Low Temperature Electrodeposition of Epitaxial Silicon Thin Films

by

Nathanael J. Downes

A dissertation submitted in partial fulfillment
of the requirements for the degree of
Doctor of Philosophy
(Chemistry)
in the University of Michigan
2022

Doctoral Committee:

Professor Stephen Maldonado, Chair
Professor Bart Bartlett
Professor Neil Dasgupta
Professor Charles McCrory

Nathanael J. Downes

downesn@umich.edu

ORCID iD: 0000-0001-6223-963X

© Nathanael J. Downes 2022

Acknowledgements

The journey to the end is not an easy one, but I've been supremely fortunate to have walked this road with a constellation of wonderful people who have helped me along the way. I'd like express my deepest gratitude to my advisor Prof. Stephen Maldonado for his patience and support over the years. His indefatigable commitment to excellence has demonstrated standards I will continue to pursue for years to come. I'd like to thank my thesis committee members Prof. Charles McCrory, Prof. Bart Bartlett, and Prof Neil Dasgupta for taking the time to evaluate my journey along the way. I'd like to thank Prof. Timothy W. Chapp and Dr. Dylan Boucher, who helped me to first start along in my scientific journey. My colleagues in the Maldonado group, both past and present, have been a tremendous source of inspiration and motivation for me and have my deepest thanks. My friends and family have been instrumental to these efforts. I thank my parents Joseph, Racheal, and Margo for their unwavering belief in me throughout my education. I'd especially like to thank my friends Stephon, Sophie, Mara, Isabella Stefan, Ella, Quintin, Omar, Josh, Justin, Brad, Emma and Adam for giving color to my life outside of science.

Table of Contents

Acknowledgements ..... **ii**

List of Figures ..... **v**

Abstract ..... **xi**

Chapter 1 Introduction **1**

1.1 Context and Importance 1

1.2 Historical Motivation for Alternative Crystallie Si Synthesis 5

1.3 Liquid Phase Epitaxy 6

1.4 Si Electrodeposition 10

1.5 Electrochemical Liquid Liquid Solid and Electrochemical Liquid Phase Epitaxy 14

1.6 Thesis Objectives and Content Description 17

1.7 References 20

Chapter 2 Electroreduction of Perchlorinated Silanes for Si Electrodeposition **26**

2.1 Introduction 26

2.2 Experimental 28

2.3 Results & Discussion 30

2.4 Discussion 42

2.5 Conclusions 45

2.6 References 46

Chapter 3 Electroreduction of $Si(NCO)_4$ for Si Electrodeposition **49**

3.1 Introduction 49

3.2 Experimental 51

3.3 Results 53

3.4 Discussion 65

3.5 Conclusions 68

3.6 References 69

Chapter 4 Electrodeposition of Epitaxial Si Thin Films at Ambient Pressure and Temperature by Electrochemical Liquid Phase Epitaxy 72

4.1 Introduction 72

4.2 Experimental 75

4.3 Results 79

4.4 Discussion 91

4.5 Conclusions 99

4.6 References 100

Chapter 5 Unfinished Works and Conclusion 104

5.1 Factors Effecting Crystalline Quality 104

5.2 Development of a Method to Produce Liquid Metal Thin Films without Compression 114

5.3 Si ec-LPE for Crystalline Si Anodes in Li-Ion Batteries 119

5.4 Conclusions 125

5.5 References 127

List of Figures

Figure 1.1 Schematic description of crystal growth in Liquid Phase Epitaxy. Adapted with permission from Ref. 76. 7

Figure 1.2 Supersaturation, misfit, and growth modes in epitaxy. Permissions from Ref. 39. 8

Figure 1.3 Schematic representation of Si electrodeposition in organic electrolyte from an oxidized molecular precursor, showing the nucleation of Si^0 after reduction at t_0, and the eventual forming an amorphous solid at t_1. 13

Figure 1.4 Schematic depiction of an electrochemical liquid phase epitaxy (ec-LPE) film growth concept with a thin liquid metal electrode with thickness h. Schematic depiction of the relevant steps in Si ec-LPE, where an oxidized species X^{4+} species dissolved in the liquid electrolyte reduces to X^0 by heterogeneous electron transfer with the liquid metal electrode, partitions into the liquid metal film across the liquid electrolyte/liquid metal interface, and then diffuses a distance h away from the liquid electrolyte/liquid metal interface before undergoing heterogeneous nucleation at the crystal seed substrate. 16

Figure 2.1 Cyclic voltammetric responses for a) the first and b) then second scans for glassy carbon electrodes immersed in propylene carbonate containing 100 mM tetrabutylammonium tetraphenylborate and either (black) no Si precursor, (red) 10 mM $SiCl_4$, (blue) 10 mM Si_2Cl_6, or (green) 10 mM $Si(SiCl_3)_4$. Scan rate = 0.1 V s^{-1} 31

Figure 2.2 Cyclic voltammograms normalized by the square root of the scan rate for glassy carbon electrodes immersed in propylene carbonate containing 100 mM tetrabutylammonium tetraphenylborate and either a) 10 mM $SiCl_4$, b) 10 mM Si_2Cl_6, or c) 10 mM $Si(SiCl_3)_4$. d) Plot showing peak current as a function of scan rate. 33

Figure 2.3 Concentration dependent voltammetric profiles for glassy carbon electrodes immersed in propylene carbonate containing 100 mM tetrabutylammonium tetraphenylborate and either 1, 2, 5, 7.5, or 10 mM solutions of either a) $SiCl_4$ or b) Si_2Cl_6. c) Plot showing the total charge passed during voltammetric cyclic in a-b) as a function of the concentration of the chlorosilane. Scan rate = 0.1 V s^{-1} 34

Figure 2.4 Time-dependent cyclic voltammetric responses for glassy carbon electrodes immersed in propylene carbonate containing either 10 mM Si_2Cl_6 and 100 mM a,d) tetrabutylammonium chloride , b,e) tetrabutylammonium tetraphenylborate, or c,f) tetrabutylammonium perchlorate at either a-c) T = 90 ºC or d-f) T = 22 °C. Scan rate = 0.1 V s^{-1} 36

Figure 2.5 Cross-sectional scanning electron micrographs of electrodeposited films prepared on n^+-Si electrodes at E = -2.5 V vs E(Ag/AgCl) as a function of the supporting electrolyte and the

formal concentration of Si_2Cl_6. Red vertical bars are a guide to the eye to indicate the average film thickness. 38

Figure 2.6 Cross-sectional film thicknesses obtained by electroreduction of Si_2Cl_6 as a function of background electrolyte, applied potential, and concentration of Si_2Cl_6. The dotted purple line indicates the expected film thickness for electroreduction of Si_2Sl_6 that results in solid Si^0 with 100% faradaic efficiency. 39

Figure 2.7 a) Schematic depiction (not drawn to scale) of an electrochemical liquid–liquid–solid (ec-LLS) process yielding crystalline Si with a liquid Ga [Ga(l)] electrode. (b) Voltammetric response obtained from 0.5 M solutions of $SiCl_4$ (red) and Si_2Cl_6 (blue) in 0.2 M tetrabutylammonium tetraphenylborate (black) at a gallium pool electrode. Scan rate = 0.1 V s^{-1}. c) and d) show macroscopic images of silicon deposits obtained by ec-LLS performed in c) 0.5 M $SiCl_4$ and d) 0.5 M Si_2Cl_6 in 0.2 M tetrabutylammonium tetraphenylborate electrolytes at E = -2.5 V vs E(Ag/AgCl) for 30 min at 120 ºC. Insets: Raman spectra of the obtained electrodeposited films measured at room temperature. 41

Figure 3.1 Temperature dependent voltammetric profiles for n^+-Si electrodes immersed in propylene carbonate containing either (dashed black line) no precursor or 0.1 M solutions of $Si(NCO)_4$ at T = (solid red line) 23 or (solid blue line) 150 ºC for baths containing a) 0.1 M tetrabutylammonium chloride and b) 100 mM tetrabutylammonium tetraphenylborate solutions. Scan rate = 100 mV s^{-1} 54

Figure 3.2 Concentration dependent voltammetric profiles for n^+-Si electrodes immersed in propylene carbonate for 0.001, 0.01, and 0.1 M solutions of $Si(NCO)_4$ at T = 23 and 150 ºC for baths containing a,c) 0.1 M tetrabutylammonium tetraphenylborate and b,d) 0.1 M tetrabutylammonium chloride solutions, respectively. The blank voltammetric responses in the absence of $Si(NCO)_4$ are denoted with dashed black lines. Scan rate = 100 mV s^{-1}. 56

Figure 3.3 Cyclic voltammograms normalized by the square root of the scan rate for n^+-Si electrodes immersed in propylene carbonate containing 0.1 M $Si(NCO)_4$ at T = 23 and 150 ºC and a,c) 0.1 M tetrabutylammonium tetraphenylborate and b,d) 0.1 M tetrabutylammonium chloride solutions, respectively. 57

Figure 3.4 a) Chronoamperometric response at E = -2.5 V vs E(Ag.AgCl) of n^+-Si electrodes immersed in propylene carbonate containing 0.1 M $Si(NCO)_4$ at T = (dashed lines) 23 and (solid lines) 150 ºC and with either (black lines) 100 mM tetrabutylammonium tetraphenylborate or (red lines) 100 mM tetrabutylammonium chloride solutions. b) Cyclic voltammetric response of n^+-Si electrodes in solutions containing 0.1 M $Si(NCO)_4$ in 0.1 M tetrabutylammonium tetraphenylborate solution (red) before and (blue) after electrolysis at E = -2.5 V vs E(Ag.AgCl) at 150 ºC. Scan rate = 10 mV s^{-1}. 59

Figure 3.5 Top-down and cross section scanning electron micrographs of deposits prepared from chronoamperometry of 0.1 M $Si(NCO)_4$ in 100 mM tetrabutylammonium tetraphenylborate at -2.5 V vs E(Ag/AgCl) for 30 min at a,c) 23 and b,d) 150 ºC, respectively. 60

Figure 3.6 a) Schematic depiction (not drawn to scale) of an electrochemical liquid–liquid–solid (ec-LLS) process yielding crystalline Si with a liquid e-GaIn electrode. b) Cyclic voltammetry

obtained from 0.1 M solutions of $Si(NCO)_4$ (solid red line) in 0.1 M tetrabutylammonium chloride (solid black line) at a eutectic gallium indium pool electrode. Scan rate = 100 mV s^{-1}. c) Photograph of an *e*-GaIn pool electrode after biasing at E = -2.5 V in propylene carbonate containing 0.1M $Si(NCO)_4$ in 0.1 M tetrabutylammonium chloride at E = -2.5 V vs E(Ag/AgCl) for 30 min at T = 23 ºC. d) Raman spectra of the collected deposit in c). 64

Figure 4.1 Overview of the electrochemical liquid phase epitaxy (ec-LPE) film growth concept with a thin liquid metal electrode with thickness h. Schematic depiction of the relevant steps in Si ec-LPE, where an oxidized species Si^{4+} species dissolved in the liquid electrolyte reduces to Si^0 by heterogeneous electron transfer, partitions into the liquid metal film, and then diffuses some distance away from the liquid electrolyte/liquid metal interface before undergoing heterogeneous nucleation at the crystal seed substrate. 74

Figure 4.2 (a) Exploded view of the ec-LPE cell used in this work. Using photoresist patterned seed substrates and porous SiC membranes, large two-dimensional liquid metal thin films are formed in this cell using a compression stack. Following assembly, liquid metal is flowed in to a final thickness defined by the photoresist and liquid electrolyte is exposed to the liquid metal surface by a porous membrane that is permeable to electrolyte but resists intrusion by the liquid metal. (b) Representative view of an assembled ec-LPE cell. 77

Figure 4.3 Voltammetric response of a *e*GaIn liquid metal thin film with the ec-LPE cell shown in Figure 4.2, with an electrolyte containing 0.1 M $(C_4H_9)_4NCl$ in propylene carbonate without (black) and with (red) 0.5 M $SiCl_4$ at T = 125 °C and scan rate = 0.1 V s^{-1}. b-d) Representative chronoamperometric traces of an ec-LPE deposition of a Si film using the follow conditions: T = 125 °C, and an electrolyte containing 0.5 M $SiCl_4$ and 0.1 M $(C_4H_9)_4NCl$ in propylene carbonate on an n^+-Si(100) seed substrate via b) direct electrodeposition at E = −1.6 V vs E(Ag/AgCl), c) direct electrodeposition at E = −1.6 V vs E(Ag/AgCl) refreshing the electrolyte bath every 300 s. d) Macroscopic image of deposit obtained on the n^+-Si(100) electrode after electrolysis and subsequent liquid metal removal..... 80

Figure 4.4 a,b) Top-down scanning electron micrographs of initial Si deposits in ec-LPE depositions performed with the same conditions as in Figure 4.1) with n^+-Si(100) and n^+-Si(111) seed substrates, respectively. c) Top-down view scanning electron micrograph of the deposit shown in Figure 4.3d). d) Diamond cubic indexed Kikuchi bands collected from the red cross-hair shown in c). e) Color-coded electron back scatter diffraction (EBSD) map of Si ec-LPE sample grown at T = 125 °C. (f) Contour pole figures from the EBSD mapping shown along the 110 and 111 poles. g) Atomic-force micrograph of Si thin film on Si substrate. (h) Line profile of the height of the Si thin film shown in (g). 82

Figure 4.5 a) Bright field transmission electron micrograph of a cross section of an epitaxial Si film prepared by ec-LPE on a n^+-Si(100) at 125ºC. The red, green, and blue dashed circles correspond to the position of the selected area aperture in **1-3.** Shown in **1-3** are partially indexed selected area electron diffraction (SAED) patterns from the epifilm, the epifilm-substrate interface, and the substrate respectively. b) High magnification scanning transmission electron micrograph of a cross section of the Si epifilm shown in a). c) Representative high-resolution transmission electron micrograph of the interface between the Si film and Si substrate shown in a). (d) STEM-EDS mapping of the Si epifilm shown in a) with elemental maps of Si, Ga shown

in in e) and f), respectively. Pixel intensities were normalized by the full-area integrated EDS spectra. Scale bar represents 50 nm. 84

Figure 4.6 a) Representative coupled 2Θ-ω X-ray rocking curves of a Si film prepared by ec-LPE on n^+-Si(100). Inset: X-ray diffractogram of Si films prepared by ec-LPE with n^+-Si(100). b) Normalized Raman spectra of n^+-Si(100) seed substrate (black) and an epitaxial Si thin film (red) prepared by ec-LPE using the conditions shown. 86

Figure 4.7 a) Schematic depictions of the electrodeposition condition employed in b) Representative chronoamperometric trace of a Si ec-LPE pulsed electrodeposition experiment (E_1 = -1.6 V for 0.2 ms, E_2 = -0.77 V for 10 ms) from electrolyte containing 0.5 M $SiCl_4$ and 0.1 M $(C_4H_9)_4NCl$ in propylene carbonate at T = 125 °C, with the electrolyte refreshed after every hour. c,g) Macroscopic image of deposit obtained on the n^+-Si(100) electrode after electrolysis and subsequent liquid metal removal. d,g) Cross-section scanning electron micrograph of Si ec-LPE sample grown at T = 125 and 23 °C, respectively e,h) Color-coded electron back scatter diffraction (EBSD) map of Si ec-LPE sample grown at T = 125 and 23 °C, respectively. f,i) Contour pole figures from the EBSD mapping shown along the 110 and 111 poles of Si ec-LPE sample grown at T = 125 and 23 °C, respectively. 88

Figure 4.8 a,b) High magnification scanning transmission electron micrograph of a cross section of the Si epifilm grown by pulsed electrodeposition at T = 23 and 125 ºC, respectively. b) Bright field transmission electron micrograph of a cross section of an epitaxial Si film prepared by ec-LPE on a n^+-Si(100) at 125ºC. The red and blue dashed circles correspond to the position of the selected area aperture in 1-2. Shown in 1-2 are partially indexed selected area electron diffraction (SAED) patterns from the epifilm and the substrate respectively. h) STEM-EDS mapping of Si epifilm with elemental maps of Si, Ga shown in i) and j), respectively. Pixel intensities were normalized by the full-area integrated EDS spectra..... 90

Figure 4.9 Schematic description of the operative pathways in Si ec-LPE during a) direct electrodeposition and e) pulsed electrodeposition, composed of the operative steps shown in b-d) and f-h), respectively..... 92

Figure 4.10 Schematic description of the dominant modes of epifilms growth under conditions of low supersaturation (bottom row), where large epitaxial grains predominantly grow, and under conditions of high supersaturation (top row) where the driving force is sufficient for nucleation to predominate over continued nuclei growth. In both cases, following coalescence of neighboring nuclei, a film is formed which continues to grow in a step flow growth-mode..... 98

Figure 5.1 Binary phase diagrams of Si in a) Ag, b) Ga, c) In. Reproduced with permissions from Ref. 2, 3, 5. Shown in figure d) ternary equilibrium diagram for the Ga-In-Ag system at room temperature. Reproduced with permission from Ref. 4. 105

Figure 5.2 Top-down scanning electron micrographs of initial Si deposits in Si ec-LPE pulsed electrodeposition experiment (E_1 = -1.6 V for 0.2 ms, E_2 = -0.77 V for 10 ms) from electrolyte containing 0.5 M $SiCl_4$ and 0.1 M $(C_4H_9)_4NCl$ in propylene carbonate at T = 23 °C with n^+-Si(100) seed substrates using a) *e*-GaIn and b) *e*-GaInAg electrodes.....107

Figure 5.3 a) Cross section scanning electron micrograph of a deposits obtained by Si ec-LPE pulsed electrodeposition experiment (E_1 = -1.6 V for 0.2 ms, E_2 = -0.77 V for 10 ms) performed for 24 hr from electrolyte containing 0.5 M $SiCl_4$ and 0.1 M $(C_4H_9)_4NCl$ in propylene carbonate at T = 23 °C with n^+-Si(100) seed substrates using *e*-GaInAg electrode. b) Top down scanning electron micrograph of the liquid metal surface with corresponding energy dispersive spectroscopy elemental maps of c) O and d) Si. 108

Figure 5.4 Scanning electron micrograph cross section of a Si films prepared from a 4 hour Si ec-LPE pulsed electrodeposition experiment (E_1 = -1.6 V for 0.2 ms, E_2 = -0.77 V for 10 ms) from an electrolyte containing 0.5 M $SiCl_4$ and 0.1 M $(C_4H_9)_4NCl$ in propylene carbonate at T = 65 °C on a n^+-Si(100) seed substrates using *e*-GaInAg electrode. b) EDS mapping of the red box in the Si epifilm shown in a). 110

Figure 5.5 Representative coupled 2Θ-ω X-ray rocking curves of the Si ec-LPE film shown in Figure 5.3a). 111

Figure 5.6 Shown is a compilation of top-down scanning electron micrographs organized as a function of the rest potential pulse duration, the liquid metal additive provided by dissolution of the wetting layer, and the concentration. All Si thin films were prepared from a 1 hour Si ec-LPE pulsed electrodeposition experiment (E_1 = -1.6 V for 0.2 ms, E_2 = -0.77 V for 0.1, 1, or 10 ms) from an electrolyte containing 0.05 or 0.5 M $SiCl_4$ and 0.1 M $(C_4H_9)_4NCl$ in propylene carbonate at T = 65 °C on a n^+-Si(100) seed substrates using *e*-GaIn electrodes with 20 nm Cu, Sn, or Ag wetting layers. 113

Figure 5.7 Schematic depiction of the geometric requirements to promote imbibition of a liquid metal into a microstructured film. 115

Figure 5.8 a) Cross-section micrograph of a Si substrate patterned with 13 μm an array of pillars. b) High magnification scanning electron micrograph of a pillar after coating with Au by thermal evaporation. Inset: elemental dispersive spectroscopy map of Au in the same region. c) Low magnification scanning electron micrograph of the micropillar array. 117

Figure 5.9 a) Cross-section scanning electron micrograph of Au coated pillar array following thermal evaporation of Ga and complete imbibition. b) Top down scanning electron micrograph of the film shown in a). c) Cross section elemental dispersive spectroscopy of the film shown in a) demonstrating the Ga (blue) film and the Si (red) substrate. d) Shown is a cyclic voltammogram of the film in a) immersed in 10 mM NaB_4O_7 in deionized water. Scan rate = 100 mv s^{-1}. e) Top-down low magnification scanning electron micrograph of the microstructured electrode after voltammetric cycling. 118

Figure 5.10 a) Macroscopic image of a compressionless Si ec-LPE pulsed electrodeposition experiment (E_1 = -1.6 V for 0.2 ms, E_2 = -0.77 V for 10 ms) from electrolyte containing 0.5 M $SiCl_4$ and 0.1 M $(C_4H_9)_4NCl$ in propylene carbonate at T = 23 °C using a *e*-GaIn thin film on Cu foil support. b) Scanning electron micrograph of the active electrode area after removal of *e*-GaIn, corresponding to the red region highlighted in a). Scanning electron micrograph of the green region in b) with corresponding energy dispersive spectroscopy elemental map scans of d) Si and e) Ga. 121

Figure 5.11 Macroscopic photographs showing the wetting behavior of *e*-GaIn on Cr coated (20 nm) Cu foil substrates a) without and b) with surface bound N-(trimethoxysilylpropyl)ethylenediamine, triacetic acid. 122

Figure 5.12 a) Low magnification scanning electron micrograph of a Si ec-LPE pulsed electrodeposition experiment (E_1 = -1.6 V for 0.2 ms, E_2 = -0.77 V for 10 ms) from electrolyte containing 0.5 M $SiCl_4$ and 0.1 M $(C_4H_9)_4NCl$ in propylene carbonate at T = 23 °C using a *e*-GaIn thin film on Cr (20 nm) coated Cu foil support showing high degree of deposit coverage. Inset: Macroscopic image of the Cr/Cu electrode surface. b) High magnification scanning electron micrograph of the active electrode area of the film shown in a). Inset: Raman spectra corresponding to the film. c) Scanning electron micrograph of the deposit film with corresponding energy dispersive spectroscopy elemental map scans of d) Cr, e) O, f) Ga, and e) Si. 124

Abstract

This thesis explores the applicability of Si electrodeposition to the synthesis of crystalline Si at low temperatures. Electrodeposition has been long perceived as an ideal route for the synthesis of semiconductor materials owing to the technical simplicity, scalability and intrinsically low cost of the method. However, to date, Si electrodeposition has found limited success for crystalline Si synthesis. Recently, a new method, called the electrochemical liquid liquid solid (ec-LLS) strategy, has been shown to synthesize crystalline Si at low temperatures by electrodeposition with $SiCl_4$ at liquid metal electrodes. While crystalline Si growth by ec-LLS was demonstrated, there was deemed an immutable temporal limitation to the electrolyte bath lifetime. Accordingly, the expansion of the ec-LLS method for crystalline Si film synthesis was hypothesized to require a better optimized Si electrodeposition electrolyte bath. On this front, this thesis has two major advances.

First, two previously unexplored molecular classes of silanes are explored as precursors for Si electrodeposition. Here, the electrochemical activity of the perchlorinated oligochlorosilanes hexachlorodisilane and tetrakis(trichlorosilyl)silane, which contain the Si-Si bonding moiety, and tetraisocyanatosilane, which contains the pseduohalide NCO^- ligand, were investigated in comparison to tetrachlorosilane as a function of electrolyte composition and bath temperature. For both the oligochlorosilanes and tetraisocyanatosilane the voltammetric responses were similar to tetrachlorosilane, suggesting that at ambient temperatures the electroreductive mechanism proceeds through a similar route. Following amperometric deposition of all of these precursors at

ambient temperature, amorphous Si was obtained. Despite their utility under ambient conditions, the chemical stability and electrochemical activity of both precursor classes were significantly attenuated at elevated temperatures, demonstrating the limited thermal range of their use therein. Further, when electrodeposition of these precursors at Ga-based electrodes was performed, under no conditions explored was the synthesis of crystalline Si observed. Cumulatively, while both precursor classes may be useful for Si electrodeposition at ambient conditions, further work is required to apply them for the low temperature synthesis of crystalline Si by ec-LLS.

Second, the application of Si electrodeposition to the electrochemical Liquid Phase Epitaxy (ec-LPE) method, a macroscopic thin film variant of ec-LLS, was demonstrated for the synthesis of thick epitaxial Si films at ambient temperature. Previously, using electrolyte baths containing $SiCl_4$ ec-LPE could be used to grow epitaxial Si thin films limited to a few hundred nanometers in thickness before the inevitable cessation of further growth. Here, the electrodeposition waveform was demonstrated to be critical to both the electrolyte bath lifetime and also for the general synthesis of thick films. Specifically, using a pulsed electrodeposition waveform in which a brief pulse generating Si^0 was followed by a longer pulse at a potential absenting any redox process, the electrodeposition of Si was shown to be sustained for hours rather than minutes. The presented electron microscopy, electron diffraction, and x-ray diffraction data demonstrate that even down to T = 23 ºC, the synthesis of thick epitaxial Si films by ec-LPE is possible. Further efforts discussing methods for optimizing materials quality in Si ec-LPE and the application of as-grown thin films are discussed, with final conclusions on the cumulative work shown here.

Chapter 1

Introduction

1.1 Context and Importance

Over the last decade, solar energy production has seen an exponential growth. Annual global installations of photovoltaics (PV) has gone from 20 GW in 2010 to 140 GW by the end of 2020, resulting in a cumulative peak energy production of 0.65 TW.[1] At the same time, with each passing year ushering in technological development in nations across the globe, human kind consumed a record 18.5 TW of energy by the end of 2020, the largest to date.[2] Among candidate renewables sources, solar unambiguously holds the greatest potential for not only compensating the continuous year-over-year global energy demand increase, but for doing so in the near term. In evaluating which candidate material to use in PV expansion, there are four essential criteria to consider. First, in order to streamline device construction, the metallurgy/physics/chemistry of the PV material is holistically understood. Second, following the installation and regular operation of the PV device, the cell has an indefinite period of operability. Third, in the event of catastrophic device failure, the constituent elements in the PV device should pose no threat to the environment. Fourth, manufacture of the PV material should be widely available, require minimal infrastructure, and have little effect on the environment.

Among all candidate semiconductors for PV integration, monocrystalline Si (c-Si) is the obvious choice for three primary reasons. First, the device engineering of Si manufacture and device integration is firmly established. For instance, problems concerning doping, hetero/homojunction formation, and surface passivation have been studied for *decades* and are considerably more advanced for Si than almost any other material.[3-4] In fact, the photoconversion efficiency loss mechanisms in Si have been well studied that PV devices are now approaching the Shockley-Quiessier limit.[5] Regarding PV based operation lifetime, Si based PVs were the first on the market and have consequently been available for nearly four decades. Although manufacturers generally grant a 20-year lifetime, Si based PV modules have a practically indefinite period of operability, with some Si PV devices still operating 40 years after the initial installation with no little added maintenance.[5] In the event of disastrous device failure, the release of crystalline Si poses no significant environmental or public health concern. Interestingly, zero valent Si is so biocompatible that it is even being considered for *in vivo* drug delivery methods.[6] While the list of possible semiconducting materials for mass scale PV devices is long, only c-Si unambiguously satisfies three of these four criteria.

Despite these ideal characteristics, the near-term rapid proliferation of Si PVs needed to meet the 18.5 TW energy demand is not possible with the current manufacturing framework for producing high purity (>99.9999%, or 6*N* purity) solar grade crystalline silicon (SoG-Si). Because raw silicon exists in nature only as either impure silica (SiO_2) or silicates ($Si_{4-x}O_x^{(4-2x)-}$), obtaining SoG-Si necessitates several extremely energy intensive and environmentally taxing reduction, purification, and crystallization steps.[7] The initial conversion of raw silica/silicates to zero valent silicon is accomplished presently by carbothermic reduction, a method established nearly 200 years ago.[8] Here, lumpy quartz is combined with graphite in an electric arc furnace and heated to

temperatures exceeding 1800 ºC in order to produce low purity (<99.9%) metallurgical grade Si (mg-Si), according to reaction 1.[7, 9-10]

$$SiO_2\ (s) + 2\ C\ (s) \longrightarrow Si\ (l) + 2\ CO\ (g) \qquad (1)$$

Despite the apparent simplicity of the reaction, there are two significant complications involved with this process that preclude near-term Si PV expansion.

First, the environmental toll of producing c-Si by carbothermic reduction is tremendous. The Si-O bond is remarkably stable, having a bond dissociation energy of 452 kJ/mol.[11] In effect, the scission of Si-O bonds in a silica matrix requires an intensive thermal input. Thus, while the stoichiometry of reaction 1 suggests that for each mole of Si 2 equivalents of CO_x should be produced, as a consequence of low reduction efficiencies (~85%)—which become further exacerbated with decreasing operation scale—and the electricity needed to supply the arc furnace, the reality is considerably more.[10] For instance, operation of the arc furnaces to create metallurgical grade Si (mg-Si) (<99.5%) requires 12 kWh kg^{-1} of electricity, translating into 1.2 MJ mol^{-1} Si.[12-13] However, the overwhelming majority of energy expended in the production of SoG-Si occurs in the purification of this mg-Si. After mg-Si synthesis, several extensive chemical or physical processes are applied, followed by some manner of controlled precipitation (e.g. directional solidification, crystal nucleation/growth) to yield SoG-Si.[14-16] Thus, some combination of high temperatures, strongly oxidizing environments, or intolerably extreme pH (whether acidic or basic leaching), and alloying are required for upgrading.[12] The approximate energy required to make SoG-Si from metallurgical refining of mg-Si is approximately 20 kWh kg^{-1} (2 MJ mol^{-1} Si).[17] This inordinately large energy input required to purify mg-Si represents an entropic cost for taking raw sources of Si to PV grade Si. In addition to the economic cost is the environmental toll incurred by the purification process. For making SoG-Si a closed loop Siemens method is predominately

employed, whereby mg-Si is converted to trichlorosilane by reaction with toxic gaseous HCl, then distilled, and deposited as purified SoG-Si, ultimately resulting in a large amount of extremely toxic and corrosive waste byproducts.[18] For reference, every 1 kg of SoG-Si *upgraded* from impure mg-Si consumes 26.6 kg of carbon and results in the emission of 84 kg of CO_2 and produces 14 kg of waste.[17] Cumulatively, these processing steps at mass scale pose significant environmental risks and render the energy buyback time of each Si PV module produced to be on the scale of years.[19]

Second, and arguably more limiting than the environmental concerns imposed by modern Si manufacturing, is the long-term fiscal volatility in the Si PV market. Over the past several decades, the cost of Si PV modules has dropped considerably, and can be partially ascribed to advances in production processes, lessened Si kerf waste during processing, and improvement in device performance thereby minimizing the amount of Si required.[5, 20-22] However, the most dramatic reductions in price can be directly attributed to subsidies from foreign governments.[1, 23-25] In specific, since the enactment of China's New Renewable Energy law in 2006, and in conjunction with various feed-in tariff policies, government led special programs for PV development, and supporting policies from local governments, the per module cost of Si PVs has dropped by 90%.[25-28] At present, this is best contextualized with the value of SoG-Si, which is ~$10/kg.[6] However, the true market value of SoG-Si is inherently tethered to these subsiding policies. Should geopolitical problems emerge or foreign governments lessen their commitment to solar energy production, the value of SoG-Si skyrockets back to ~$70/kg.[12, 29] Furthermore, with fossil fuel sources still providing the largest energy output for cost input, the profit margins achievable in SoG-Si manufacturing are too slim to justify the financial risk of potential new manufacturers.[2]

1.2 Historical Motivation for Alternative Crystalline Si Synthesis

In addition to the previously described ideal characteristics of a semiconductor candidate for mass application in photovoltaic technologies, one critical factor in the market dominance of Si today is simply that bulk high purity Si materials were already available by the time solid state Si devices were being studied. The foundation of modern electronics can be related back to the first demonstration of the semiconductor transistor effect in 1947 by Brattain, and Bardeen.[30] At the time, Shockley was aware that in order to devise reliable high performance commercial devices, the impurity concentration needed to be reduced to the part per billion scale (99.9999999% purity, or 9*N*), far below what was available at the time.[31] The breakthrough came from William Pfann who invented the zone-refining technique that afforded sufficiently pure Si and Ge for application in commercial transistors.[32] Such advancements were being made in the synthesis of high quality Si that by the start of 1960's dislocation-free, "dinner plate" (300 mm diameter) single crystal wafers were readily commercially available.[33-39] At the same time, the landmark work of Chapin et al. at Bell Lab's in 1954 demonstrated the first *p-n* junction photocell with a conversion efficiency 6%.[40] As a result of the widespread availability of 9*N* pure electronic grade Si, Si PV devices, requiring only 6*N* purity, were simply constructed. Progress was so rapid that by the late 1970's conversion efficiencies of over 19% were being reported.[41] Today, Si PV devices now approach the Shockley-Quiessier limit.[5]

Ironically, the manufacture standard and commercial availability of 9*N* Si ultimately became a limiting factor in the viability of making mass scale Si PVs both economically and environmentally. While many advances in thin film PVs have been made that mitigate the issue now, due to the poor absorption coefficient of Si, in order to make high efficiency devices thick

(>200 μm) slabs are required.[42] That is, owing to the premium to be paid for 9*N* pure Si, Si PVs were prohibitively expensive. Thus burgeoned an interest in developing cost-effective routes to make SoG-Si.

1.3 Liquid Phase Epitaxy

The pursuit of alternative synthetic routes to SoG-Si bypassing the current manufacturing dogma is not new. One such method for that was explored for the growth of SoG-Si is Liquid Phase Epitaxy (LPE). Shown schematically in Figure 1.1, LPE is crystal growth method that uses a fluid medium to solvate component atoms of solid phase to develop a reversible pathway between the solid and liquid phases.[43] This reversibility allows atoms to continually deposit (or adsorb) and dissolve until an atom reaches its thermodynamically stable point in the growing solid. This reversibility is driven by a thermal gradient that creates local differences in the supersaturation to induce heterogeneous nucleation on the underlying substrate. In LPE the supersaturation defines the growth rate, v, of a crystal by:

$$v = (n - n_e)D/\rho\delta \tag{1.1}$$

where n is the effective concentration, n_e is the equilibrium concentration at given temperature, D is the diffusion coefficient of the solute in the melt, and δ is the diffusion boundary layer thickness. Thus, when the melt is slowly cooled such that the deviation of the effective concentration is slightly smaller than the equilibrium concentration at a given temperature, the growth rate is very slow. Conversely, when large thermal gradients are imposed, the supersaturation is large and the growth rate is fast. A key advantage of LPE, relative to other crystal growth methods, is the ability to drive crystal growth at small supersaturation. As shown

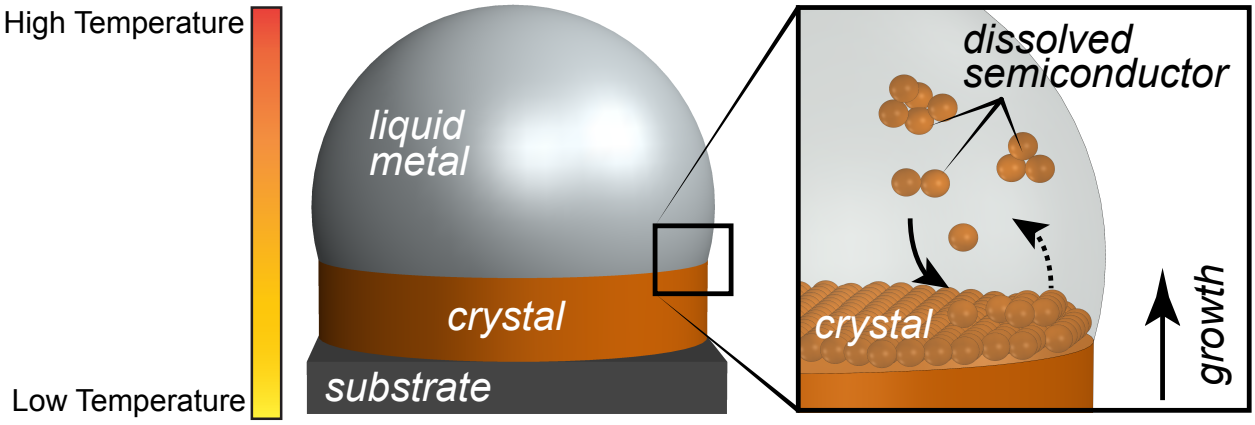


Figure 1.1 Schematic description of crystal growth in Liquid Phase Epitaxy. Adapted with permission from Ref. 76.

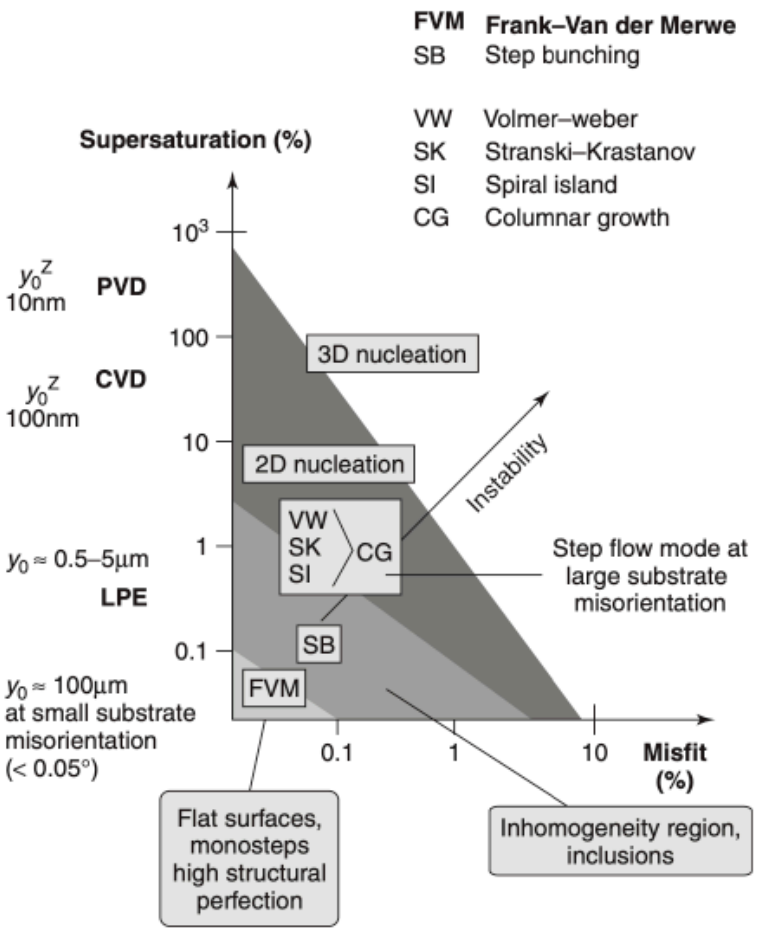


Figure 1.2 Supersaturation, misfit, and growth modes in epitaxy. Permissions from Ref. 39.

in Figure 1.2, as the supersaturation is increased the growth mode becomes increasingly unstable, resulting in greater surface coarsening due to the emergence of 3D structures rather than 2D monoatomic steps. LPE is defined as a near-equilibrium growth method in which the supersaturation of the dissolved atoms of the growing solid is near zero and is a route for making structurally perfect solids with orders of magnitude fewer defects than the substrate upon which it is grown.[44-45]

There are several advantages to the application of LPE in the growth of SoG-Si. First, as mentioned, the defects (e.g. large quantity of dislocations, twins, and stacking faults) of a low quality substrate upon which an epitaxial layer is grown become essentially 'annealed' out.[44] That is, low quality mg-Si carrier substrates can be used in the growth of high quality thick epitaxial Si layers. Second, owing to the nature of dissolved components in the melt, LPE is an effective strategy for purifying impure source materials. Specifically, the segregation coefficient k_i for a species i follows a temperature dependence according to:

$$k_i \equiv \frac{C_i^S}{C_i^L} \tag{1.2}$$

$$= k_{i,0} \cdot \exp\left[-\frac{b_i}{T}\right] \tag{1.3}$$

where $C_i^S$is the impurity concentration of species I in the solid phase, C_i^L is the impurity concentration in the liquid phase, T is the absolute temperature, and $k_{i,0}$ and b_i are positive constants which correspond to a specific metal.[45] For most metals, the segregation coefficient is relatively low, and tends to decrease with temperature.[46] Thus, when low purity mg-Si is used the source material from which a molten metal solution becomes saturated with dissolved Si^0, the purity of the resultant epitaxial layer can be considerably upgraded. Lastly, LPE is advantageous especially for its ability to form epitaxial layers at low temperatures (280-1200 ºC). Simply, the only limitation in LPE is the ability to saturate a molten metal solution with Si^0 and for the melt to

remain molten during the crystallization of the Si epitaxial layer. Given the wide range of known low-temperatures solders and the existence of metals like Hg and Ga, which are liquid at or near room temperature, LPE is a unique strategy by which Si epitaxial layers can be grown at low temperature in a wide range of metal solvents.[45, 47-60]

While LPE has many attractive qualities for application in SoG-Si manufacture, it does suffer several fundamental drawbacks. A persistent and difficult problem in LPE is the existence of substrate defects, specifically oxides that inhibit the nucleation and growth of layers. While the use of reducing gases (e.g. forming gas, H_2) and oxide scrubbing elements (Al, Mg, etc.) added to the melt can ameliorate the problem it serves as a significant barrier in reproducibility.[61-64] A separate, and critical problem in LPE is the inability to stop and start the growth at need. Ultimately, since LPE is a thermodynamic process that hinges on the saturation of a component in the liquid phase, no kinetic control existed to grow films of set dimensions or thickness despite rigorous efforts to the contrary. Consequently, Si LPE has faded into obscurity.

1.4 Si Electrodeposition

Beyond LPE, a second significant alternative for SoG-Si synthesis that has been explored is electrodeposition. Historically, electrodeposition has long been viewed as an ideal method for materials synthesis. Uniquely, electrodeposition uses the cleanest imaginable source to reduce oxidized species to their zero valent form—electrons. By virtue of the ability to inject electrons into a species by the application of a controlled applied bias, electrodeposition is a kinetically precise method that requires no thermal input and can be done under ambient conditions. Furthermore, the equipment needed to perform an electrodeposition experiment are cheap, easily

used, and scalable. [65-66] Consequently, electrodeposition has attracted a considerable range of interest as a method for producing SoG-Si.

Over the past five decades several strategies have been employed for the electrodeposition of Si. In the ideal case, electrodeposition should be performed under standard conditions with common solvents in order that minimal technical input is required to obtain zero valent Si. In the simplest case, silica should be directly reduced to zero valent Si. However, Si-O bonds, as previously mentioned, are very strong and have a reduction potential that lies outside the solvent window of all molecular solvents. Thus, two separate routes of Si electrodeposition have been pursued in the last half century. The first route aims to electrodeposit Si under ambient conditions using molecular silanes that are easily reduced in common organic solvents. The second route seeks to reduce oxidized silica (e.g. sand) to zero valent Si directly, using high temperature molten salt eutectic mixtures.

Low-temperature Si electrodeposition has largely been explored in common organic solvents such as tetrahydrofuran, dichloromethane, acetonitrile, sulfolane, propylene carbonate.[67-74] The range of available molecular silanes to be used as Si precursors is vast, but the list of viable precursors is brief. The alkoxysilanes, $Si(OR)_4$ where R represents an alkyl group, would be ideal precursors given the known chemical routes to form them from silica directly.[9] While there have been reports claiming to form amorphous Si by chronoamperometric deposition, these claims are dubious in their contradiction of available literature and were also unrepeatable in our hands.[75-76] Aminosilanes, $Si(NR)_4$, and organosilanes, SiR_4, have also been explored but were similarly shown to be irreducible in organic solvents.[76] Only the halogenated silanes (SiX_4, where $X = Cl^-$, I^-, Br^-) and hydrohalosilanes ($SiHX_3$) were found to be reducible within the solvent window of the aforementioned organic media, and of these $SiCl_4$ was the most ideal precursor.[70, 72-73]

Nevertheless, electrodeposition at low temperatures is plagued by the formation of impure amorphous Si, which immediately oxidizes when exposed to lab air due to the reticulated structure of the film.[70] Consequently, the as-obtained Si electrodeposition is of limited utility. This observation in organic solvents has been deemed virtually immutable, due to (1) the insolubility of Si^0 in molecular solvents such that no reversible pathway exists and (2) the low adatom mobility due to the Si-Si bond energy being much greater than the available thermal energy, precluding the reorganization of the deposited solid.[45, 77] This is show schematically in Figure 1.3. Ultimately, while the resultant deposit can be annealed and subsequently crystallized, the indirect nature of forming crystalline Si with organic electrolyte based Si electrodeposition serves as a significant impediment to the methods utility.[70]

Interest in Si electrodeposition at low temperatures has been revitalized in the past decade with the emergence of room temperature ionic liquids (RTIL). These solvents have a melting point below 100 ºC, have large electrochemical windows, and are water/air stable.[78] While the RTILS and organic solvents have similarly shown a large drawback for Si electrodeposition due to contamination in the deposited amorphous layers, RTILs have become in vogue given their favorable physical properties over organic electrolytes, which make the possibility of their scaling more attractive. To this end, much work in the literature has abounded to develop RTIL-based Si electrodeposition. Several RTILs have been explored including 1-butyl-3-methylimidazolium-bis(trifluoromethylsulfonyl) imide ($BMImTf_2N$), 1-butyl-3-methylimidazolium-hexafluorophosphate ($BMImPF_6$), and 1-butyl-1-methylpyrrolidinium bis(trifluoromethylsulfonyl)imide ($[BMP]Tf_2N$).[78-79] These RTILs are of particular note owing to the demonstration that they can tolerate large quantities of water in comparison to organic electrolytes, with no consequence to the obtained deposit.[79] More recently, special attention has

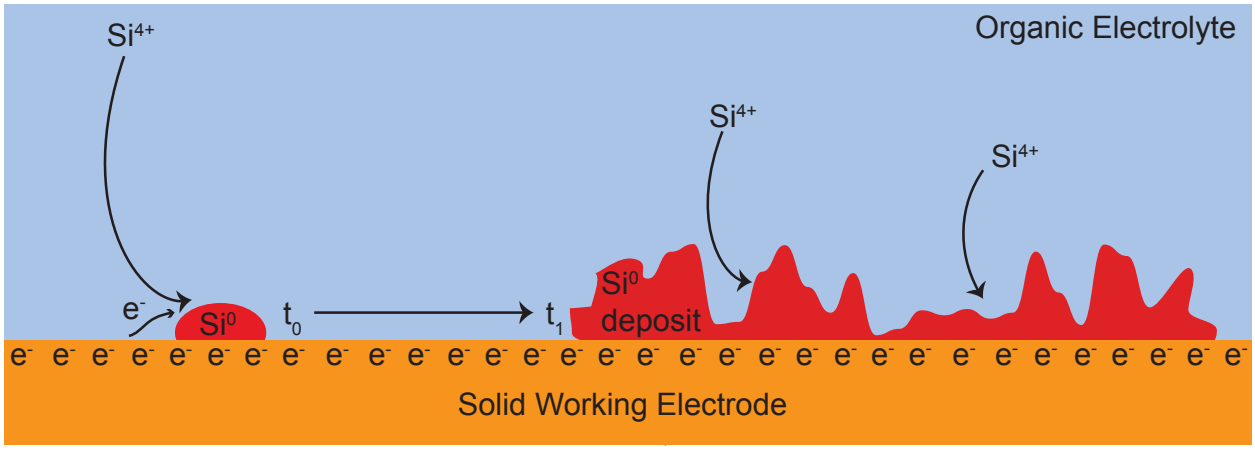


Figure 1.3 Schematic representation of Si electrodeposition in organic electrolyte from an oxidized molecular precursor, showing the nucleation of Si^0 after reduction at t_0, and the eventual forming an amorphous solid at t_1.

been paid to understanding the elementary processes of Si electrodeposition from RTILs including the formation of homogenous side-products during dissolution, the sum reductive pathway of $SiCl_4$ to Si^0, and the establishment of numerical models describing the nucleation pathway during deposition.[80-86] While considerable progress has been made in defining the operative processes in Si electrodeposition from RTILs, these solvents still suffer the same long-term problem of producing low-quality Si deposits.

In the second route, separate efforts have been devoted to the exploration of Si electrodeposition in molten salts. Here, owing to the reduction potential of Si-O and Si-F bonds being more positive than that of the molten alkali metal earth salts being used as the solvent, Si can be electrodeposited using silicate and fluorosilicates as the oxidized precursors.[65-66, 87-88] The electrodeposition of SiO_2 has had great breakthroughs in the last twenty years, following the discovery that complexing agents such as $CaCl_2$ and CaO can help to electrochemically activate the dissolved SiO_2.[89] Significantly, the electrodeposition of Si in molten salts by these methods results in polycrystalline Si, which has recently been shown to be of high enough purity to be used in functional PV devices.[89-90] However, the operating temperatures of molten salt electrolyses is in excess of T = 600 ºC and requires specialty equipment that is both difficult to operate and to bring to scale.

1.5 Electrochemical Liquid Liquid Solid and Electrochemical Liquid Phase Epitaxy

In the last decade, a method for the growth of covalent and inorganic has emerged denoted the electrochemical liquid-liquid-solid (ec-LLS) strategy.[6, 91-94] In ec-LLS, liquid metal electrodes are used (1) as a source of electrons to drive the reduction of oxidized precursors (M^+) in solution

to their zero valent form (M^0) and (2) as a medium for recrystallization in which deposited M^0 can partition into the liquid metal until the equilibrium concentration is sufficiently exceeded to nucleate a crystalline solid (Figure 3).[95] In ec-LLS, the dominant nucleation pathway is dictated by the size of the liquid metal electrode. That is, when the liquid metal volume is in on the scale of 1 cm^3 the concentration gradient in the liquid metal exceeds supersaturation locally and a crystal homogenously nucleates. When the liquid metal volume is scaled at or beneath 10^{-10} cm^3 then the concentration gradient of M^0 in the liquid metal does not exceed supersaturation locally and M^0 can diffuse to the underlying substrate and nucleate heterogeneously.[95] Consequently, when the liquid metal height is on the scale of microns and the underlying substrate is crystalline, the resultant crystal that nucleates grows in crystallographic registry with the underlying substrate (e.g. epitaxial). In the latter case, a modified version of ec-LLS, denoted electrochemical Liquid Phase Epitaxy (ec-LPE) and shown schematically in Figure 1.4, using macroscopically large (cm^2) yet microscopically thin (> 20 μm) liquid metals has been demonstrated for the growth of macroscopic epitaxial Ge films.[93] Cumulatively, ec-LPE marries the kinetic control that is afforded by electrodeposition with the thermodynamic aspects of LPE that afford the growth of crystalline solids.

Previous work has applied the ec-LLS and ec-LPE strategies for the growth of crystalline Si, though in the case of the latter, to limited success. The growth of crystalline Si by electroreduction of dissolved Si precursors with liquid metal electrodes has been demonstrated in propylene carbonate, ionic liquids, and KCl-KF molten salt electrolytes.[96-97] Using $SiCl_4$ electrolyte solutions in propylene carbonate, the growth of Si nano- and microwires has also been shown at temperatures as low as 60 ºC.[91-92] However, the application of this same electrolyte solution to ec-LPE resulted in crystalline epitaxial films limited in thickness on the

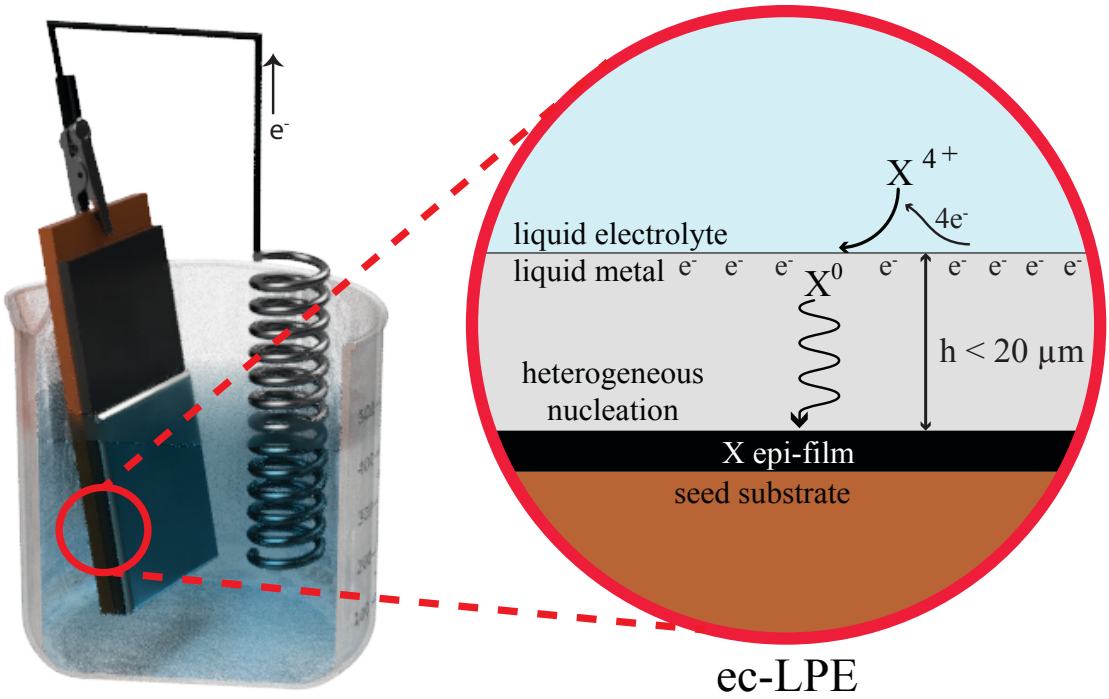


Figure 1.4. Schematic depictions of an electrochemical liquid phase epitaxy (ec-LPE) film growth concept with a thin liquid metal electrode with thickness h. Schematic depiction of the relevant steps in Si ec-LPE, where an oxidized species X^{4+} species dissolved in the liquid electrolyte reduces to X^0 by heterogeneous electron transfer with the liquid metal electrode, partitions into the liquid metal film across the liquid electrolyte/liquid metal interface, and then diffuses a distance h away from the liquid electrolyte/liquid metal interface before undergoing heterogeneous nucleation at the crystal seed substrate.

scale of a few hundred nanometers.[98] Cumulatively, during electrolysis of $SiCl_4$, at any dimension, the experiments resulted in the inevitable cessation of deposition and the observation that an oxidized amorphous Si material coated the liquid metal electrode.[99] These observations, in totality, bore forth the hypothesis that the fundamental limitations observed in ec-LPE was a direct consequence of deleterious, unavoidable side processes of the $SiCl_4$ electrolyte bath during electrolysis that ultimately prohibit the application of ec-LPE to the growth of thick contiguous epitaxial Si films.

1.6 Thesis Objectives and Content Description

The work in this thesis can be split into two separate objectives. First, to expand the scope of precursors available to Si electrodeposition, and applicable to ec-LPE, several novel electrolyte baths are explored and interrogated for application in the ec-LLS framework. The second objective of this thesis is the application of Si electrodeposition using electrolyte baths of dissolved Si precursors to the growth of thick Si epitaxial layers under ambient conditions.

Chapter 2 explores the exploration of novel chlorosilane electrolyte baths for their applicability precursors for Si electrodeposition. In this work, the electrochemical response of electrolyte baths composed of hexachlorodisilane and tetrakis(trichlorosilyl)silane were compared to $SiCl_4$ both as a function of temperature and of background salt composition. The presented voltammetry demonstrates that at ambient temperatures all the chlorosilanes have similar electrochemical reduction behaviors and undergo an electroreductive process mediated by a similar electrogenerated intermediate. Under ambient conditions, all chlorosilanes are similarly insensitive to the identity of the background salt. However, despite the amenable low vapor

pressures of Si_2Cl_6 and $Si(SiCl_3)_4$ for electrodeposition of Si at elevated temperatures, neither precursor is advantageous for Si electrodeposition relative to $SiCl_4$ owing to their propensity to decompose. Specifically, the sensitivity of the Si-Si bond in the presence of free Cl^-, a byproduct of Si^0 electrodeposition, is demonstrated and shown to impart, at best, metastability to all electrolyte baths containing Si_2Cl_6 at elevated temperatures. At lower temperatures, while Si_2Cl_6 is suitable for electrodeposition of amorphous Si, a comparable faradaic efficiency to $SiCl_4$ is demonstrated which was not dependent on the concentration, electrolyte identity, or the potential. The electrodeposition of Si_2Cl_6 at a liquid Ga electrode was examined for the growth of crystalline Si by ec-LLS, but yielded only amorphous Si. The absence of crystalline Si indicated that the synthesis of crystalline Si by the ec-LLS mechanism is not universal in Si electrodeposition, and that more mechanistic insight is required for the design of an optimal electrolyte bath.

Chapter 3 elaborates on the electrochemical behavior of the novel pseduohalosilane specie $Si(NCO)_4$ for Si electrodeposition. In this work the voltammetric response of $Si(NCO)_4$ is examined as function of temperature and supporting electrolyte identity. The presented voltammetry demonstrate that $Si(NCO)_4$ is electroactive within the solvent window of propylene carbonate. At ambient temperatures, $Si(NCO)_4$ demonstrated similar electroreductive behaviors to the chlorosilanes. At elevated temperatures, a significant attenuation to the voltammetric response was observed, indicating the participation of additional thermally activated electrogenerated intermediates. The electrochemical response of tetraisocyanatosilane was shown to not strongly depend upon the identity of the anion in the supporting electrolyte. A combination of chronoamperometric, electron microscopy, and X-ray photoelectron spectroscopy data were used to study the morphology and composition of electrodeposited films. At ambient temperatures, the composition and morphology of the as-deposited films were prescriptive of the formation

amorphous Si. At elevated temperatures, the composition of the electrodeposited films was mostly O and C. Attempts to apply tetraisocyanatosilane for crystalline Si synthesis by ec-LLS at a Ga based electrode yielded a polymeric matrix of partially reduced species. Cumulatively, the data demonstrate that while tetraisocyanatosilane can be used for Si electrodeposition under ambient conditions, the thermal activity of byproducts generated from its reduction and its inability to form undergo the ec-LLS process limit its utility.

Chapter 4 details the growth of thin films of epitaxial crystalline Si thin films at ambient temperatures by ec-LPE. This work demonstrates the novel application of a pulsed electrodeposition waveform to sustain epitaxial Si growth in ec-LPE. The single step amperometric response of Si ec-LPE experiments containing electrolyte baths of $SiCl_4$ confirmed previous observations that there is an inevitably short lifetime to the electrodeposition. While a confluence of electron microscopy, electron diffraction, and x-ray diffraction methods demonstrated that the growth of Si epitaxial films by ec-LPE occurs, these films were limited to several hundred nanometers in thickness. Here, the hypothesis that the eventual coalescence of a Si^0 film on the liquid metal surfaces acted as a barrier to further Si^0 dissolution in the melt was tested by the employ of a pulsed electrodeposition waveform. That is, in a cyclical fashion, a short potential step driving the reduction of $SiCl_4$ to Si^0 was followed by a long potential step where no redox occurs to ensure the complete dissolution of Si^0 into the liquid metal electrode. By the application of this pulsed electrodeposition method, the electrodeposition of Si was sustained for hours, rather than minutes, and thick crystalline Si thin films were obtained. Further, using pulsed electrodeposition new thermal benchmarks in epitaxial Si thin film synthesis were set at $T = 23$ ºC, emphasizing the uniqueness of ec-LPE for materials synthesis.

Chapter 5 summarizes additional efforts that remain ongoing. The progress and prospects

of these efforts are discussed.

1.7 References

1. Wen, D.; Gao, W.; Qian, F.; Gu, Q.; Ren, J., Development of solar photovoltaic industry and market in China, Germany, Japan and the United States of America using incentive policies. *Energy Exploration & Exploitation* **2020,** *39* (5), 1429-1456.
2. Looney, B., Statistical Review of World Energy, 2020. *Bp* **2020,** *69*, 66.
3. Singh, J.; Agrahari, A., The progression of silicon technology acting as substratum for the betterment of future photovoltaics. *International Journal of Energy Research* **2019,** *43* (9), 3959-3980.
4. Goodrich, A.; Hacke, P.; Wang, Q.; Sopori, B.; Margolis, R.; James, T. L.; Woodhouse, M., A wafer-based monocrystalline silicon photovoltaics road map: Utilizing known technology improvement opportunities for further reductions in manufacturing costs. *Solar Energy Materials and Solar Cells* **2013,** *114*, 110-135.
5. Saga, T., Advances in crystalline silicon solar cell technology for industrial mass production. *NPG Asia Materials* **2010,** *2* (3), 96-102.
6. Maldonado, S., The Importance of New "Sand-to-Silicon" Processes for the Rapid Future Increase of Photovoltaics. *ACS Energy Letters* **2020,** *5* (11), 3628-3632.
7. Dal Martello, E.; Tranell, G.; Gaal, S.; Raaness, O.; Tang, K.; Arnberg, L., Study of pellets and lumps as raw materials in silicon production from quartz and silicon carbide. *Metallurgical and Materials Transactions B* **2011,** *42* (5), 939-950.
8. Furgal, J. C.; Lenora, C. U., 6. Green routes to silicon-based materials and their environmental implications. In *Green Chemistry in Government and Industry*, De Gruyter: 2020; pp 65-100.
9. Laine, R. M.; Furgal, J. C.; Doan, P.; Pan, D.; Popova, V.; Zhang, X., Avoiding carbothermal reduction: distillation of alkoxysilanes from biogenic, green, and sustainable sources. *Angewandte Chemie* **2016,** *128* (3), 1077-1081.
10. Sakaguchi, Y.; Ishizaki, M.; Kawahara, T.; Fukai, M.; Yoshiyagawa, M.; Aratani, F., Production of High Purity Silicon by Carbothermic Reduction of Silica Using AC-arc Furnace with Heated Shaft. *ISIJ International* **1992,** *32* (5), 643-649.
11. Hühn, C.; Erlebach, A.; Mey, D.; Wondraczek, L.; Sierka, M., Ab Initio energetics of Si-O bond cleavage. *Journal of Computational Chemistry* **2017,** *38* (27), 2349-2353.
12. Chigondo, F., From Metallurgical-Grade to Solar-Grade Silicon: An Overview. *Silicon* **2018,** *10* (3), 789-798.
13. Nguyen, T. T.; Fukaya, N.; Sato, K.; Choi, J.-C.; Kataoka, S., Technoeconomic and environmental assessment for design and optimization of tetraethyl orthosilicate synthesis process. *Industrial & Engineering Chemistry Research* **2018,** *57* (6), 2192-2199.
14. Fu, R.; James, T. L.; Woodhouse, M., Economic Measurements of Polysilicon for the Photovoltaic Industry: Market Competition and Manufacturing Competitiveness. *IEEE Journal of Photovoltaics* **2015,** *5* (2), 515-524.

15. Dal Martello, E.; Tranell, G.; Gaal, S.; Raaness, O. S.; Tang, K.; Arnberg, L., Study of Pellets and Lumps as Raw Materials in Silicon Production from Quartz and Silicon Carbide. *Metallurgical and Materials Transactions B* **2011,** *42* (5), 939.
16. Ye, K.; Wang, J.; Xing, P.; Du, X.; Gao, B.; Kong, J.; Luo, X., Study of the Preparation of High Purity Silicon by a New Electro-thermal Metallurgy Method. *Silicon* **2019,** *11* (3), 1175-1184.
17. Ma, L.; Yu, Z.; Ma, W.; Qing, S.; Wu, J., Assessment and Study on the Impact on Environment by Multi-crystalline Silicon Preparation by Metallurgical Route. *Silicon* **2019,** *11* (3), 1383-1391.
18. Méndez, L.; Forniés, E.; Garrain, D.; Pérez Vázquez, A.; Souto, A.; Vlasenko, T., Upgraded metallurgical grade silicon and polysilicon for solar electricity production: A comparative life cycle assessment. *Science of The Total Environment* **2021,** *789*, 147969.
19. Xie, M.; Ruan, J.; Bai, W.; Qiao, Q.; Bai, L.; Zhang, J.; Li, H.; Lv, F.; Fu, H., Pollutant payback time and environmental impact of Chinese multi-crystalline photovoltaic production based on life cycle assessment. *Journal of Cleaner Production* **2018,** *184*, 648-659.
20. Lee, H.-S.; Suk, J.; Kim, H.; Kim, J.; Song, J.; Jeong, D. S.; Park, J.-K.; Kim, W. M.; Lee, D.-K.; Choi, K. J., Enhanced efficiency of crystalline Si solar cells based on kerfless-thin wafers with nanohole arrays. *Scientific reports* **2018,** *8* (1), 1-12.
21. Bedell, S. W.; Shahrjerdi, D.; Hekmatshoar, B.; Fogel, K.; Lauro, P. A.; Ott, J. A.; Sosa, N.; Sadana, D., Kerf-less removal of Si, Ge, and III–V layers by controlled spalling to enable low-cost PV technologies. *IEEE Journal of Photovoltaics* **2012,** *2* (2), 141-147.
22. Powell, D. M.; Winkler, M. T.; Goodrich, A.; Buonassisi, T., Modeling the cost and minimum sustainable price of crystalline silicon photovoltaic manufacturing in the United States. *IEEE Journal of Photovoltaics* **2013,** *3* (2), 662-668.
23. Wilson, G. M.; Al-Jassim, M.; Metzger, W. K.; Glunz, S. W.; Verlinden, P.; Xiong, G.; Mansfield, L. M.; Stanbery, B. J.; Zhu, K.; Yan, Y.; Berry, J. J.; Ptak, A. J.; Dimroth, F.; Kayes, B. M.; Tamboli, A. C.; Peibst, R.; Catchpole, K.; Reese, M. O.; Klinga, C. S.; Denholm, P.; Morjaria, M.; Deceglie, M. G.; Freeman, J. M.; Mikofski, M. A.; Jordan, D. C.; TamizhMani, G.; Sulas-Kern, D. B., The 2020 photovoltaic technologies roadmap. *Journal of Physics D: Applied Physics* **2020,** *53* (49), 493001.
24. Szeląg-Sikora, A.; Sikora, J.; Niemiec, M.; Gródek-Szostak, Z.; Suder, M.; Kuboń, M.; Borkowski, T.; Malik, G., Solar Power: Stellar Profit or Astronomic Cost? A Case Study of Photovoltaic Installations under Poland's National Prosumer Policy in 2016–2020. *Energies* **2021,** *14* (14).
25. Wang, S., Current status of PV in China and its future forecast. *CSEE Journal of Power and Energy Systems* **2020,** *6* (1), 72-82.
26. Zhang, L.; Chen, C.; Wang, Q.; Zhou, D., The impact of feed-in tariff reduction and renewable portfolio standard on the development of distributed photovoltaic generation in China. *Energy* **2021,** *232*, 120933.
27. Schuman, S.; Lin, A., China's Renewable Energy Law and its impact on renewable power in China: Progress, challenges and recommendations for improving implementation. *Energy policy* **2012,** *51*, 89-109.
28. Wang, F.; Yin, H.; Li, S., China's renewable energy policy: Commitments and challenges. *Energy Policy* **2010,** *38* (4), 1872-1878.
29. Louwen, A.; Van Sark, W.; Schropp, R.; Faaij, A., A cost roadmap for silicon heterojunction solar cells. *Solar Energy Materials and Solar Cells* **2016,** *147*, 295-314.

30. Bardeen, J.; Brattain, W. H., The transistor, a semi-conductor triode. *Physical Review* **1948,** *74* (2), 230.
31. Shimura, F., Single-Crystal Silicon: Growth and Properties. In *Springer Handbook of Electronic and Photonic Materials*, Kasap, S.; Capper, P., Eds. Springer International Publishing: Cham, 2017; pp 1-1.
32. Pfann, W., Techniques of zone melting and crystal growing. *Solid state physics* **1957,** *4*, 423-521.
33. Teal, G. K., Single crystals of germanium and silicon—Basic to the transistor and integrated circuit. *IEEE Transactions on electron devices* **1976,** *23* (7), 621-639.
34. Czochralski, J., Ein neues verfahren zur messung der kristallisationsgeschwindigkeit der metalle. *Zeitschrift für physikalische Chemie* **1918,** *92* (1), 219-221.
35. Dash, W., Improvements on the pedestal method of growing silicon and germanium crystals. *Journal of Applied Physics* **1960,** *31* (4), 736-737.
36. Dash, W. C., Silicon crystals free of dislocations. *Journal of Applied Physics* **1958,** *29* (4), 736-737.
37. Dash, W. C., Growth of silicon crystals free from dislocations. *Journal of Applied Physics* **1959,** *30* (4), 459-474.
38. Jackson, K. A., *Silicon devices: structures and processing*. John Wiley & Sons: 2008.
39. Keck, P. H.; Golay, M. J., Crystallization of silicon from a floating liquid zone. *Physical Review* **1953,** *89* (6), 1297.
40. Chapin, D. M.; Fuller, C. S.; Pearson, G. L., A new silicon p‐n junction photocell for converting solar radiation into electrical power. *Journal of Applied Physics* **1954,** *25* (5), 676-677.
41. Fossum, J.; Burgess, E., High‐efficiency p+‐n‐n+ back‐surface‐field silicon solar cells. *Applied Physics Letters* **1978,** *33* (3), 238-240.
42. Goetzberger, A.; Hebling, C., Photovoltaic materials, past, present, future. *Solar Energy Materials and Solar Cells* **2000,** *62* (1), 1-19.
43. Trentler, T. J.; Hickman, K. M.; Goel, S. C.; Viano, A. M.; Gibbons, P. C.; Buhro, W. E., Solution-liquid-solid growth of crystalline III-V semiconductors: an analogy to vapor-liquid-solid growth. *Science* **1995,** *270* (5243), 1791-1794.
44. D'Asaro, L.; Landorf, R.; Furnanage, R., more slowly than their surroundings and which therefore appear. *Semiconductor Silicon* **1969**, 233.
45. Capper, P.; Mauk, M., *Liquid phase epitaxy of electronic, optical and optoelectronic materials*. John Wiley & Sons: 2007; Vol. 21.
46. Trumbore, F. A., Solid solubilities of impurity elements in germanium and silicon. *Bell System Technical Journal* **1960,** *39* (1), 205-233.
47. Girault, B.; Chevrier, F.; Joullie, A.; Bougnot, G., Liquid phase epitaxy of silicon at very low temperatures. *Journal of Crystal Growth* **1977,** *37* (2), 169-177.
48. Abdou, F.; Fave, A.; Lemiti, M.; Laugier, A.; Bernard, C.; Pisch, A. In *Liquid phase epitaxy of silicon from tin alloys at low temperature*, Conference Record of the Thirty-first IEEE Photovoltaic Specialists Conference, 2005., 3-7 Jan. 2005; 2005; pp 1066-1069.
49. Linnebach, R.; Bauser, E., Low temperature liquid phase epitaxy of silicon. *Journal of Crystal Growth* **1982,** *57* (1), 43-47.
50. Ogawa, H.; Guo, Q.; Ohta, K., Low temperature liquid phase epitaxy of silicon from gallium solution. *Journal of Crystal Growth* **1995,** *155* (3), 193-197.

51. Zhengrong, S.; Young, T. L.; Green, M. A., Low-temperature liquid phase epitaxy of silicon. *Materials Letters* **1991,** *12* (5), 339-343.
52. Baliga, B. J., Silicon Liquid Phase Epitaxy: A Review. *Journal of The Electrochemical Society* **1986,** *133* (1), 5C-14C.
53. Ujihara, T.; Kanda, E.; Obara, K.; Fujiwara, K.; Usami, N.; Sazaki, G.; Alguno, A.; Shishido, T.; Nakajima, K., Effects of growth temperature on the surface morphology of silicon thin films on (111) silicon monocrystalline substrate by liquid phase epitaxy. *Journal of Crystal Growth* **2004,** *266* (4), 467-474.
54. Mauk, M. G.; Curran, J. P., Electro-epitaxial lateral overgrowth of silicon from liquid-metal solutions. *Journal of Crystal Growth* **2001,** *225* (2), 348-353.
55. Konuma, M.; Silier, I.; Gutjahr, A.; Bauser, E.; Banhart, F.; Frey, H.; Nagel, N., Extremely Low Temperature Silicon Liquid Phase Epitaxy. *MRS Proceedings* **2011,** *386*, 339.
56. Rai-Choudhury, P., Gallium doped epitaxial silicon. *Journal of Crystal Growth* **1971,** *8* (2), 165-171.
57. Sumner, B. E.; Foley, R. T., Liquid‐Phase Epitaxial Growth of Gallium‐Doped Silicon. *Journal of The Electrochemical Society* **1978,** *125* (11), 1817-1824.
58. Sukegawa, T.; Kimura, M.; Tanaka, A., LPE growth of silicon by yo-yo solute feeding method. *Journal of Crystal Growth* **1991,** *108* (3), 598-602.
59. Soo Hong, L.; Healy, S. A.; Young, T. L.; Green, M. A., Very-low-temperature liquid-phase epitaxial growth of silicon. *Materials Letters* **1990,** *9* (2), 53-56.
60. Lee, S. H.; Green, M. A., Evaluation of binary and ternary melts for the low temperature liquid phase epitaxial growth of silicon. *Journal of electronic materials* **1991,** *20* (10), 635-641.
61. MAUK, M.; BARNETT, A. In *High efficiency thin-layer silicon solar cells with internal reflection*, EC Photovoltaic solar energy conference. 6, 1985; pp 940-944.
62. Bergmann, R.; Kurianski, J., The role of hydrogen in silicon liquid phase epitaxy. *Materials letters* **1993,** *17* (3-4), 137-140.
63. Bergmann, R.; Robinson, S.; Shi, Z.; Kurianski, J., Silicon films incorporating a drift-field grown by liquid phase epitaxy for solar cell applications. *Solar energy materials and solar cells* **1993,** *31* (3), 447-451.
64. Wang, T.; Ciszek, T. In *Growth kinetics studies of silicon LPE from metal solutions*, Proceedings of 1994 IEEE 1st World Conference on Photovoltaic Energy Conversion-WCPEC (A Joint Conference of PVSC, PVSEC and PSEC), IEEE: 1994; pp 1250-1253.
65. Elwell, D., Electrocrystallization of semiconducting materials from molten salt and organic solutions. *Journal of Crystal Growth* **1981,** *52*, 741-752.
66. Elwell, D.; Feigelson, R. S., Electrodeposition of solar silicon. *Solar Energy Materials* **1982,** *6* (2), 123-145.
67. Lee, C. H.; Kröger, F. A., Cathodic Deposition of Amorphous Alloys of Silicon, Carbon, and Fluorine. *Journal of The Electrochemical Society* **1982,** *129* (5), 936-942.
68. Nishimura, Y.; Fukunaka, Y., Electrochemical reduction of silicon chloride in a non-aqueous solvent. *Electrochimica Acta* **2007,** *53* (1), 111-116.
69. Bechelany, M.; Elias, J.; Brodard, P.; Michler, J.; Philippe, L., Electrodeposition of amorphous silicon in non-oxygenated organic solvent. *Thin Solid Films* **2012,** *520* (6), 1895-1901.
70. Munisamy, T.; Bard, A. J., Electrodeposition of Si from organic solvents and studies related to initial stages of Si growth. *Electrochimica Acta* **2010,** *55* (11), 3797-3803.

71. Gobet, J.; Tannenberger, H., Electrodeposition of Silicon from a Nonaqueous Solvent. *Journal of The Electrochemical Society* **1988,** *135* (1), 109-112.
72. Nicholson, J. P., Electrodeposition of Silicon from Nonaqueous Solvents. *Journal of The Electrochemical Society* **2005,** *152* (12), C795-C802.
73. Agrawal, A. K.; Austin, A. E., Electrodeposition of Silicon from Solutions of Silicon Halides in Aprotic Solvents. *Journal of The Electrochemical Society* **1981,** *128* (11), 2292-2296.
74. Link, S.; Ivanov, S.; Dimitrova, A.; Krischok, S.; Bund, A., Electrochemical deposition of silicon from a sulfolane-based electrolyte: Effect of applied potential. *Electrochemistry Communications* **2019,** *103*, 7-11.
75. Mohan, T. R.; Kröger, F., Cathodic deposition of amorphous silicon from solutions of silicic acid and tetraethyl ortho-silicate in ethylene glycol and formamide containing HF. *Electrochimica Acta* **1982,** *27* (3), 371-377.
76. Gobet, J.; Tannenberger, H., Electrodeposition of silicon from a nonaqueous solvent. *Journal of The Electrochemical Society* **1988,** *135*, 109-112.
77. Ouyang, G.; Gu, M. X.; Fu, S. Y.; Sun, C. Q.; Zhu, W. G., Determination of the Si-Si bond energy from the temperature dependence of elastic modulus and surface tension. *EPL (Europhysics Letters)* **2008,** *84* (6), 66005.
78. El Abedin, S. Z.; Borissenko, N.; Endres, F., Electrodeposition of nanoscale silicon in a room temperature ionic liquid. *Electrochemistry communications* **2004,** *6* (5), 510-514.
79. Shah, N. K.; Pati, R. K.; Ray, A.; Mukhopadhyay, I., Electrodeposition of Si from an ionic liquid bath at room temperature in the presence of water. *Langmuir* **2017,** *33* (7), 1599-1604.
80. Cheng, C.; Zhang, C.; Jiang, J.; Ma, E.; Bai, J.; Wang, J., Raman Spectroscopy Characterization of Dissolved Polysilicon Byproduct SiCl₄ in Ionic Liquids. *Journal of Spectroscopy* **2018,** *2018*, 2329189.
81. Ivanov, S.; Link, S.; Dimitrova, A.; Krischok, S.; Bund, A. In *Electrochemical Nucleation of Silicon in Ionic Liquid-Based Electrolytes*, ECS Meeting Abstracts, IOP Publishing: 2020; p 1181.
82. Link, S.; Dimitrova, A.; Krischok, S.; Bund, A.; Ivanov, S., Electrogravimetry and Structural Properties of Thin Silicon Layers Deposited in Sulfolane and Ionic Liquid Electrolytes. *ACS Applied Materials & Interfaces* **2020,** *12* (51), 57526-57538.
83. Link, S.; Ivanov, S.; Dimitrova, A.; Krischok, S.; Bund, A., Understanding the initial stages of Si electrodeposition under diffusion kinetic limitation in ionic liquid-based electrolytes. *Journal of Crystal Growth* **2020,** *531*, 125346.
84. Thomas, S.; Kowalski, D.; Molinari, M.; Mallet, J., Role of electrochemical process parameters on the electrodeposition of silicon from 1-butyl-1-methylpyrrolidinium bis (trifluoromethanesulfonyl) imide ionic liquid. *Electrochimica Acta* **2018,** *265*, 166-174.
85. Tsuyuki, Y.; Fujimura, T.; Kunimoto, M.; Fukunaka, Y.; Pianetta, P.; Homma, T., Analysis of cathodic reaction process of SiCl4 during Si electrodeposition in ionic liquids. *Journal of The Electrochemical Society* **2017,** *164* (14), D994.
86. Tsuyuki, Y.; Takai, H.; Fukunaka, Y.; Homma, T., Formation of Si thin films by electrodeposition in ionic liquids for solar cell applications. *Japanese Journal of Applied Physics* **2018,** *57* (8S3), 08RB11.
87. Boen, R.; Bouteillon, J., The electrodeposition of silicon in fluoride melts. *Journal of Applied Electrochemistry* **1983,** *13* (3), 277-288.

88. Rao, G. M.; Elwell, D.; Feigelson, R. S., Electrodeposition of Silicon onto Graphite. *Journal of The Electrochemical Society* **1981,** *128* (8), 1708-1711.
89. Zhao, J.; Yin, H.; Lim, T.; Xie, H.; Hsu, H.-Y.; Forouzan, F.; Bard, A. J., Electrodeposition of Photoactive Silicon Films for Low-Cost Solar Cells. *Journal of The Electrochemical Society* **2016,** *163* (9), D506-D514.
90. Zou, X.; Ji, L.; Ge, J.; Sadoway, D. R.; Yu, E. T.; Bard, A. J., Electrodeposition of crystalline silicon films from silicon dioxide for low-cost photovoltaic applications. *Nature Communications* **2019,** *10* (1), 5772.
91. Ma, L.; Lee, S.; DeMuth, J.; Maldonado, S., Direct electrochemical deposition of crystalline silicon nanowires at T ≥ 60 °C. *RSC Advances* **2016,** *6* (82), 78818-78825.
92. Gu, J.; Fahrenkrug, E.; Maldonado, S., Direct Electrodeposition of Crystalline Silicon at Low Temperatures. *Journal of the American Chemical Society* **2013,** *135* (5), 1684-1687.
93. Demuth, J.; Fahrenkrug, E.; Ma, L.; Shodiya, T.; Deitz, J. I.; Grassman, T. J.; Maldonado, S., Electrochemical Liquid Phase Epitaxy (ec-LPE): A New Methodology for the Synthesis of Crystalline Group IV Semiconductor Epifilms. *Journal of the American Chemical Society* **2017,** *139* (20), 6960-6968.
94. Cheek, Q.; Fahrenkrug, E.; Hlynchuk, S.; Alsem, D. H.; Salmon, N. J.; Maldonado, S., In Situ Transmission Electron Microscopy Measurements of Ge Nanowire Synthesis with Liquid Metal Nanodroplets in Water. *ACS Nano* **2020,** *14* (3), 2869-2879.
95. Fahrenkrug, E.; Maldonado, S., Electrochemical Liquid–Liquid–Solid (ec-LLS) Crystal Growth: A Low-Temperature Strategy for Covalent Semiconductor Crystal Growth. *Accounts of Chemical Research* **2015,** *48* (7), 1881-1890.
96. Haarberg, G. M.; Kato, T.; Norikawa, Y.; Nohira, T., Electrodeposition of Silicon with a Liquid Gallium Cathode in Molten Salts. *ECS Transactions* **2019,** *89* (7), 29-35.
97. Zhao, Z.; Yang, C.; Wu, L.; Zhang, C.; Wang, R.; Ma, E., Preparation and Characterization of Crystalline Silicon by Electrochemical Liquid–Liquid–Solid Crystal Growth in Ionic Liquid. *ACS Omega* **2021,** *6* (18), 11935-11942.
98. Demuth, J. Low Temperature Electrodeposition of Epitaxial Films of Covalent Semiconductors. 2017.
99. Gu, J. Low-temperature Electrodeposition of Crystalline Semiconductor Materials. 2014.

Chapter 2

Electroreduction of Perchlorinated Silanes for Si Electrodeposition

Adapted with permission from Downes, N; Cheek, Q. B.; Maldonado, S. "Electroreduction of Perchlorinated Silanes for Si Electrodeposition" J. Electrochem. Soc. **2021**, *168*, 022503

2.1 Introduction

The production of elemental Si is presently dominated by carbothermal reduction of silica.[1-2] This process is energy intensive and involves numerous toxic side-products. Accordingly, strategies for direct, low-temperature electrodeposition of Si have been sought for decades[3-14] because the possibility of economic and environmental advantages exists. To date, just three classes of molecular Si electrodeposition precursors that have been investigated. Siloxanes were reported initially but the stability of the Si-O bonds are not reducible within the potential window of common solvents.[9, 11, 14] Hydrosilanes are reducible but are chemically unstable in air and demonstrate high vapor pressures.[3, 8, 10] Halosilanes are similarly reducible but generally more stable than hydrosilanes. Despite the large compositional space within the halosilane class, predominantly only $SiCl_4$ has been studied in detail.[3, 8, 10, 15-17]

$SiCl_4$ has several advantages and disadvantages as a Si electrodeposition precursor. $SiCl_4$ has a high solubility in solvents such as tetrahydrofuran, acetonitrile, and propylene carbonate.[3, 8, 10, 15-17] However, the thermal range over which $SiCl_4$ can be used is comparatively small since its boiling point (59.2 ºC) is low and its vapor pressure (194 torr at 20 ºC) is high.[18-19] Additionally, despite several reports on the voltammetric responses of $SiCl_4$, the mechanism of $SiCl_4$ reduction

is still not thoroughly detailed. The apparent electroreductive coupling of two molecules of $SiCl_4$ during electroreduction to form larger oligomeric perchlorosilanes at the electrode surface has been proposed.[20]

Identifying different Si electrodeposition precursors has potential utility. Large chlorosilanes are intriguing because they have higher boiling point and lower vapor pressure relative to $SiCl_4$, while retaining chemical moieties which make the latter useful for electrodeposition. This aspect ought to allow for electrodeposition at mild temperatures above room temperature, which could be effectual for emergent Si electrodeposition strategies, such as the electrochemical liquid-liquid-solid process (ec-LLS).[18-19, 21-22] However, at present, there has been no analysis of the electroreduction of larger chlorosilanes. Hence, whether $SiCl_4$ is unique or just one of many potential chlorosilane precursors for Si ec-LLS is not known.

Herein, this work describes the low temperature electroreduction of two chlorosilanes, hexachlorodisilane (Si_2Cl_6) and tetrakis(trichlorosilyl)silane ($Si(SiCl_3)_4$), in propylene carbonate. We focus on propylene carbonate as the solvent of choice for the following reasons. This solvent has already proven fruitful for the ec-LLS growth of crystalline Si particles and nanowires.[18-19] With a high boiling point (242 °C) and polar character, propylene carbonate is simultaneously useful for exploring wider temperature ranges which generally facilitates better crystal growth in ec-LLS and for serving as a comparatively low-resistance medium for performing electrochemical reactions.

The data presented here explore three hypotheses that are germane to the development of Si ec-LLS processes that rely on chlorosilane precursors. First, the voltammetric behavior of chlorosilanes is sensitive to the number of Si-Cl bonds in the chlorosilane precursor. Second, the choice of background salt strongly influences the observable voltammetry but does not strongly

influence the resultant electrodeposited Si film. Third, not all chlorosilanes are universally effective reagents for Si ec-LLS. Electrochemical and electron microscopy data are presented to explore these hypotheses.

2.2 Experimental

Materials $SiCl_4$ (99.99+%, Strem Chemicals), Si_2Cl_6 (99.9%, Gelest) HF (49%, Transene Inc.), gallium (99.999%, Alfa Aesar), hexanes (ACS Grade, Fischer Scientific), methanol (ACS grade, BDH), acetone (ACS grade, BDH), imidazole (99%, Sigma Aldrich), tertbutyldimethylchlorosilane (99%, Oakwood Chemicals), anhydrous THF (99.5%, Sigma Aldrich, extra dry over molecular sieves) were used as received. Propylene carbonate (99.5%, Acros Organics) was purified by a modified method described by Jasinski and Kirkland by first drying by distillation under reduced vacuum at T = 60 ºC in the presence of molecular sieves for 24 hr, and then sparging with dry N_2 at T = 60 ºC for 2 days to remove residual water and trace impurities.[23] The amounts of trace water and organic impurity (allyl alcohol, propylene oxide, propylene glycol) by this method are <10 ppm. Tetrabutylammonium chloride (95%, Alfa Aesar), tetrabutylammonium perchlorate (99%, Alfa Aesar), and tetrabutylammonium tetraphenylborate (99%, Sigma Aldrich) were dried under reduced pressure at T = 80 ºC overnight before bringing into the glovebox. Degenerately doped (i.e. possessing a sufficiently high concentration of electrically active As dopant such that the Fermi level in the bulk was always within $3k_BT$ of the conduction band edge) n^+-Si(100) wafer substrates (<0.007 ohm cm, 0.625 ± 0.020 mm thick) were obtained from University Wafer. Water with a resistivity >18.2 MΩ cm (Barnsted Nanopure) was used throughout.

Silanization of Electrochemical Cells To prevent hydrolysis of the chlorosilanes in the electrolyte bath catalyzed by the protic groups of the glass cell,[24] all glassware was silanized

beforehand. In a borosilicate glass electrochemical cell, imidizaole (1 g, 979 mmol) was dissolved in 15 mL of anhydrous THF at room temperature ($T = 22 \pm 2$°C). The solution was stirred at room temperature for 1 hr. To the stirring solution, tert-butyldimethylchlorosilane (1 g, 416 mmol) was then added. The solution was left stirring for another 12 hr. Following, the solution was removed and the glassware was rinsed thoroughly with methanol to remove any unreacted silane.

Electrochemical Measurements. A Metrohm Autolab PGSTAT302N was employed for all electrochemical measurements and electrodeposition experiments. All electrochemical measurements were performed in a MBraun MB10 drybox. A standard three-electrode configuration with a carbon rod counter electrode with either glassy carbon or n^+-Si(100) as the working electrode and a reference electrode consisting of a Ag wire coated with AgCl immersed in a fritted compartment containing 0.1 M tetrabutylammonium chloride in propylene carbonate. All reported electrochemical potentials are with respect to this electrode, which was externally referenced to ferrocene/ferrocenium periodically in a separate cell to ensure reference electrode stability.

Degenerately doped n^+-Si(100) wafer substrates were diced into approximately 0.6 × 0.6 cm pieces and then degreased with hexanes, acetone, methanol, and water. The wafer sections were then exposed to 5% HF solution for 30s to remove native oxide before use. Electrical contact to n^+-Si(100) electrodes was established by applying a thin layer of InGa eutectic on the back of the wafer and pressing the substrate against a thin stainless steel electrode support.

Si electrodeposition by the ec-LLS method were attempted with a three-electrode configuration, using a 200 μL Ga(l) pool as the working electrode (ca. 0.616 cm^2 active area). Electrical contact to each Ga electrode was made by inserting a section of Pt wire enclosed in the PTFE heat-shrink tubing through the top of the liquid metal pool. A silane-protected glass cell and

vessel were then transferred into a N_2-purged glove box, filled with 14 mL of electrolyte and heated to T = 100 ºC. Electrodepositions were performed under potentiostatic control, with E = -2.5 V vs E(Ag/AgCl). The counter electrode was placed behind a frit to separate the anodic products of electrolysis. After the deposition, the vessel was rinsed three with acetone and methanol, then dried under a stream of N_2 before further analysis.

Materials Characterization. Scanning electron microscopy was performed with a JEOL JSM-7800FLV SEM operated at 15.00 kV. Raman spectra were obtained using a Renishaw Raman microscope spectrometer equipped with a Nikon LU Plan 20x objective (NA = 0.4) and edge filters to reject the 785 nm excitation line. A 785 nm diode laser was used as the incident excitation at a total radiant power of 1.12 mW over a 20 μm^2 incident spot for an integration time of 60 sec.

2.3 Results & Discussion

Voltammetric Analyses of Si_2Cl_6 and $Si(SiCl_3)_4$ Figure 2.1a demonstrates the voltammetric response of 10 mM solutions of $SiCl_4$, Si_2Cl_6, and $Si(SiCl_3)_4$ in 100 mM tetrabutylammonium perchlorate at room temperature (scan rate = 0.1 V s^{-1}). Through comparison with and without Si precursor in the electrolyte bath, the current onset observed at potentials more negative than -1.6 V can be attributed to the reduction of the chlorosilanes. All three precursors exhibited nominally similar reduction responses but with some notable differences. The current onset for the reductions of Si_2Cl_6 and $Si(SiCl_3)_4$ began at -1.6 V. However, for $SiCl_4$, a pre-wave was apparent

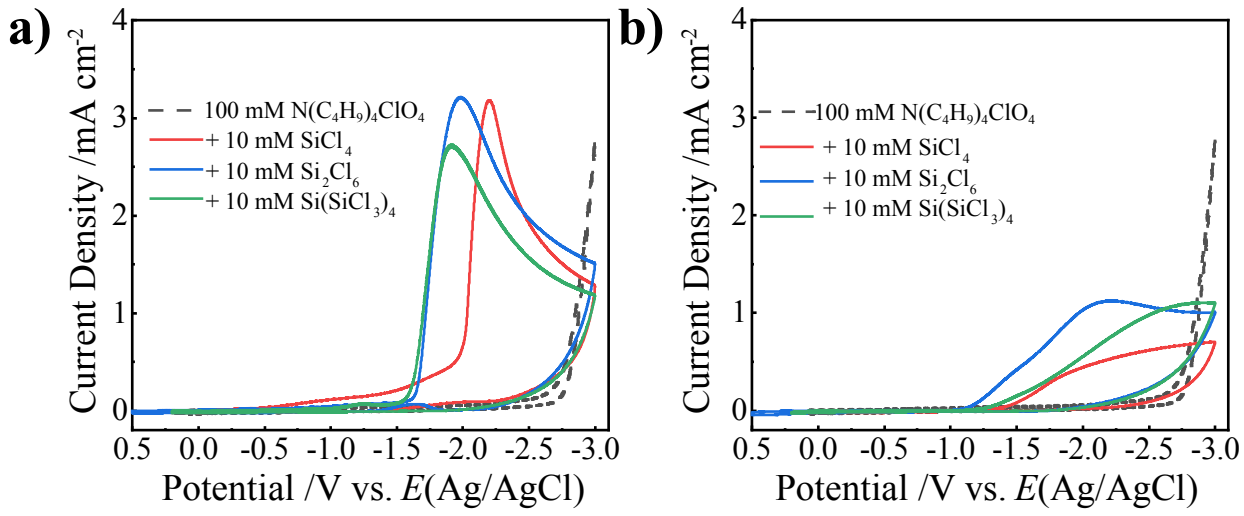


Figure 2.1 Cyclic voltammetric responses for a) the first and b) then second scans for glassy carbon electrodes immersed in propylene carbonate containing 100 mM tetrabutylammonium tetraphenylborate and either (black) no Si precursor, (red) 10 mM $SiCl_4$, (blue) 10 mM Si_2Cl_6, or (green) 10 mM $Si(SiCl_3)_4$. Scan rate = 0.1 V s^{-1}

at potentials more positive than the main voltammetric peak, which was shifted negative by approximately 0.25 V. Previous reports attribute this pre-wave feature in the $SiCl_4$ voltammetry to the reduction of free protons generated through hydrolysis of $SiCl_4$ with trace water in solution.[10] From this vantage point, the data suggested that Si_2Cl_6 and $Si(SiCl_3)_4$ have greater hydrolytic stability. All three chlorosilanes exhibited comparable current densities on the first cycle and similar diminished current densities on the second cycle. The attenuation of the current on the second sweep was indicative of Si electrodeposition onto the electrode, which both increased the operative resistance in the measurement and affected the rate of the reduction reactions. The color of solutions both before and after voltammetric cycling was clear. Since the solubility of $Si(SiCl_3)_4$ was low, these solutions first required heating to promote full dissolution.

The voltammetric responses of $SiCl_4$, Si_2Cl_6, and $Si(SiCl_3)_4$ as a function of scan rate are shown in Figure 2.2. The data in Figures 2.2a-c are normalized with respect to electrode area and the square root of the scan rate with which each voltammogram was obtained. When the rate-determining step in a cathodic voltammetric process is the reduction of a freely diffusing species, normalization of the data in this way should yield voltammograms of the same peak height. As evident in Figure 2.2, there was variation in the peak heights for all three chlorosilane precursors, with the variation being the greatest for $SiCl_4$. With increasing scan rate, all three chlorosilanes exhibited a comparable shift of the reduction peak potential to more negative values. At slower scan rates, $SiCl_4$ exhibited a noticeably diminished current density while Si_2Cl_6 and $Si(SiCl_3)_4$ did not. At slower scan rates for these precursors, the voltammetric wave instead became noticeably sharper. Figure 2.2d compares the peak currents in Figures 2.2a-c as a function of the scan rate. For all three systems, the dependence of current with the square root of the scan rate

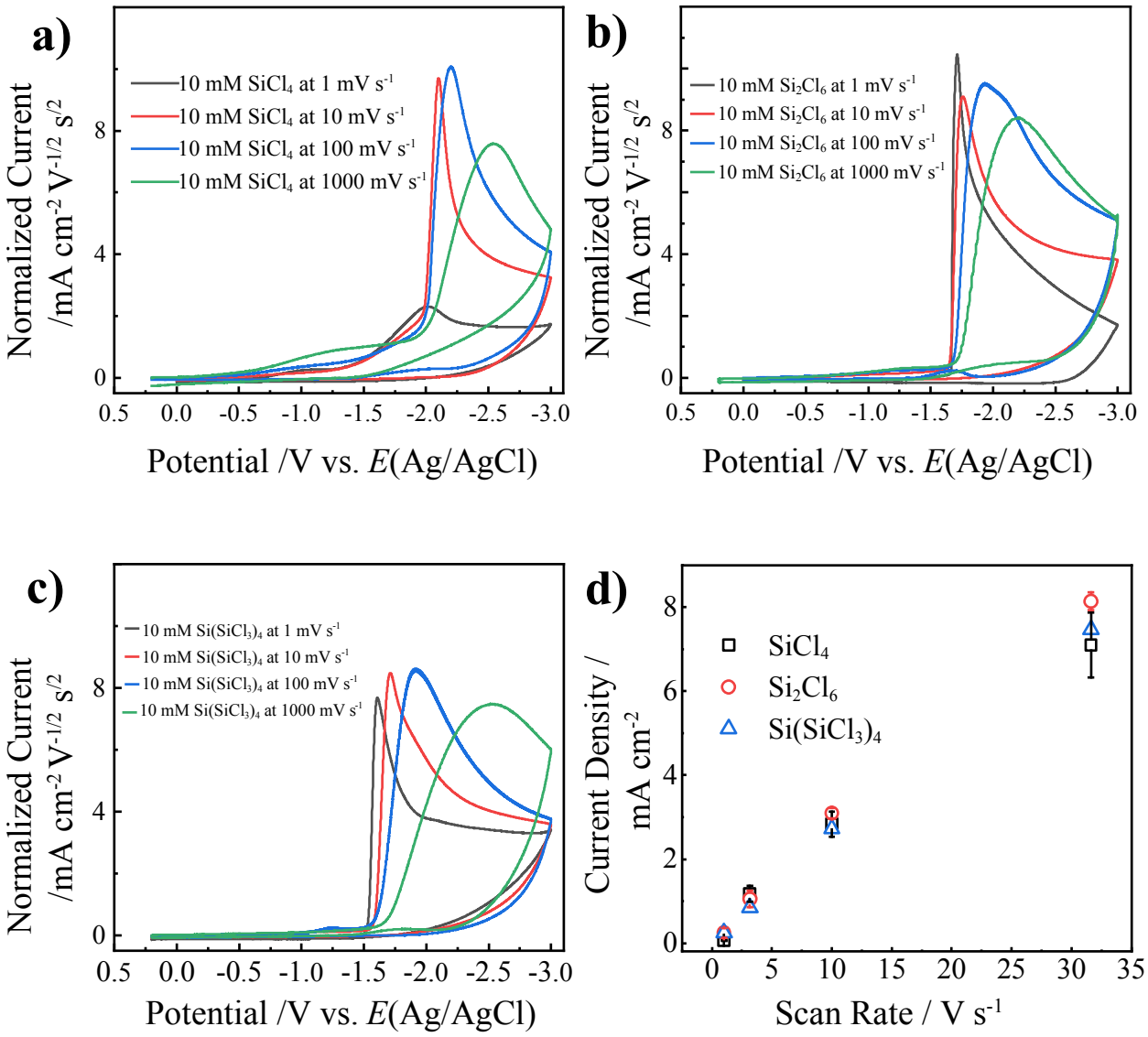


Figure 2.2 Cyclic voltammograms normalized by the square root of the scan rate for glassy carbon electrodes immersed in propylene carbonate containing 100 mM tetrabutylammonium tetraphenylborate and either a) 10 mM $SiCl_4$, b) 10 mM Si_2Cl_6, or c) 10 mM $Si(SiCl_3)_4$. d) Plot showing peak current as a function of scan rate.

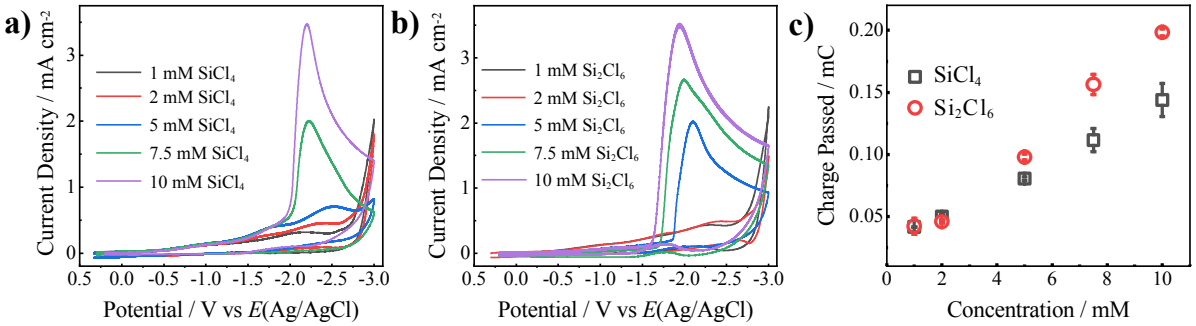


Figure 2.3 Concentration dependent voltammetric profiles for glassy carbon electrodes immersed in propylene carbonate containing 100 mM tetrabutylammonium tetraphenylborate and either 1, 2, 5, 7.5, or 10 mM solutions of either a) $SiCl_4$ or b) Si_2Cl_6. c) Plot showing the total charge passed during voltammetric cyclic in a-b) as a function of the concentration of the chlorosilane. Scan rate = 0.1 V s^{-1}.

was monotonic but not linear. A convex character was evident for the cumulative responses for all three chlorosilanes. An assessment of the dependence of the voltammetric responses for each chlorosilane as a function of concentration was attempted. During the course of these measurements, it became apparent that $Si(SiCl_3)_4$ had limited solubility at room temperature. Prolonged heating at T = 90 °C turned solutions containing $Si(SiCl_3)_4$ a deep orange color and these solutions no longer elicited a voltammetric response. Solutions of $SiCl_4$ and Si_2Cl_3 did not exhibit any color change. Since this solution color was consistent with the disassociation of $SiCl_3^-$ from a parent chlorosilane,[25-26] we inferred $Si(SiCl_3)_4$ was susceptible to homogeneous reactions and thus was not pursued for further analysis.

The concentration-dependent voltammetric responses of $SiCl_4$ and Si_2Cl_6 are shown in Figures 2.3a and 2.3b. At low concentrations, in both systems, no obvious redox wave was observed. However, with increasing concentration, a singular redox peak was resolved. Figure 2.3c shows the charge passed during the voltammetric cycling of $SiCl_4$ and Si_2Cl_6 from 1-10 mM. The quantity of charge passed for chlorosilane electroreduction was determined by first integrating the measured currents obtained during the first forward sweep with and without the chlorosilane precursor and then taking the difference between these two measurements. At lower concentrations, the charge passed for each precursor was roughly equivalent. However, with increasing concentration, the charge passed was 1.5 times greater for Si_2Cl_6 as compared to the charge passed for $SiCl_4$ reduction. This ratio is consistent with the expected ratio for a $6e^-$ redox process for Si_2Cl_6 and a $4e^-$ redox process for $SiCl_4$.

To more fully assess the temperature stability of Si_2Cl_6, Figure 2.4 shows a series of voltammetric responses recorded as a function of time at two different electrolyte temperatures and three different electrolytes that consisted of the same cation (tetrabutylammonium) but

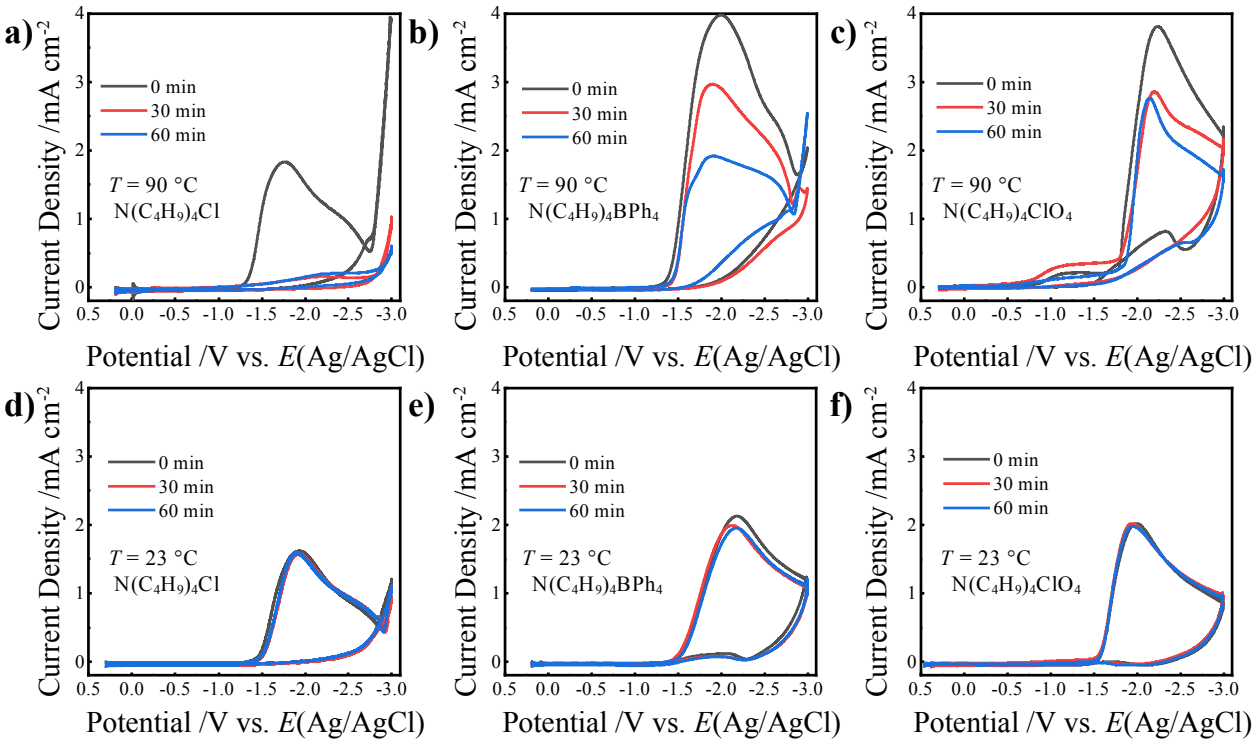


Figure 2.4 Time-dependent cyclic voltammetric responses for glassy carbon electrodes immersed in propylene carbonate containing either 10 mM Si_2Cl_6 and 100 mM a,d) tetrabutylammonium chloride , b,e) tetrabutylammonium tetraphenylborate, or c,f) tetrabutylammonium perchlorate at either a-c) T = 90 ºC or d-f) T = 22 °C. Scan rate = 0.1 V s^{-1}

different anions (Cl^-, ClO_4^-, and BPh_4^-). At room temperature, the voltammetric responses were all similar in shape and remained unchanged after 60 min. At T = 90 ºC, all three sets of voltammetric responses changed over time. When the electrolyte contained free Cl^-, the voltammetric responses for Si_2Cl_6 reduction decreased significantly within 15 mins, with the solution color changing to a deep orange. In the presence of ClO_4^-, the decrease in current magnitude was less severe. In the presence of BPh_4^-, only a minor decrease in the voltammetric current was observed over this period of time. Notably, in electrolytes containing either ClO_4^- or BPh_4^- at T = 90°C, the initial peak currents were larger than the initial peak currents at room temperature.

Si Electrodeposition Figure 2.5 shows cross-section electron micrographs of amorphous Si films electrodeposited onto n^+-Si(100) electrodes from solutions of Si_2Cl_6 at various concentrations at E = -2.5 V vs E(Ag/AgCl), 0.1 M tetrabutylammonium chloride in propylene carbonate for a total charge passed of 25mC at T = 23 °C. Each image highlights the average thickness of the resultant Si thin films resulting from the direct electroreduction of Si_2Cl_6. Figure 2.6 more directly summarizes the measured Si film thicknesses as a function of electrolyte composition at E = -2.5 V. Elemental analyses of films by energy dispersive X-ray spectroscopy confirmed these films were Si but readily converted to SiO_x upon exposure to air, in accord with the well documented instability of electrodeposited amorphous Si in air.[16] Figure 2.6 illustrates that there was no obvious trend in obtained thickness with either concentration, applied potential, or electrolyte anion identity. In all cases, the obtained film thicknesses were much lower than what would be expected if the faradaic efficiency towards Si electrodeposition was 100% (dashed horizontal line in Figure 6). In general, the faradaic efficiency for Si film

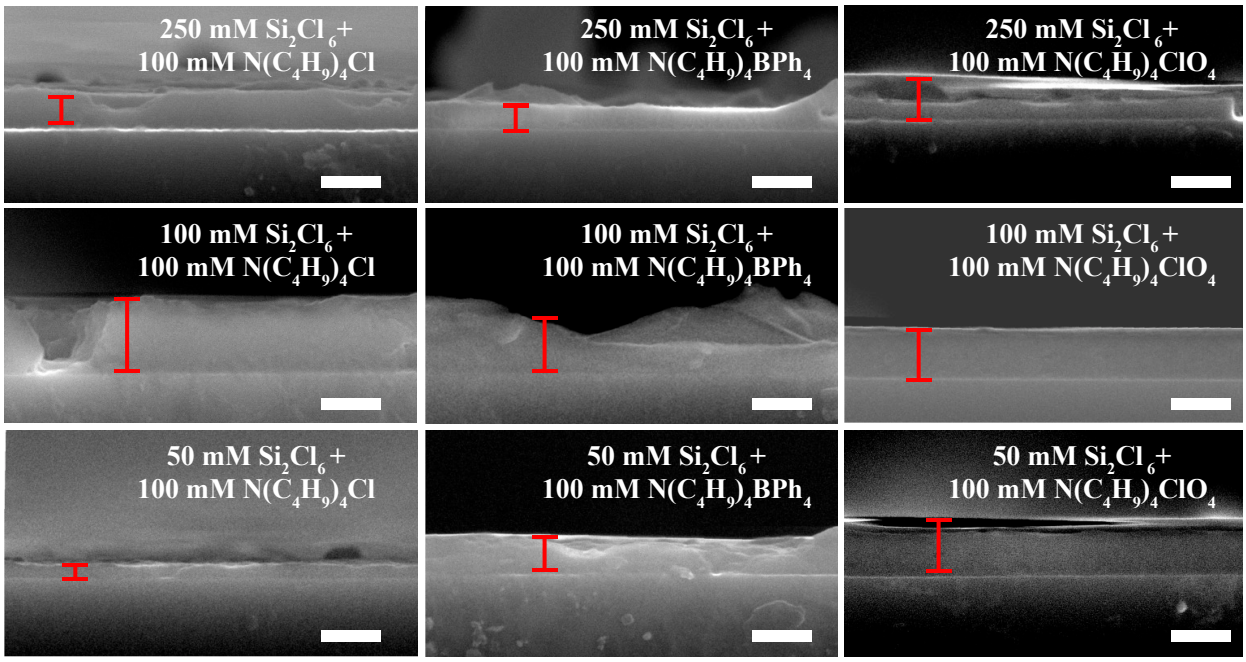


Figure 2.5 Cross-sectional scanning electron micrographs of electrodeposited films prepared on n^+-Si electrodes at E = -2.5 V vs E(Ag/AgCl) as a function of the supporting electrolyte and the formal concentration of Si_2Cl_6. Red vertical bars are a guide to the eye to indicate the average film thickness.

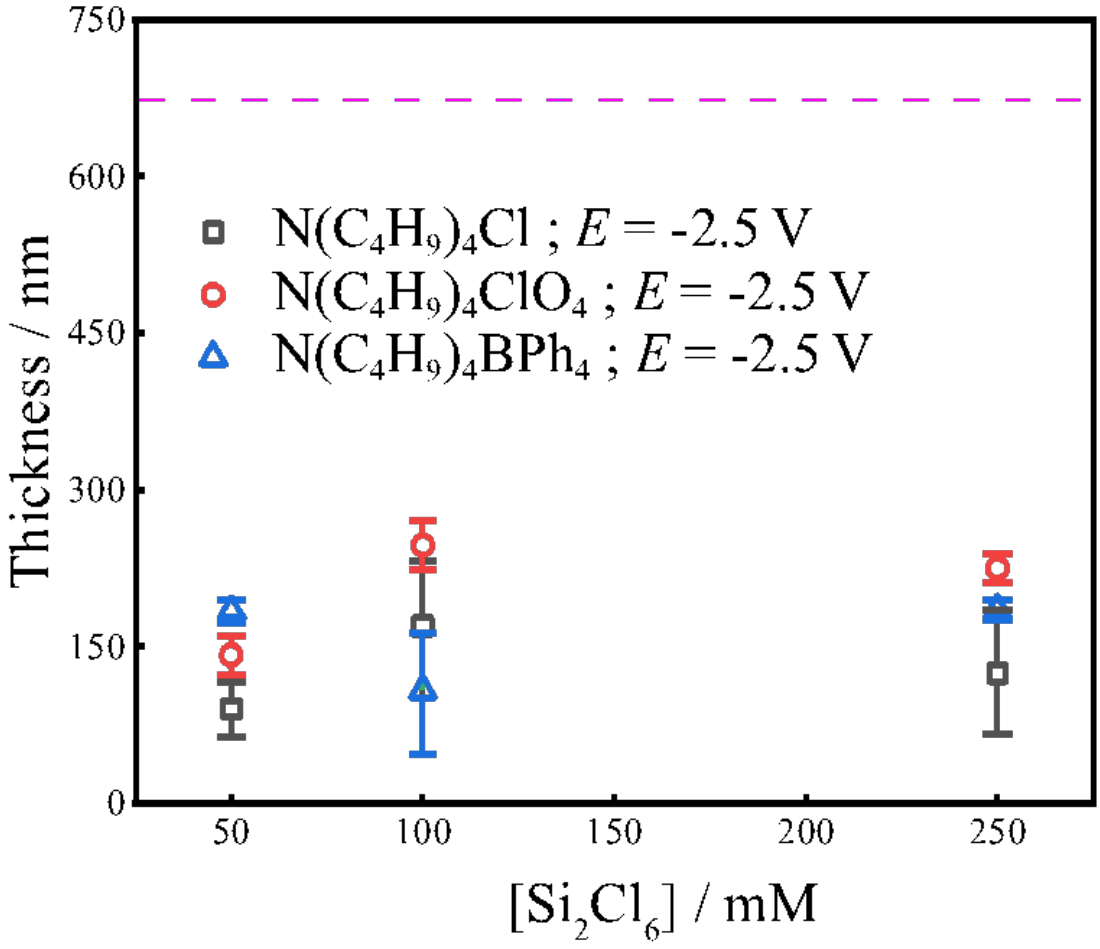


Figure 2.6 Cross-sectional film thicknesses obtained by electroreduction of Si_2Cl_6 as a function of background electrolyte, applied potential, and concentration of Si_2Cl_6. The dotted purple line indicates the expected film thickness for electroreduction of Si_2Sl_6 that results in solid Si^0 with 100% faradaic efficiency.

electrodeposition was low, ≤ 35%, which is comparable to previous reports for Si electrodeposition using $SiCl_4$ in non-aqueous solvents.[8]

Another set of Si electrodeposition trials were performed with liquid metal electrodes to attempt Si ec-LLS. That is, the target of these electrodeposition efforts was the direct electrodeposition of crystalline Si by dissolution of Si^0 immediately after electroreduction, followed by supersaturation of Si in the liquid metal that then triggers nucleation and crystal growth (Figure 2.7a). Figure 2.7b shows the voltammetric responses for $SiCl_4$ and Si_2Cl_6 in 0.1 M $(C_4H_9)_4N$ BPh_4 at a liquid gallium (Ga) pool electrode. Both chlorosilanes elicited a clear enhancement of the current above the current recorded with just the electrolyte, indicating both precursors were reducible with Ga electrodes. Notably, the currents recorded for $SiCl_4$ reduction were uniformly higher than the currents recorded for Si_2Cl_6. Moreover, neither chlorosilane elicited voltammetric behaviors akin to what was observed in Figures 2.1-3. With liquid Ga electrodes, ec-LLS was attempted at -2.5 V. Figures 2.7c,d present photographs of the resultant products obtained for electroreduction of Si_2Cl_6 and $SiCl_4$, respectively. With Si_2Cl_6, electroreduction resulted in a gold-yellow deposit on the surface of liquid Ga (Figure 2.7c). Raman spectra analysis of this material yielded no obvious signature for crystalline Si, instead showing weak, broad peaks centered at 320 cm^{-1} and 480 cm^{-1} that were consistent with the presence of amorphous silicon and/or polysilanes.[19] With $SiCl_4$, a black film was electrodeposited that yielded a strong Raman longitudinal optical phonon mode at 520 cm^{-1} for crystalline Si (inset Figure 2.7d), consistent with what was previously reported for Si ec-LLS.[18-19]

The data presented here speak to three primary points. First, Si_2Cl_6 and $Si(SiCl_3)_4$ exhibit similar electrochemical reactivity towards reduction as $SiCl_4$, implying a common electroactive

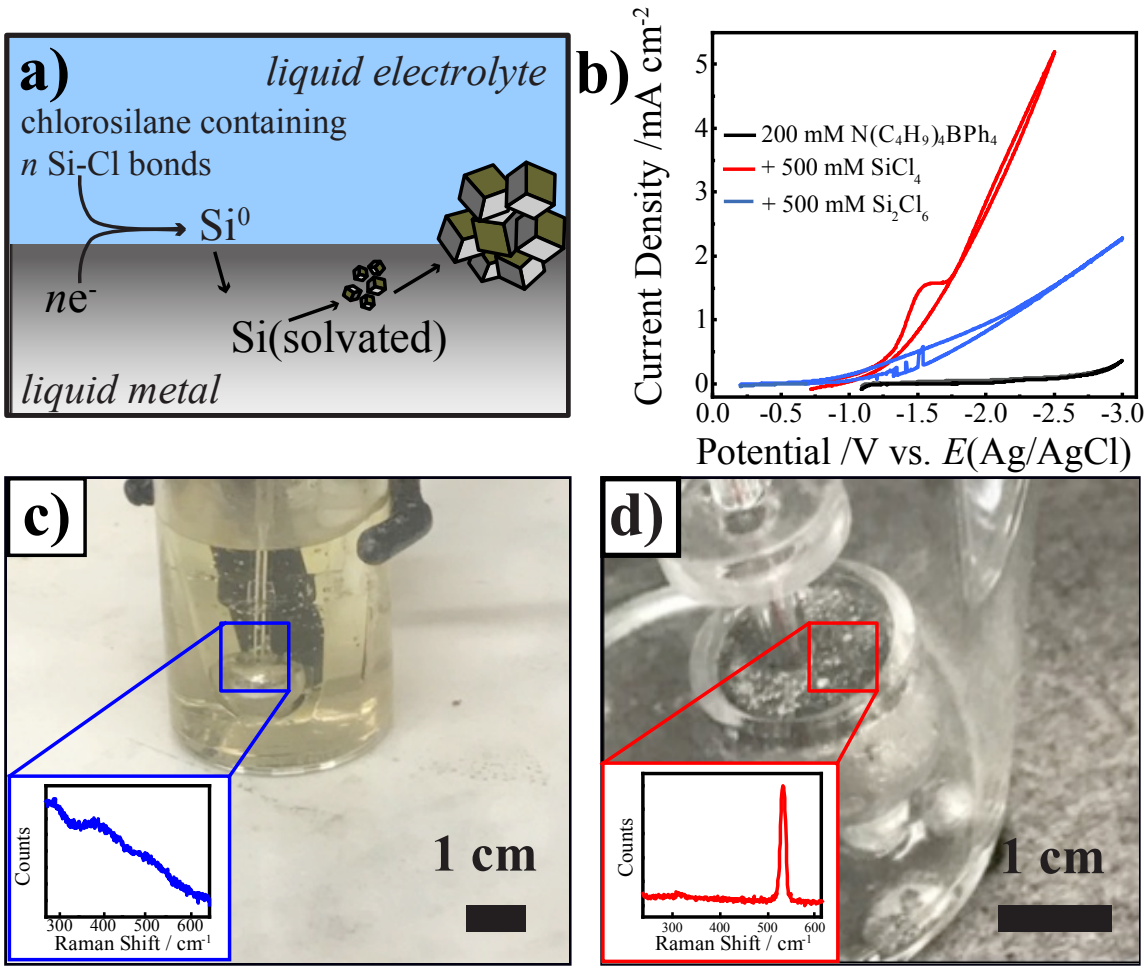


Figure 2.7 a) Schematic depiction (not drawn to scale) of an electrochemical liquid–liquid–solid (ec-LLS) process yielding crystalline Si with a liquid Ga [Ga(l)] electrode. (b) Voltammetric response obtained from 0.5 M solutions of $SiCl_4$ (red) and Si_2Cl_6 (blue) in 0.2 M tetrabutylammonium tetraphenylborate (black) at a gallium pool electrode. Scan rate = 0.1 V s^{-1}. c) and d) show macroscopic images of silicon deposits obtained by ec-LLS performed in c) 0.5 M $SiCl_4$ and d) 0.5 M Si_2Cl_6 in 0.2 M tetrabutylammonium tetraphenylborate electrolytes at E = -2.5 V vs E(Ag/AgCl) for 30 min at 120 ºC. Insets: Raman spectra of the obtained electrodeposited films measured at room temperature.

intermediate. Second, Si_2Cl_6 can be used for the electrodeposition of zero-valent Si on solid electrodes but the faradaic efficiency for electrodeposition is low, presumably due to side-reactions in solution. Third, Si ec-LLS is not possible with Si_2Cl_6 under the same experimental conditions that permit Si ec-LLS with $SiCl_4$.

2.4 Discussion

Electrochemical Reduction of $SiCl_4$, Si_2Cl_6, and $Si(SiCl_3)_4$. The similarity in the general features of the voltammetric data in Figures 1-3 suggest that the electroreductions of all investigated chlorosilanes occur through a similar reaction pathway. At sufficiently concentrated solutions and fast scan rates, the current densities were found to be roughly equivalent for $SiCl_4$, Si_2Cl_6, and $Si(SiCl_3)_4$ at room temperature. These observations imply that the number of electrons passed during the rate-limiting step is the same for all three precursors despite the number of reducible Si-Cl bonds being different in each precursor. Moreover, since a concentration threshold was noted in the observance of a prominent voltammetric wave, we posit that electroreduction is catalyzed by an accumulation of species at the electrode surface upon electroreduction, possibly an adsorbed intermediate given the sharpness of the primary cathodic waves at slow scan rates.

We posit that the key step in electroreduction is the generation of $SiCl_3^-$. If this species is itself the active species for the formation Si^0 or directly involved in the rate-limiting electroreduction process, then the data presented here can be understood more clearly. The diminution of the voltammetric wave at the slowest scan rates only for $SiCl_4$ (Figure 2.22) then is in accord with the idea that $SiCl_4$, Si_2Cl_6 and $Si(SiCl_3)_4$ are all initially reduced to generate $SiCl_3^-$ species in solution and this intermediate is necessary for completing the rest of the multi-electron reduction process. However, accumulation of $SiCl_3^-$ at the electrode occurs more readily with

Si_2Cl_6 and $Si(SiCl_3)_4$ than with $SiCl_4$. Only when $SiCl_3^-$ is accumulated above some threshold concentration do the subsequent reduction steps proceeds similarly for all three chlorosilanes.

Effects of the Background Salt on Si_2Cl_6 Stability The instability of both Si_2Cl_6 and $Si(SiCl_3)_4$ is problematic for electrodeposition at elevated temperatures. We posit that the observed degradation occurs through scission of the Si-Si bond by both the products of the initial electroreduction reduction of the chlorosilanes and also through homogenous reactions with the supporting electrolyte. The synthesis of larger chlorosilanes is known to be complicated in the presence of free Cl^-.[25] Specifically, at elevated temperatures, hypercoordinate $Si_2Cl_7^-$ is formed when Si_2Cl_6 interacts with Cl^-, which subsequently splits into $SiCl_3^-$ and $SiCl_4$. The newly formed $SiCl_4$ is volatile and is lost. $SiCl_3^-$, however, acts as a strong nucleophile, and induces an Aufbau reaction where Si_2Cl_6 is attacked to form $Si_3Cl_9^-$ which undergoes further addition at neutral chlorosilanes in solution to ultimately generate additional $SiCl_4$ and a large array $Si_nCl_{2n+1}^-$ species, owing to the increased anionic stability of the chlorosilanes with increasing chain length.[25-28] The instability of the Cl^- containing electrolyte bath at elevated temperature suggests that the large chlorosilane complexes formed through this pathway are electrochemically inert within the solvent window of propylene carbonate. We posit that the likely degradation pathway for $Si(SiCl_3)_4$ involves $SiCl_3^-$, which undergo subsequent cascading reactions as described above.

In retrospect, given that the electroreduction of chlorosilanes must generate free Cl^-, precursor loss and/or degradation are intrinsic issues. However, the observations in this work suggest that the anions investigated here can also participate in homogenous reactions with chlorosilane. When Si_2Cl_6 was mixed in propylene carbonate containing ClO_4^-, no obvious reaction was noted although silica particles slowly formed over time. This stood in contrast to when ClO_4^- salt was added to neat Si_2Cl_6, where a violent combustion resulted and produced a

deep brown gas. The formation of particulates, in conjunction with the decrease in voltammetric current, is consistent with existing reports of chlorate and chlorosiloxane formation when chlorosilanes are electrolyzed in the presence of ClO_4^-.[24, 29]

For solutions of Si_2Cl_6 containing BPh_4^- at T = 90 °C, the solution changed color over the course of one hour. Although it is difficult to envision nucleophilic attack by BPh_4^-, $(C_4H_9)_4N$ BPh_4^- can itself decompose near 100 ºC.[30-31] If trialkyammonium is formed, this species could coordinate with Si_2Cl_6, leading to disproportionation and rearrangement reactions, as has been reported in the Urry series for oligochlorosilane synthesis.[32] Accordingly, separate work with the alkali metal (Li^+, Na^+, K^+) salts of BPh_4^- was pursued to eliminate this possibility and to investigate the influence of the cation on the electrochemical stability of the chlorosilanes. The voltammetric responses showed a similar current attenuation when periodically monitored at elevated temperature. When these alkali salts were used during electrolysis, however, a considerable accumulation of precipitate was observed and ascribed to the formation of alkali metal chloride salts, which are known to be sparingly soluble in propylene carbonate.[33] Accordingly, these salts were not investigated further due to the complications presented by precipitate accumulation at the electrode surface.

Suitability of Si_2Cl_6 for ec-LLS The inability to generate crystalline Si by ec-LLS with electroreduction of Si_2Cl_6 suggests that the mechanistic steps for ec-LLS with this precursor must be more complex than indicated in Figure 2.7a. Specifically, ec-LLS requires that the electroreduced Si^0 is readily dissolved into the liquid metal. Several reasons are possible that could explain why Si^0 was not appreciably dissolved into, and precipitated out of, liquid Ga.

First, dissolution of Si^0 requires a clean liquid metal/liquid electrolyte interface. Ga electrodes are known to readily form appreciable native oxides readily at ambient pressures.[34-35]

Even within the glove box used to perform ec-LLS in this work, a native oxide presumably formed on the liquid Ga electrodes. In water, the oxide on Ga can be removed electrochemically.[36] It may be possible that $SiCl_4$ facilitates Si ec-LLS in aprotic solvents like propylene carbonate and ionic liquids[18, 37] because it also acts to remove this native oxide. In this work, during the initial stages of electrolysis of $SiCl_4$, the roundness of the Ga pool increased, implying an increase in surface tension possibly from the removal of surface oxide. This same observation was not noted during the electroreduction of Si_2Cl_6 at Ga electrodes. Further, the attenuated voltammetric responses specifically when using the liquid Ga electrode are consistent with the possibility that Si_2Cl_6 does not similarly remove any complicating surface barrier (oxide) layer.

Second, dissolution of a Si cluster containing multiple Si^0-Si^0 bonds may be appreciably slower than dissolution of a discrete Si^0 adatom. Although the electrochemical data are consistent with the formation of a $SiCl_3^-$ species as a key intermediate, the gold-yellow deposit which covered and accumulated over the entire Ga electrode surface is consistent with the electrodeposition of Si^0 species that could not dissolve into Ga rapidly enough. From this vantage point, the data do not necessarily rule out entirely the possibility of ec-LLS with larger chlorosilanes but do implicate the need for designing additional features of the electrolyte and/or the liquid metal to facilitate more rapid dissolution of electrogenerated products that contain Si-Si bonds.

2.5 Conclusions

In this work, the electrochemical reduction of hexachlorodisilane and tetrakis(trichlorosilyl)silane was compared to $SiCl_4$ for the purposes of assessing their suitability as Si electrodeposition precursors. The voltammetry presented here show that Si_2Cl_6 and $Si(SiCl_3)_4$ exhibit similar electrochemical reduction behaviors as $SiCl_4$. However, although both Si_2Cl_6 and

$Si(SiCl_3)_4$ have lower vapor pressures, neither precursor is substantially more advantageous than $SiCl_4$ at elevated temperatures since they are both prone to decomposition processes. At lower temperatures, Si_2Cl_6 was suitable for electrodeposition of amorphous Si, albeit with low faradaic efficiencies that did not depend on the concentration, electrolyte identity, or potential. For electrodeposition of crystalline Si by ec-LLS with liquid Ga, Si_2Cl_6 was not effective and only yielded amorphous Si. The absence of crystalline Si indicated that more mechanistic factors must be considered to design optimal electrolyte/liquid metal combinations for ec-LLS. This work posits that the ability to prevent accumulation of electroreduced product at the liquid metal/liquid electrolyte interface is necessary to widen the scope of Si ec-LLS processes.

2.6 References

1. Lee, J. G.; Miller, P. D.; Cutler, I. B., Carbothermal Reduction of Silica. In *Reactivity of Solids*, Wood, J.; Lindqvist, O.; Helgesson, C.; Vannerberg, N.-G., Eds. Springer US: Boston, MA, 1977; pp 707-711.
2. Maldonado, S., "The Importance of New "Sand-to-Silicon" Processes for the Rapid Future Increase of Photovoltaics." *ACS Energy Letters* **2020,** *5* (11), 3628-3632.
3. Agrawal, A. K.; Austin, A. E., "Electrodeposition of Silicon from Solutions of Silicon Halides in Aprotic Solvents." *Journal of The Electrochemical Society* **1981,** *128* (11), 2292-2296.
4. Boen, R.; Bouteillon, J., "The electrodeposition of silicon in fluoride melts." *Journal of Applied Electrochemistry* **1983,** *13* (3), 277-288.
5. Cohen, U., "Some prospective applications of silicon electrodeposition from molten fluorides to solar cell fabrication." *Journal of Electronic Materials* **1977,** *6* (6), 607-643.
6. Cohen, U.; Huggins, R. A., "Silicon Epitaxial Growth by Electrodeposition from Molten Fluorides." *Journal of The Electrochemical Society* **1976,** *123* (3), 381-383.
7. Elwell, D., "Electrocrystallization of semiconducting materials from molten salt and organic solutions." *Journal of Crystal Growth* **1981,** *52*, 741-752.
8. Gobet, J.; Tannenberger, H., "Electrodeposition of Silicon from a Nonaqueous Solvent." *Journal of The Electrochemical Society* **1988,** *135* (1), 109-112.
9. Kang, D.; Kim, T. W.; Kubota, S. R.; Cardiel, A. C.; Cha, H. G.; Choi, K.-S., "Electrochemical Synthesis of Photoelectrodes and Catalysts for Use in Solar Water Splitting." *Chemical Reviews* **2015,** *115* (23), 12839-12887.
10. Munisamy, T.; Bard, A. J., "Electrodeposition of Si from organic solvents and studies related to initial stages of Si growth." *Electrochimica Acta* **2010,** *55* (11), 3797-3803.

11. Rama Mohan, T. R.; Kröger, F. A., "Cathodic deposition of amorphous silicon from solutions of silicic acid and tetraethyl ortho-silicate in ethylene glycol and formamide containing HF." *Electrochimica Acta* **1982,** *27* (3), 371-377.
12. Rao, G. M.; Elwell, D.; Feigelson, R. S., "Electrowinning of Silicon from K2SiF6 - Molten Fluoride Systems." *Journal of The Electrochemical Society* **1980,** *127* (9), 1940-1944.
13. Rao, G. M.; Elwell, D.; Feigelson, R. S., "Electrodeposition of Silicon onto Graphite." *Journal of The Electrochemical Society* **1981,** *128* (8), 1708-1711.
14. Takeda, Y.; Kanno, R.; Yamamoto, O.; Rama Mohan, T. R.; Lee, C. H.; Kröger, F. A., "Cathodic Deposition of Amorphous Silicon from Tetraethylorthosilicate in Organic Solvents." *Journal of The Electrochemical Society* **1981,** *128* (6), 1221-1224.
15. Bechelany, M.; Elias, J.; Brodard, P.; Michler, J.; Philippe, L., "Electrodeposition of amorphous silicon in non-oxygenated organic solvent." *Thin Solid Films* **2012,** *520* (6), 1895-1901.
16. Nicholson, J. P., "Electrodeposition of Silicon from Nonaqueous Solvents." *Journal of The Electrochemical Society* **2005,** *152* (12), C795-C802.
17. Nishimura, Y.; Fukunaka, Y., "Electrochemical reduction of silicon chloride in a non-aqueous solvent." *Electrochimica Acta* **2007,** *53* (1), 111-116.
18. Gu, J.; Fahrenkrug, E.; Maldonado, S., "Direct Electrodeposition of Crystalline Silicon at Low Temperatures." *Journal of the American Chemical Society* **2013,** *135* (5), 1684-1687.
19. Ma, L.; Lee, S.; DeMuth, J.; Maldonado, S., "Direct electrochemical deposition of crystalline silicon nanowires at T ≥ 60 °C." *RSC Advances* **2016,** *6* (82), 78818-78825.
20. Tsuyuki, Y.; Fujimura, T.; Kunimoto, M.; Fukunaka, Y.; Pianetta, P.; Homma, T., "Analysis of Cathodic Reaction Process of SiCl4 during Si Electrodeposition in Ionic Liquids." *Journal of The Electrochemical Society* **2017,** *164* (14), D994-D998.
21. Cheek, Q.; Fahrenkrug, E.; Hlynchuk, S.; Alsem, D. H.; Salmon, N. J.; Maldonado, S., "In Situ Transmission Electron Microscopy Measurements of Ge Nanowire Synthesis with Liquid Metal Nanodroplets in Water." *ACS Nano* **2020,** *14* (3), 2869-2879.
22. Fahrenkrug, E.; Maldonado, S., "Electrochemical Liquid–Liquid–Solid (ec-LLS) Crystal Growth: A Low-Temperature Strategy for Covalent Semiconductor Crystal Growth." *Accounts of Chemical Research* **2015,** *48* (7), 1881-1890.
23. Jasinski, R. J.; Kirkland, S., "Analysis and distillation of propylene carbonate." *Analytical Chemistry* **1967,** *39* (13), 1663-1665.
24. Hair, M. L.; Hertl, W., "Reactions of chlorosilanes with silica surfaces." *The Journal of Physical Chemistry* **1969,** *73* (7), 2372-2378.
25. Tillmann, J.; Meyer, L.; Schweizer, J. I.; Bolte, M.; Lerner, H.-W.; Wagner, M.; Holthausen, M. C., "Chloride-Induced Aufbau of Perchlorinated Cyclohexasilanes from Si2Cl6: A Mechanistic Scenario." *Chemistry – A European Journal* **2014,** *20* (30), 9234-9239.
26. Tillmann, J.; Wender, J. H.; Bahr, U.; Bolte, M.; Lerner, H.-W.; Holthausen, M. C.; Wagner, M., "One-Step Synthesis of a [20]Silafullerane with an Endohedral Chloride Ion." *Angewandte Chemie International Edition* **2015,** *54* (18), 5429-5433.
27. Teichmann, J.; Bursch, M.; Köstler, B.; Bolte, M.; Lerner, H.-W.; Grimme, S.; Wagner, M., "Trapping Experiments on a Trichlorosilanide Anion: a Key Intermediate of Halogenosilane Chemistry." *Inorganic Chemistry* **2017,** *56* (15), 8683-8688.
28. Olaru, M.; Hesse, M. F.; Rychagova, E.; Ketkov, S.; Mebs, S.; Beckmann, J., "The Weakly Coordinating Tris(trichlorosilyl)silyl Anion." *Angewandte Chemie International Edition* **2017,** *56* (52), 16490-16494.

29. Fuchigami, T., "Electrochemistry of Organosilicon Compounds." *PATAI'S Chemistry of Functional Groups* **2009**.
30. Akhtar, M. N.; Sheikh, S. U., "Analytical pyrolysis of alkylammonium tetraphenylborates." *Journal of thermal analysis* **1994,** *41* (1), 105-114.
31. Sakurai, H.; Morimoto, C.; Hirao, T., "Oxidative Ligand Coupling of Tetraarylborates Promoted by Chlorosilane and Molecular Oxygen." *Chemistry Letters* **2001,** *30* (11), 1084-1085.
32. Kaczmarczyk, A.; Urry, G., "Complexes of disilicon hexachloride with trimethylamine." *Journal of Inorganic and Nuclear Chemistry* **1964,** *26* (3), 415-420.
33. Muhuri, P. K.; Ghosh, S. K.; Hazra, D. K., "Solubilities of some alkali-metal salts, tetraphenylarsonium chloride, and tetraphenylphosphonium bromide in propylene carbonate at 25.degree.C using the ion-selective electrode technique." *Journal of Chemical & Engineering Data* **1993,** *38* (2), 242-244.
34. Regan, M. J.; Tostmann, H.; Pershan, P. S.; Magnussen, O. M.; DiMasi, E.; Ocko, B. M.; Deutsch, M., "X-ray study of the oxidation of liquid-gallium surfaces." *Physical Review B* **1997,** *55* (16), 10786-10790.
35. Xu, Q.; Oudalov, N.; Guo, Q.; Jaeger, H. M.; Brown, E., "Effect of oxidation on the mechanical properties of liquid gallium and eutectic gallium-indium." *Physics of Fluids* **2012,** *24* (6), 063101.
36. Wang, J.; Appusamy, K.; Guruswamy, S.; Nahata, A., "Electrolytic reduction of liquid metal oxides and its application to reconfigurable structured devices." *Scientific Reports* **2015,** *5* (1), 8637.
37. Zhang, J.; Chen, S.; Zhang, H.; Zhang, S.; Yao, X.; Shi, Z., "Electrodeposition of crystalline silicon directly from silicon tetrachloride in ionic liquid at low temperature." *RSC Advances* **2016,** *6* (15), 12061-12067.

Chapter 3

Electroreduction of $Si(NCO)_4$ for Si Electrodeposition

Downes, N.; Vasquez, R.; Maldonado, S. "Electroreduction of $Si(NCO)_4$ for Si Electrodeposition". *Submitted for Publication*

3.1 Introduction

The electrodeposition of elemental Si at low temperatures has been of technical interest for decades[1] because it is potentially both economically advantageous and environmentally benign. Many classes of electrodeposition precursors have been investigated over the years. For example, hydrosilanes are electrochemically active but are easily combusted and otherwise difficult to handle.[2] Conversely, siloxanes are easy to handle but difficult, if not impossible, to reduce within the potential window of commonly available organic solvents.[3-4] Silicates can only be reduced at elevated temperatures.[5-7] Halogenated silanes have been studied, though among them, only $SiCl_4$ has been examined extensively.[2, 8-16] $SiCl_4$ has several advantages and disadvantages as a Si electrodeposition precursor. First, $SiCl_4$ is less hazardous than hydro- or hydrohalosilanes ($SiHX_3$) and more stable under electrolysis than $SiBr_4$ and SiI_4.[13-15] Nevertheless, upon exposure to air, $SiCl_4$ still hydrolyzes and liberates substantial heat and gaseous HCl. Second, $SiCl_4$ is highly soluble and reducible within the solvent window of several electrolyte systems. Substantial data exist for the electrochemistry of $SiCl_4$ in propylene carbonate,[10, 15, 17] tetrahydrofuran,[13-15] acetonitrile,[13] sulfolane[9] and various ionic liquids.[18-20] However, the low boiling point (56 ºC) and high vapor pressure (194 torr at 20 ºC) of $SiCl_4$

complicate the study of its electrochemistry over large temperature ranges.[21-22] Accordingly, additional Si precursors that are similarly reducible but with more favorable physicochemical properties would be useful.

Identifying different precursors has potential utility in reviving a broader interest in Si electrodeposition. Recently, an emergent strategy, called electrochemical liquid-liquid-solid (ec-LLS) growth, has been demonstrated for the low temperature electrodeposition of single crystalline covalent and inorganic materials.[8, 23-24] Si ec-LLS was performed using $SiCl_4$ but the cumulative data suggest that there is a short electrodeposition window before the bath becomes inert and prevents any further ec-LLS. Thus, prospects for advancing Si ec-LLS would benefit strongly from the discovery of new, viable precursors for Si electrodeposition. In particular, precursors that are stable over a wide range of temperatures would be beneficial for exploring the metallurgical aspects of crystal growth in ec-LLS.

The pseudohalosilane tetraisocyanatosilane ($Si(NCO)_4$) is one potential candidate precursor. This compound has not yet been explored in any context for Si electrodeposition. However, its high boiling point (186 ºC) and lower vapor pressure (0.4 Torr at 30 ºC) [25] are attractive and suggest it might be easier to handle than $SiCl_4$. $Si(NCO)_4$ as a precursor for vapor-phase deposition of Si-containing materials has been explored, as it is used in low temperature chemical vapor deposition of *a*-SiO_2.[26-27] Though the pseudohalide functional group is similar to halogens in some homogeneous chemistry, it is unclear whether $Si(NCO)_4$ is electrochemically active and can be electroreduced to Si^0.

Herein, this work describes the electroreduction of $Si(NCO)_4$ in propylene carbonate to explore the general efficacy of its used for Si electrodeposition. The data presented here explore three hypotheses germane to expanding the development of Si ec-LLS. First, $Si(NCO)_4$ is

electroactive within the solvent window of propylene carbonate. Second, the electroreduction of $Si(NCO)_4$ is insensitive towards the supporting electrolyte identity. We have previously shown the effect of anion identity on the electroreduction of chlorosilanes, noting that subtle aspects irrelevant to the general electrochemical parameters of a cell are vitally important to possible homogeneous chemistry before, during, and after electroreduction.[17] Here, we explore the use of two electrolytes that only differ in the reactivities of the anions towards Si compounds. Cl^- is a strong nucleophile, which can promote parasitic side-reactions in the reduction of silanes.[28-29] BPh_4 is a weak, sterically hindered Lewis base that should be unreactive. Third, $Si(NCO)_4$ facilitates Si crystal growth in liquid Ga electrodes via ec-LLS. Electroanalytical and materials characterization data are presented here to explore these hypotheses.

3.2 Experimental

Materials $Si(NCO)_4$ (99.99+%, Gelest), HF (49%, Transene Inc.), gallium (99.999%, Alfa Aesar), indium (99.999%, American Elements), hexanes (ACS Grade, Fischer Scientific), methanol (ACS grade, BDH), acetone (ACS grade, BDH), imidazole (99%, Sigma Aldrich), tertbutyldimethylchlorosilane (99%, Oakwood Chemicals), anhydrous THF (99.5%, Sigma Aldrich, extra dry over molecular sieves) were used as received. Propylene carbonate (99.5%, Acros Organics), tetrabutylammonium chloride (95%, Alfa Aesar) and tetrabutylammonium tetraphenylborate (99%, Sigma Aldrich) were purified according to our previously reported method.[17] Degenerately doped n^+-Si(100) wafer substrates (<0.007 ohm cm, 0.625 ± 0.020 mm thick) were obtained from University Wafer. Water with a resistivity >18.2 MΩ cm (Barnsted Nanopure) was used throughout.

Electrochemical Measurements A Metrohm Autolab PGSTAT302N was employed for all electrochemical measurements and electrodeposition experiments. Electroanalyses were

performed in a controlled, inert atmosphere within a MBraun MB10 drybox. A standard three-electrode configuration with a carbon rod counter electrode with n^+-Si(100) as the working electrode and a reference electrode consisting of a Ag wire coated with AgCl immersed in a fritted compartment containing 0.1 M tetrabutylammonium chloride in propylene carbonate. All reported electrochemical potentials are with respect to this electrode, which was externally referenced to ferrocene/ferrocenium periodically in a separate cell to ensure reference electrode stability. Degenerately doped n^+-Si(100) wafer substrates were diced into smaller pieces (~0.6 × 0.6 cm^2) and then degreased under sonication in hexanes, acetone, methanol, and water. These wafer sections were then exposed to 5% HF solution for 30 s to remove native oxide before use. Ohmic contacts to these platforms were prepared by applying a thin layer of eutectic GaIn (*e*-GaIn) on the backside and then pressing the substrate against a thin stainless steel electrode support. To combat the possibility of hydrolysis of $Si(NCO)_4$ with exposed hydroxyl groups on the surfaces of the glass cell, all glassware was silanized beforehand as described previously,[17] including glassware used to prepare electrolytes. Si electrodeposition by the ec-LLS method was attempted with a three-electrode configuration, using a 200 μL *e*-GaIn pool as the working electrode (ca. 0.616 cm^2 active area). Electrical contact to each *e*-GaIn electrode was made by inserting a section of Pt wire enclosed in the PTFE heat-shrink tubing through the top of the liquid metal pool. A silanized glass cell and vessel were then transferred into a N_2-purged glove box, filled with 14 ml of electrolyte and heated to T = 150 °C. Electrodepositions were performed under potentiostatic control, with E = −2.5 V vs E(Ag/ AgCl) when n^+-Si(100) was used as the working electrode, and E = −1.6 V vs E(Ag/ AgCl) when *e*-GaIn was used as the working electrode. Upon completion, the working electrodes were rinsed three times with acetone and methanol, then dried under a stream of N_2 before further analysis.

Materials characterization.—Scanning electron microscopy was performed with a JEOL JSM-7800FLV SEM operated at 15.00 kV. Raman spectra were obtained using a Renishaw Raman microscope spectrometer equipped with a Nikon LU Plan 20x objective (NA = 0.4) and edge filters to reject the 785 nm excitation line. A 785 nm diode laser was used for excitation at a total radiant power of 1.12 mW over a 20 μm^2 incident spot for an integration time of 60 s. A PHI 5400 X-ray photoelectron analyzer was used with a nonmonochromatic Al Kα (1486.6 eV, 6 mA current emission, 12 kV anode high tension) source to collect spectra. A pressure of $< 2.5 \times 10^{-9}$ Torr was used for spectral acquisition without any charge neutralization. Survey scans were collected from 0 to 1350 eV with a pass energy of 117.40 eV and a take-off angle of 54.6°. High-resolution scans were collected at a pass energy of 23.5 eV. All binding energies were referenced to adventitious carbon (284.6 eV). Data analyses of XP spectra were performed using CASA XPS 2.3.13 software.

3.3 Results

Voltammetric Analysis of $Si(NCO)_4$ Figure 3.1a-b) demonstrates the voltammetric response of $Si(NCO)_4$ with a degenerately doped *n*-Si(100) electrode as a function of the supporting electrolyte identity and the temperature (*T*) of the bath. In these data, the concentration of $Si(NCO)_4$ and scan rate are held constant. Voltammetric measurements with and without $Si(NCO)_4$ in both electrolyte baths highlighted that the current onset near E = -1.4 V was for a reduction process associated with $Si(NCO)_4$. Both electrolyte baths exhibited nominally similar responses, i.e. current magnitude and wave shape, indicating the rate-determining aspect of the electroreduction was not radically different in the presence of the different supporting electrolytes. When the electrolyte bath was heated to 150 ºC, the current magnitude increased by roughly a factor of 2. At all temperatures and both electrolyte baths, the current magnitude was small, relative

to reported results for $SiCl_4$ at the same concentration, and presented no obvious peak indicative of the transition between kinetic and diffusion controlled current.[13]

At room temperature, both electrolytes were clear before and after measurements. After experiments at T = 150 ºC, both the Cl^- and BPh_4^- containing electrolytes turned pale yellow color,

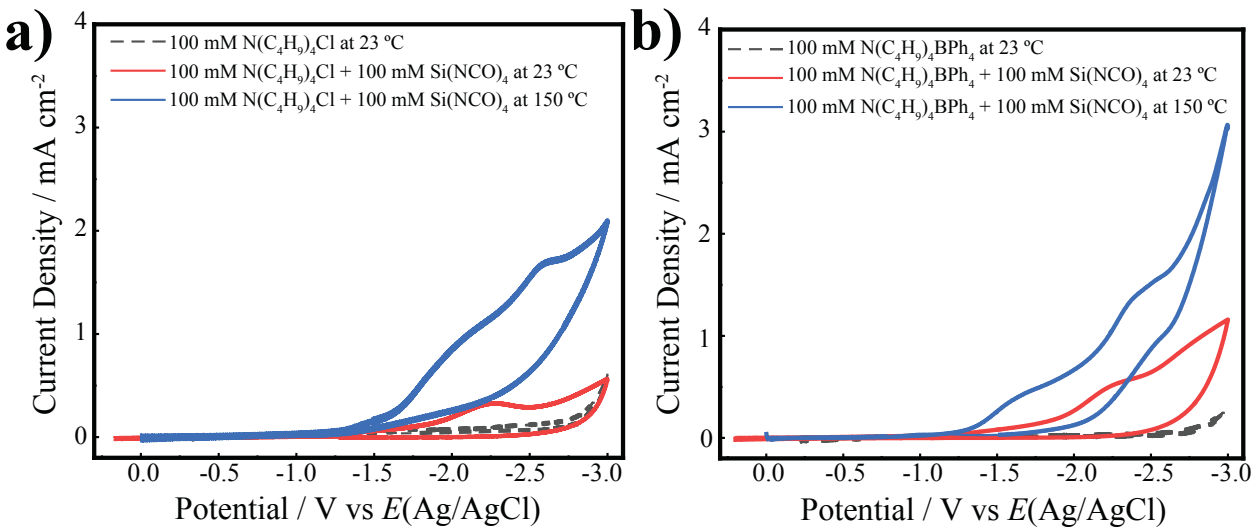


Figure 3.1 Temperature dependent voltammetric profiles for n^+-Si electrodes immersed in propylene carbonate containing either (dashed black line) no precursor or 0.1 M solutions of $Si(NCO)_4$ at T = (solid red line) 23 or (solid blue line) 150 ºC for baths containing a) 0.1 M tetrabutylammonium chloride and b) 100 mM tetrabutylammonium tetraphenylborate solutions. Scan rate = 100 mV s^{-1}

consistent with reductive decomposition of propylene carbonate.[30-31] When both solutions were heated but without any electrochemical measurement performed, no change in color was observed, indicating that the product of electroreduction undergoes a more facile homogeneous reaction in solution at the higher temperature.

The concentration-dependences of the voltammetric responses for $Si(NCO)_4$ electroreduction are shown in Figure 3.2. The data in Figure 3.2a,b) represent voltammetry collected at room temperature in BPh_4^- and Cl^- electrolytes, respectively. At low concentrations, no clear faradaic current response was observed in either electrolyte solution. At higher concentrations, the observed currents were still uniformly small, with the same voltammetric wave shapes in both electrolytes. These features were consistent with an electroreduction reaction not limited by the diffusive transport to the electrode surface. Instead, the lack of sharp peak shapes for any concentration implied a slow, kinetically-limited redox process.

The data in Figures 2c,d) present the corresponding voltammetric responses collected at T =150 ºC. In the Cl^- based electrolyte, no significant redox response was observed at 1 mM $Si(NCO)_4$. In both electrolyte baths, the current magnitude and wave shape were nominally the same. At higher concentrations of $Si(NCO)_4$, two small peaks were observed near E = -1.5 and -2.2 V.

The influence of scan rate is shown in Figure 3.3. The data presented in Figures 3a-d are normalized to the square root of the scan rate. In this normalized format, a diffusion-limited redox process would appear the same at every scan rate. At T = 23 ºC, the normalized voltammetric

responses of $Si(NCO)_4$ in both electrolyte solutions were roughly similar at fast scan rates but at slow scan rates the currents were attenuated and exhibited a large hysteresis. Interestingly, although both the Cl^- and BPh_4^- electrolytes had the same purity level, only the Cl^- containing

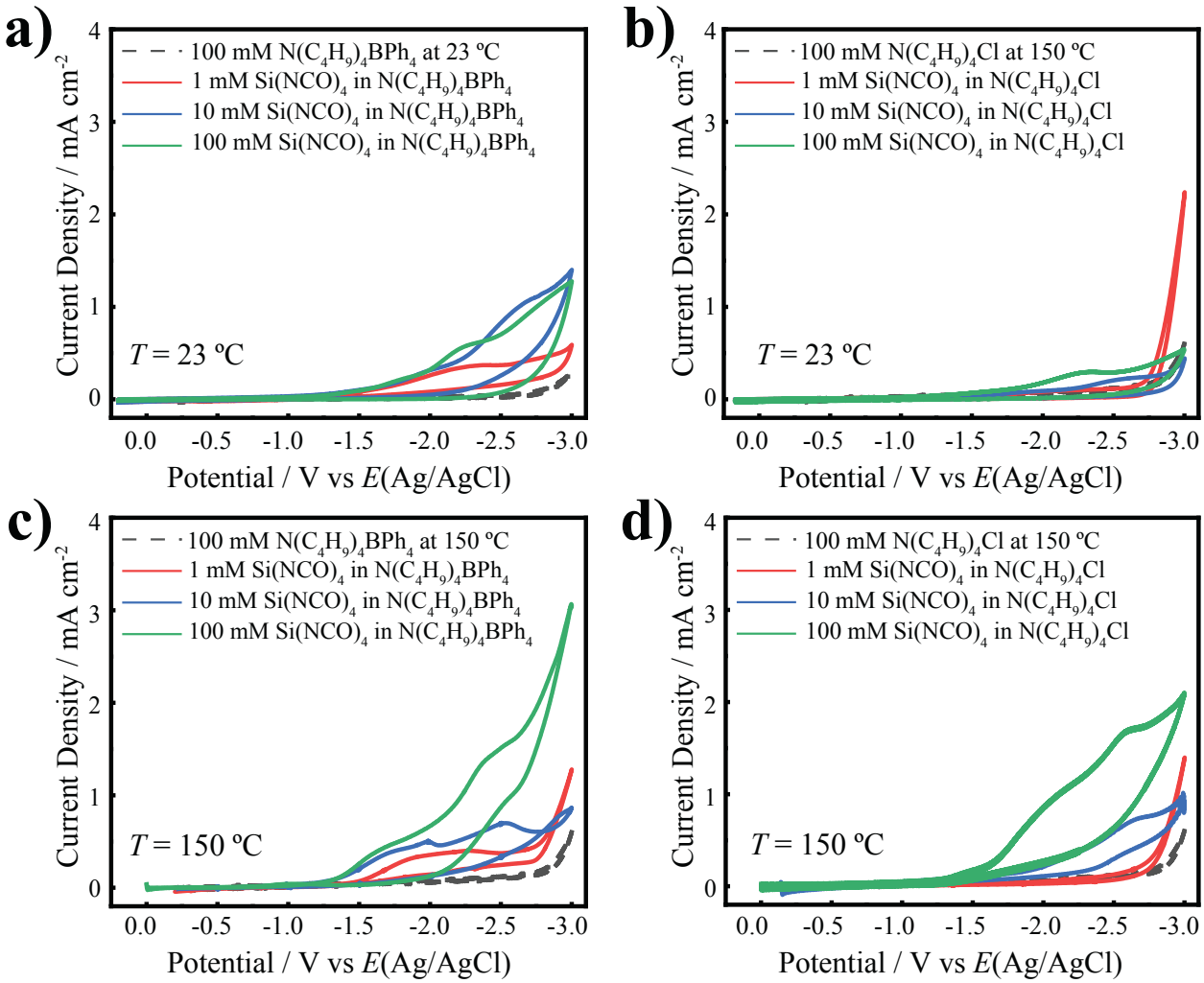


Figure 3.2 Concentration dependent voltammetric profiles for n^+-Si electrodes immersed in propylene carbonate for 0.001, 0.01, and 0.1 M solutions of $Si(NCO)_4$ at T = 23 and 150 ºC for baths containing a,c) 0.1 M tetrabutylammonium tetraphenylborate and b,d) 0.1 M tetrabutylammonium chloride solutions, respectively. The blank voltammetric responses in the absence of $Si(NCO)_4$ are denoted with dashed black lines. Scan rate = 100 mV s^{-1}.

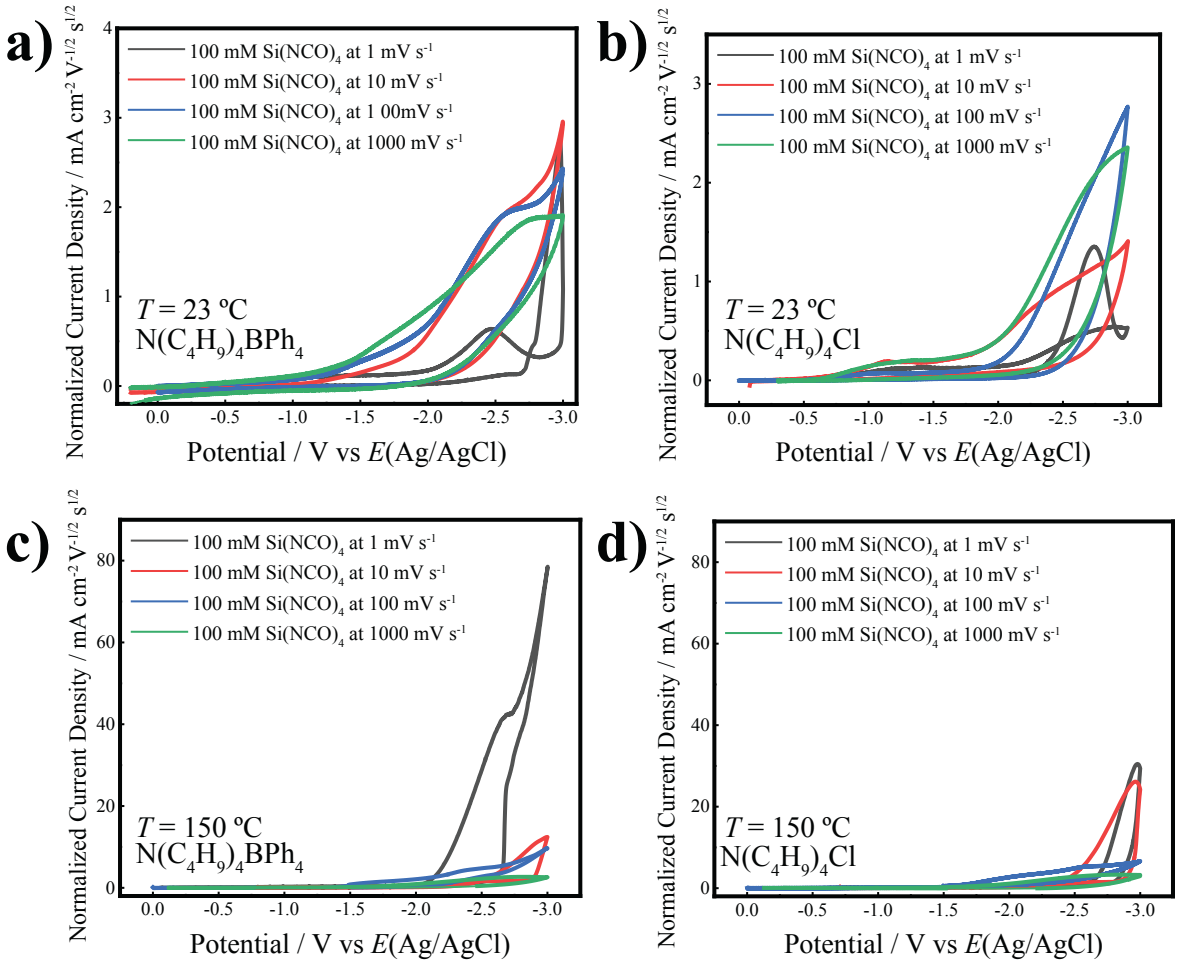


Figure 3.3 Cyclic voltammograms normalized by the square root of the scan rate for n^+-Si electrodes immersed in propylene carbonate containing 0.1 M $Si(NCO)_4$ at T = 23 and 150 ºC and a,c) 0.1 M tetrabutylammonium tetraphenylborate and b,d) 0.1 M tetrabutylammonium chloride solutions, respectively.

solution exhibited the pre-wave feature starting at E = -0.6 V previously ascribed to the reduction of trace protic sources in the electroreduction of chlorosilanes.[13, 15, 17, 32] Since $Si(NCO)_4$ is known to be relatively hydrolytically stable, we posit that it is associated with the presence of free Cl^- rather than decomposition of $Si(NCO)_4$. At T = 150 ºC, the normalized voltammetric responses strongly changed at each scan rate. Slow scan rates elicited a significantly larger normalized current response, with the deviation considerably larger in the presence of BPh_4^- than Cl^-.

Chronoamperometry of $Si(NCO)_4$ Figure 3.4a) presents the chronoamperometric responses of 100 mM $Si(NCO)_4$ at E = -2.5 V E(vs Ag/AgCl) for t =30 min. These data were collected as a function of electrolyte composition and temperature in order to assess the capacity for bulk Si electrodeposition. A chronoamperometric response for an electrodeposition process at a large overpotential, four aspects are expected in the current-time profiles. (*1*) A local minimum of the current following the dissipation of the charging current owing to nucleation which depletes the precursor near the electrode surface should be observed. (*2*) A rise in current attributable to the generation and growth of nuclei should follow. (*3*) A local maximum of the current occurs as the radial diffusional fields of the individual nucleated crystallites coalesce, resulting in a contiguous film. (*4*) The current then decreases as electrodeposition becomes limited by linear diffusion of precursors to the growing film.[33]

The solid and dashed traces in Figure 3.4a) illustrate the current-time transients collected at E = -2.5 V vs E(Ag/AgCl) and at T = 150 and 23 ºC, respectively. As with the voltammetry, the current transient showed minimal current in both electrolyte solutions, resulting in minimal total charge passed. Moreover, not all of the aforementioned four features were cleanly observable in the data. In both electrolyte solutions, the current-time transient exhibited the first three features

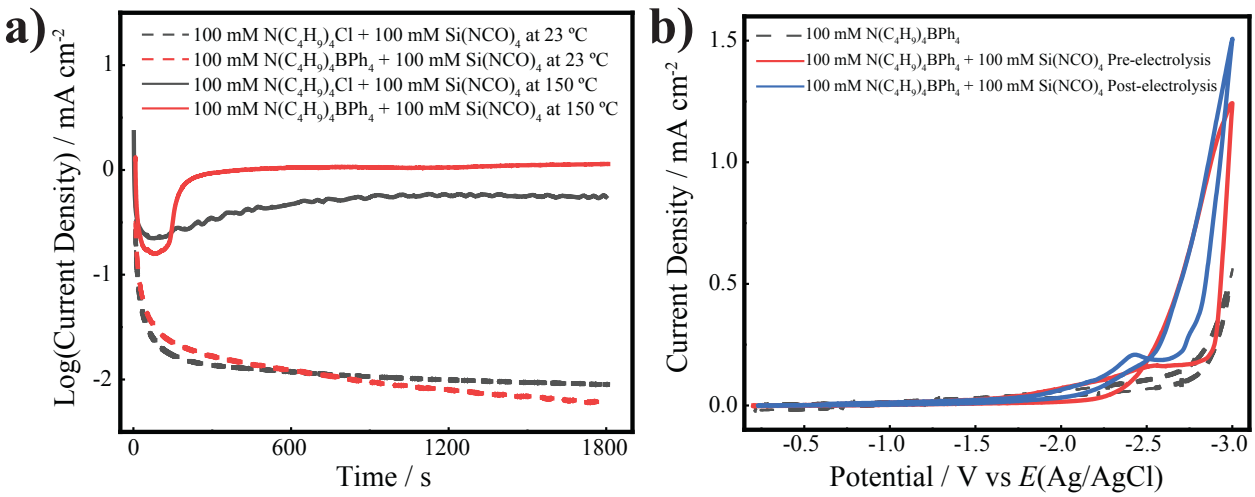


Figure 3.4 a) Chronoamperometric response at E = -2.5 V vs E(Ag.AgCl) of n^+-Si electrodes immersed in propylene carbonate containing 0.1 M $Si(NCO)_4$ at T = (dashed lines) 23 and (solid lines) 150 ºC and with either (black lines) 100 mM tetrabutylammonium tetraphenylborate or (red lines) 100 mM tetrabutylammonium chloride solutions. b) Cyclic voltammetric response of n^+-Si electrodes in solutions containing 0.1 M $Si(NCO)_4$ in 0.1 M tetrabutylammonium tetraphenylborate solution (red) before and (blue) after electrolysis at E = -2.5 V vs E(Ag.AgCl) at 150 ºC. Scan rate = 10 mV s^{-1}.

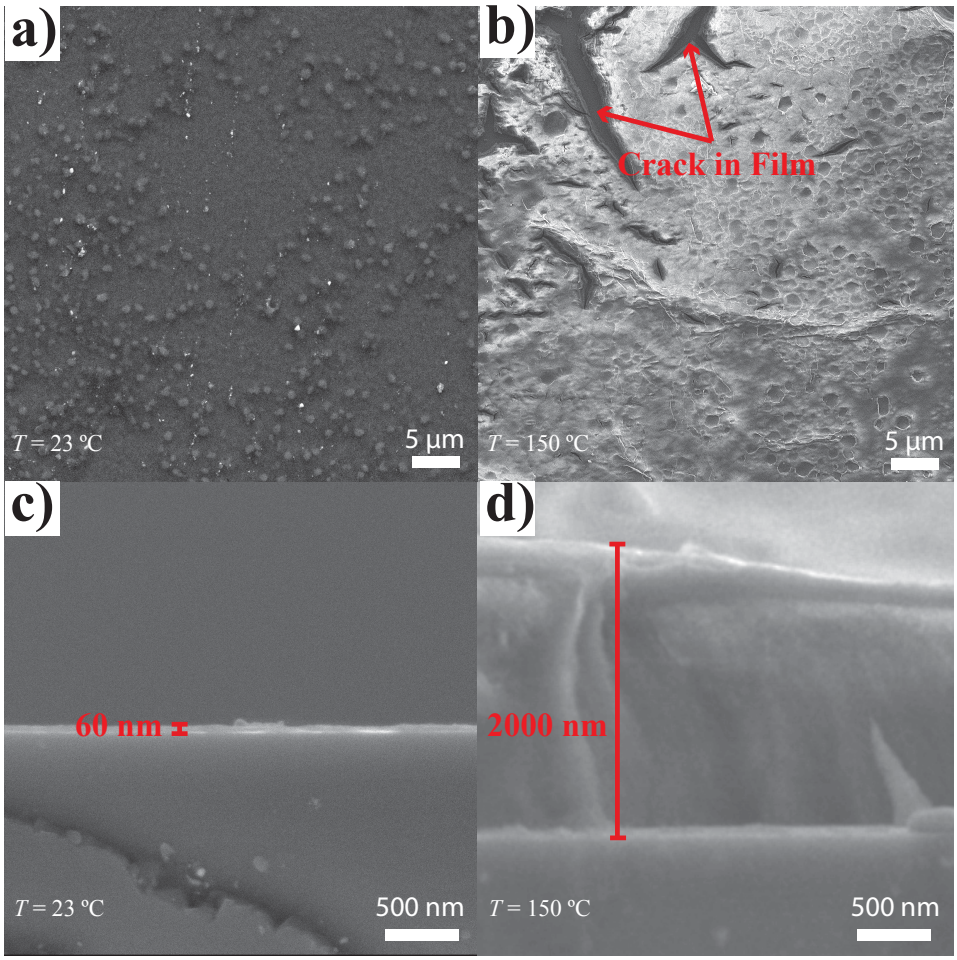


Figure 3.5 Top-down and cross section scanning electron micrographs of deposits prepared from chronoamperometry of 0.1 M $Si(NCO)_4$ in 100 mM tetrabutylammonium tetraphenylborate at -2.5 V vs *E*(Ag/AgCl) for 30 min at a,c) 23 and b,d) 150 ºC, respectively.

but the current attained a non-zero steady-state value rather than decay to zero in Cottrellian fashion. The steady-state current indicates the electroreduction of $Si(NCO)_4$ was coupled to at least one other chemical reaction rather than directly producing Si^0. To assess the emergence of stable electrogenerated and electroactive intermediates during passage of current, the data in Figure 3.4b) compares the voltammetric responses collected either after a 30 min chronoamperometry experiment at T = 150 ºC or with a newly prepared electrolyte solution on fresh n^+-Si(100) electrodes at a scan rate of 10 mV s^{-1}. No new redox peaks were observed nor was the current magnitude altered, indicating the steady-state current in the chronoamperometry was not producing appreciable quantities of new redox active species in solution.

The surface of the electrodes following experiments akin to Figure 3.4a) are shown in Figure 3.5. The top-down view scanning electron micrographs of electrode surfaces showed solid deposits following $Si(NCO)_4$ electroreduction in solutions containing 0.1 M $Si(NCO)_4$ and 0.1 M tetrabutylammonium tetraphenylborate at E = -2.5 V E(vs Ag/AgCl) for 30 min at T = 23 ºC. The deposited solids were large, coarse nuclei adjoined by a thin deposit covering the electrode surface. At T = 150 ºC, the obtained deposit was similarly coarse but was far more insulating, as evidenced by more extensive charging during imaging by electron microscopy. Figures 3.5c,d) show cross-section scanning electron micrographs of these same deposits, respectively. Each image highlights the thickness of the deposit, with the elemental analyses of the deposits from X-ray photoelectron spectroscopy presented in Table 1. At T = 23 ºC, the composition of the obtained deposit suggested a highly oxidized but Si rich film. This description is in good accord with observed compositions of electrodeposited Si films from $SiCl_4$ that readily oxidize upon exposure to air.[13, 15] At T = 150 ºC, the elemental composition was considerably less Si rich and nearly entirely composed of C and

Electrodeposition Bath Temperature (°C)	Supporting Electrolyte	Si	O	C	N	B
23	**$N(C_4H_9)_4BPh_4$**	36 ± 7%	37 ± 7%	13 ± 4%	5 ± 1%	5 ± 1%
150	**$N(C_4H_9)_4BPh_4$**	8 ± 1%	50 ± 2%	42 ± 3%	1 ± 0%	N/A

Table 3.1 Elemental composition of the electrodeposited film analyzed by X-ray Photoelectron Spectroscopy.

O species. This composition suggests the obtained deposit obtained at elevated temperature was not zero-valent Si.

Electroreduction of $Si(NCO)_4$ with a liquid metal electrode A separate set of electrodeposition experiments were performed with a liquid *e*-GaIn to assess the possibility of Si ec-LLS with $Si(NCO)_4$. Given the apparent coupled chemical reaction(s) at elevated temperatures, these experiments were performed solely at room temperature. In Si ec-LLS, liquid metal electrodes are used as both a source of electrons to reduce a Si precursor and also as a medium for dissolution and recrystallization of Si^0 (Figure 3.6a).[8, 23-24] A comparison of the voltammetric responses for liquid *e*-GaIn electrodes with and without 100 mM $Si(NCO)_4$ in 100 mM tetrabutylammonium chloride is shown in Figure 3.6b). There was a clear enhancement in the total current in the presence of $Si(NCO)_4$, indicating electroreduction was also possible with this type of electrode. The excess currents at the more positive potentials were consistent with the presence of Cl^- in the electrolyte. Figure 3.6c) shows an optical photograph of the e-GaIn pool electrode after biasing at E = -2.5 V E(vs Ag/AgCl) while immersed in solution containing 100 mM $Si(NCO)_4$ and 100 mM tetrabutylammonium tetraphenylborate for 30 min. An uneven, white film accumulated on the surface. Raman spectra were collected of these films (Figure 3.6d) following rinsing with methanol and acetone and drying by an $N_2(g)$ stream. Several peaks were observed. Peaks observed at 710 and 545 cm^{-1} are ascribed to the Si-NCO deformation stretches.[34] The Raman peak observed at 510 cm^{-1} was ascribed to the metal surface adsorption of NCO^-.[35] Several additional small peaks found between 1000-1050, 1380-1450, at 1725 cm^{-1} were assigned to organic species, with methylene, carbonate ester, and carbonyl functionalities, respectively.[36] A broad band centered around 480 cm^{-1} suggestive of amorphous Si was not observed and neither were signals at 300 cm^{-1} consistent with SiO_x.[33] Additionally, a sharp Raman phonon mode at 520

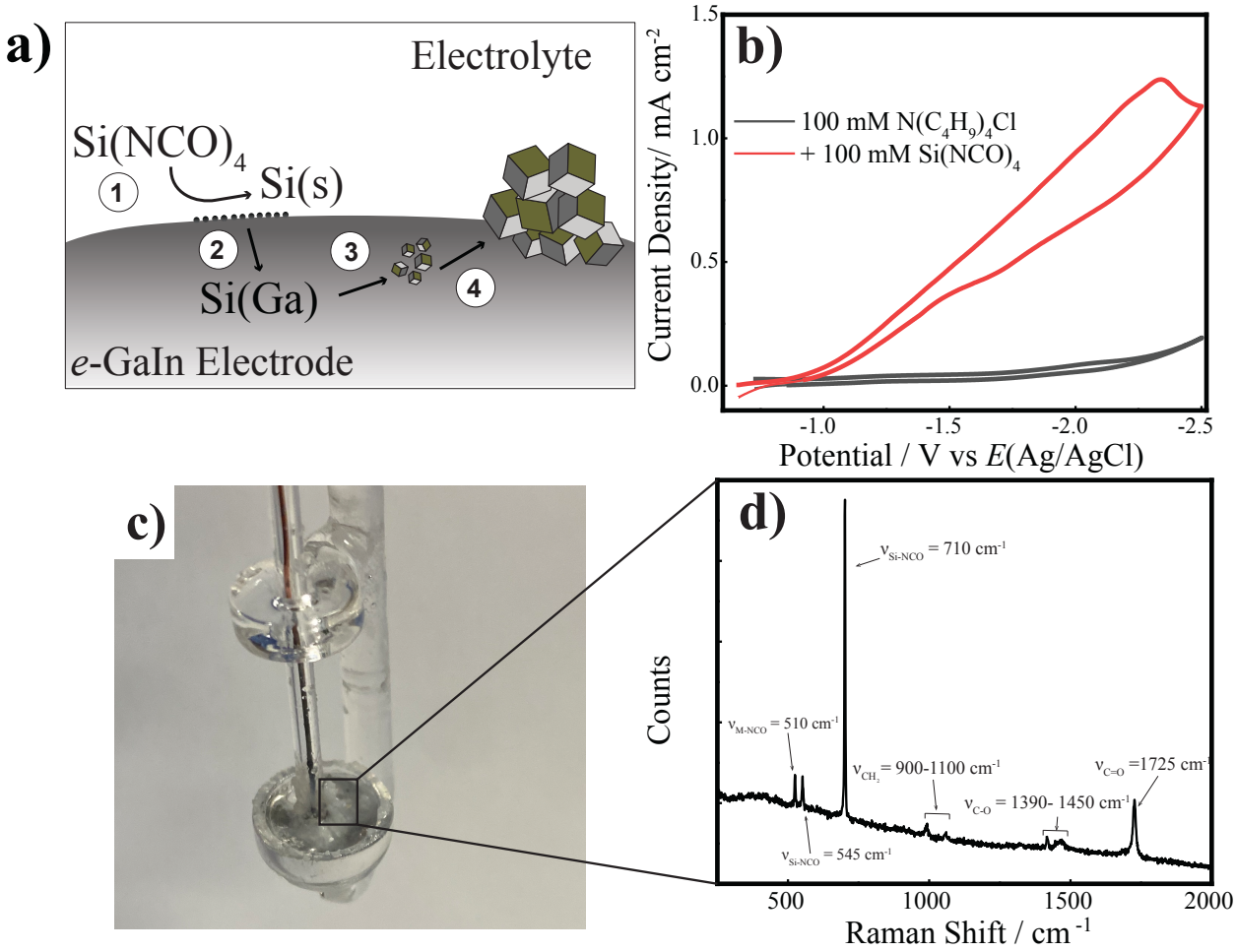


Figure 3.6 a) Schematic depiction (not drawn to scale) of an electrochemical liquid–liquid–solid (ec-LLS) process yielding crystalline Si with a liquid e-GaIn electrode. b) Cyclic voltammetry obtained from 0.1 M solutions of $Si(NCO)_4$ (solid red line) in 0.1 M tetrabutylammonium chloride (solid black line) at a eutectic gallium indium pool electrode. Scan rate = 100 mV s^{-1}. c) Photograph of an *e*-GaIn pool electrode after biasing at E = -2.5 V in propylene carbonate containing 0.1M $Si(NCO)_4$ in 0.1 M tetrabutylammonium chloride at E = -2.5 V vs E(Ag/AgCl) for 30 min at T = 23 ºC. d) Raman spectra of the collected deposit in c).

cm^{-1} diagnostic of crystalline Si was not observed. Accordingly, the electrodeposited film was most accurately described as a polymeric composite containing partially or fully reduced $Si(NCO)_4$ species and trapped electrolyte.[34, 37-40] Experiments performed with BPh_4^- electrolytes yielded equivalent results.

3.4 Discussion

The data presented here speak to three points. First, $Si(NCO)_4$ is electroactive and can be reduced. Second, the operative process in the electroreduction of $Si(NCO)_4$ is complicated and strongly depends upon the conditions of the electrolyte bath. Third, while $Si(NCO)_4$ is a potentially useful precursor for electrodeposition of amorphous Si on solid electrodes it is not suitable for Si ec-LLS with *e*-GaIn.

Electroreduction of $Si(NCO)_4$. The reductive behavior of $Si(NCO)_4$ parallels the electrochemical behavior of $SiCl_4$. First, the data are clear that this pseudohalide silane exhibits electrochemical activity at potentials comparable to $SiCl_4$. This similarity suggests the strength of the Si-X bonds are similar, in agreement with the extant literature. For instance, $Si(NCO)_4$ and $SiCl_4$ form $Si(NCO)_4^-$ and $SiCl_4^-$ in the gas phase upon electron capture of electrons with similar energies. Moreover, the sets of dissociative ion products (i.e. $Si(NCO)_3^-$, $Si(NCO)_2^-$, $Si(NCO)^-$, Si^- & NCO^- and $SiCl_3^-$, $SiCl_2^-$, $SiCl^-$, Si^- & Cl^-) were in similar relative abundances.[41]

Second, like $SiCl_4$, [17] the voltammetric responses for $Si(NCO)_4$ did not show a simple dependence with concentration. For chlorosilanes, a singular clear redox peak is only observed at concentrations greater than 5 mM.[17] The present interpretation of this behavior is the mechanism is mediated by an absorptive event which dictates the total attainable reaction rate. The invariance of current during $Si(NCO)_4$ electroreduction at low concentrations is consistent with adsorption being important. Further, the generation of $SiCl_3^-$ intermediates is important in the reduction of

$SiCl_4$.[17] If the electroreduction of $Si(NCO)_4$ similarly depends on the accumulation of a similar intermediate (e.g. $Si(NCO)_3^-$), then the concentration threshold required for a pronounced voltammetric response is reasonable.

The chronoamperometric deposition of $Si(NCO)_4$ also showed several similarities to the chlorosilanes at room temperature. For both $Si(NCO)_4$ and the chlorosilanes, the morphology of the electrodeposit at room temperature was a coarse, granular, and Si-rich film. Accordingly, the electrodeposition behavior of $Si(NCO)_4$ at room temperature is analogous to $SiCl_4$.

Still, the electroreduction of $Si(NCO)_4$ also showed clear differences from $SiCl_4$. First, the ambient chronoamperometric deposition of $Si(NCO)_4$ produced, for the first time in molecular solvents, a-Si thin films free of halides.[42] Although not of interest here, if care is taken to preserve the resultant amorphous Si, it stands to reason the character of amorphous Si produced by electroreduction of $Si(NCO)_4$ is different than the amorphous Si produced by electroreduction of $SiCl_4$. Specifically, Cl^- actively disrupts the bonding network in amorphous Si.[43] Second, under the same experimental conditions, the peak current density from the voltammetric response of $Si(NCO)_4$ observed here was 0.5 mA cm^{-2}, nearly an order of magnitude smaller than for $SiCl_4$ at otherwise identical conditions (3 mA cm^{-2}).[17] Simply, the rate of electroreduction of $Si(NCO)_4$ appears slower. Third, the high temperature electroreduction of $Si(NCO)_4$ is very different. As evident in the presented voltammetry, a second broad wave is apparent at more negative potentials that isn't visible at room temperature (e.g. Figure 3.1). We believe this specifically reflects the fact that the NCO ligand is electroactive at elevated temperatures. The product of $Si(NCO)_4$ electroreduction is not pure amorphous Si. It instead appears to be predominantly an organics-containing film.

The reactivity of $Si(NCO)_4$ at elevated temperatures is probably not demonstrative of an initial scission of the Si-NCO bond. Earborn et al. devised a conversion series for the exchange reaction between SiR_3X and M*X* salts (R = alkyl, $X = I^- \rightarrow S^- \rightarrow Br^- \rightarrow Cl^- \rightarrow NCS^- \rightarrow NCO^-$), ordering the reaction tendencies with the strength of the Si-*X* bond.[44] Since $SiCl_4$ is stable in propylene carbonate at T = 150 °C, it seems unlikely that $Si(NCO)_4$ decomposes in this same solution.

We posit instead that at elevated temperatures, the absence of Si electrodeposition during $Si(NCO)_4$ electroreduction reflects an acceleration of electropolymerization of organoisocyanates. That is, the reductive electropolymerization of organoisocyanates has been widely reported in the production of a solid electrolyte interphases for the protection of electrode materials in Li-ion battery technology.[30-31] At very negative potentials, a radical anion of the isocyanate functional group can form which goes on to either react with other isocyanate monomers or with the solvent (propylene carbonate) to generate a polymeric coating with a high carbonyl content on the substrate. Here, the activation energy for electropolymerization is surmountable at T = 150 °C, so the electroreduction of $Si(NCO)_4$ becomes coupled with this reaction. The higher oxygen content, and the features in the Raman spectra in Figure 3.6 indicative of carbonate ester groups, is consistent with this premise. Since this electropolymerization reaction is fast and difficult to suppress, the net conclusion is that $Si(NCO)_4$ can only be used to electrodeposit Si^0 efficiently at low temperatures.

Suitability of $Si(NCO)_4$ for Si ec-LLS The collected data suggest that Si ec-LLS at room temperature with $Si(NCO)_4$ is not possible with *e*-GaIn under the explored conditions. The reasons are unclear, since at room temperature apparently amorphous Si is obtained during $Si(NCO)_4$

electroreduction with solid electrodes. We believe the description of amorphous Si is appropriate even though the characterization indicates oxidized Si for the following reasons. First, the ...

We posit that the issue may arise from adsorption of electrogenerated NCO^- ligands during electrolysis. The N-bound adsorption of free isocyanate ligand under cathodic potentials is known in dilute KNCO electrolytes on gold, silver, nickel and copper electrodes.[35, 45-47] In this literature, the adsorption depended on the metal identity, tracking the Lewis acidity of the electrode.[35] In the Raman spectra shown in Figure 3.6d, the peak at 510 cm^{-1} directly implicates at least some isocyanate adsorption on Ga.[35] While in aqueous media there is an apparent redox process for NCO^-/NC^- couple, here the use of propylene carbonate rather than water, and the absence of vigorous bubbling at the electrode surface, argue against electroreduction of NCO^-. Accordingly, we propose that NCO^- is a persistent surface adsorbate that prevents adsorbed Si^0 formation.[35, 47-48] The metal N-bound isocyanate Raman mode at 510 cm^{-1} and the strong Si-NCO peak at 705 cm^{-1} in the Raman data support this point.

3.5 Conclusions

In this work, the electrochemical activity and electrodeposition characteristics of $Si(NCO)_4$ were investigated. The voltammetry presented here demonstrate for the first time that $Si(NCO)_4$ is electroactive at negative applied potentials. Under certain conditions, appreciable amounts of Si^0 can be obtained from the sustained electroreduction of $Si(NCO)_4$. Further, unlike chlorosilanes, the electrochemical behavior of $Si(NCO)_4$ was not strongly influenced by the identity of the supporting electrolyte. However, the apparent mechanism for $Si(NCO)_4$ electroreduction depended on several factors which severely limit its utility as a general Si electrodeposition precursor. Simply, competition with NCO^- electropolymerization precludes clean Si electrodeposition at elevated temperatures. Lastly, although $Si(NCO)_4$ may be useful for low

temperature electrodeposition of amorphous Si on solid Si electrodes, Si ec-LLS is not realized under conditions that are suitable for $SiCl_4$. More work is needed to understand if there are other experimental conditions (e.g. other liquid metals, intermediate electrolyte temperature, more nuanced applied waveforms) that do allow Si ec-LLS with $Si(NCO)_4$.

3.6 References

1. Elwell, D.; Feigelson, R. S., "Electrodeposition of solar silicon." *Solar Energy Materials* **1982,** *6* (2), 123-145.
2. Agrawal, A. K.; Austin, A. E., "Electrodeposition of Silicon from Solutions of Silicon Halides in Aprotic Solvents." *Journal of The Electrochemical Society* **1981,** *128* (11), 2292-2296.
3. Rama Mohan, T. R.; Kröger, F. A., "Cathodic deposition of amorphous silicon from solutions of silicic acid and tetraethyl ortho-silicate in ethylene glycol and formamide containing HF." *Electrochimica Acta* **1982,** *27* (3), 371-377.
4. Takeda, Y.; Kanno, R.; Yamamoto, O.; Rama Mohan, T. R.; Lee, C. H.; Kröger, F. A., "Cathodic Deposition of Amorphous Silicon from Tetraethylorthosilicate in Organic Solvents." *Journal of The Electrochemical Society* **1981,** *128* (6), 1221-1224.
5. Elwell, D., "Electrocrystallization of semiconducting materials from molten salt and organic solutions." *Journal of Crystal Growth* **1981,** *52*, 741-752.
6. Boen, R.; Bouteillon, J., "The electrodeposition of silicon in fluoride melts." *Journal of Applied Electrochemistry* **1983,** *13* (3), 277-288.
7. Rao, G. M.; Elwell, D.; Feigelson, R. S., "Electrowinning of Silicon from K 2SiF6 - Molten Fluoride Systems." *Journal of The Electrochemical Society* **1980,** *127* (9), 1940-1944.
8. Ma, L.; Lee, S.; DeMuth, J.; Maldonado, S., "Direct electrochemical deposition of crystalline silicon nanowires at T ≥ 60 °C." *RSC Advances* **2016,** *6* (82), 78818-78825.
9. Link, S.; Ivanov, S.; Dimitrova, A.; Krischok, S.; Bund, A., "Electrochemical deposition of silicon from a sulfolane-based electrolyte: Effect of applied potential." *Electrochemistry Communications* **2019,** *103*, 7-11.
10. Nishimura, Y.; Fukunaka, Y., "Electrochemical reduction of silicon chloride in a non-aqueous solvent." *Electrochimica Acta* **2007,** *53* (1), 111-116.
11. Bechelany, M.; Elias, J.; Brodard, P.; Michler, J.; Philippe, L., "Electrodeposition of amorphous silicon in non-oxygenated organic solvent." *Thin Solid Films* **2012,** *520* (6), 1895-1901.
12. Zein El Abedin, S.; Borissenko, N.; Endres, F., "Electrodeposition of nanoscale silicon in a room temperature ionic liquid." *Electrochemistry Communications* **2004,** *6* (5), 510-514.
13. Munisamy, T.; Bard, A. J., "Electrodeposition of Si from organic solvents and studies related to initial stages of Si growth." *Electrochimica Acta* **2010,** *55* (11), 3797-3803.
14. Gobet, J.; Tannenberger, H., "Electrodeposition of Silicon from a Nonaqueous Solvent." *Journal of The Electrochemical Society* **1988,** *135* (1), 109-112.
15. Nicholson, J. P., "Electrodeposition of Silicon from Nonaqueous Solvents." *Journal of The Electrochemical Society* **2005,** *152* (12), C795-C802.

16. Rao, G. M.; Elwell, D.; Feigelson, R. S., "Electrodeposition of Silicon onto Graphite." *Journal of The Electrochemical Society* **1981,** *128* (8), 1708-1711.
17. Downes, N.; Cheek, Q.; Maldonado, S., "Electroreduction of Perchlorinated Silanes for Si Electrodeposition." *Journal of The Electrochemical Society* **2021,** *168* (2), 022503.
18. Shah, N. K.; Pati, R. K.; Ray, A.; Mukhopadhyay, I., "Electrodeposition of Si from an Ionic Liquid Bath at Room Temperature in the Presence of Water." *Langmuir* **2017,** *33* (7), 1599-1604.
19. Borisenko, N.; Zein El Abedin, S.; Endres, F., "In Situ STM Investigation of Gold Reconstruction and of Silicon Electrodeposition on Au(111) in the Room Temperature Ionic Liquid 1-Butyl-1-methylpyrrolidinium Bis(trifluoromethylsulfonyl)imide." *The Journal of Physical Chemistry B* **2006,** *110* (12), 6250-6256.
20. Pulletikurthi, G.; Lahiri, A.; Carstens, T.; Borisenko, N.; Zein El Abedin, S.; Endres, F., "Electrodeposition of silicon from three different ionic liquids: possible influence of the anion on the deposition process." *Journal of Solid State Electrochemistry* **2013,** *17* (11), 2823-2832.
21. Prat, O. P.; Cloitre, T.; Aulombard, R. L., "Thermal and Mechanical Properties of Silicon Tetrachloride (SiCl4) and Germanium Tetrachloride (GeCl4) in Their Vapor and Liquid Phases." *Chemical Vapor Deposition* **2007,** *13* (5), 199-203.
22. Jenkins, A. C.; Chambers, G. F., "Vapor Pressures of Silicon Compounds." *Industrial & Engineering Chemistry* **1954,** *46* (11), 2367-2369.
23. Gu, J.; Fahrenkrug, E.; Maldonado, S., "Direct Electrodeposition of Crystalline Silicon at Low Temperatures." *Journal of the American Chemical Society* **2013,** *135* (5), 1684-1687.
24. Fahrenkrug, E.; Maldonado, S., "Electrochemical Liquid–Liquid–Solid (ec-LLS) Crystal Growth: A Low-Temperature Strategy for Covalent Semiconductor Crystal Growth." *Accounts of Chemical Research* **2015,** *48* (7), 1881-1890.
25. Machida, H.; Kada, T.; Ishikawa, M.; Ogura, A.; Ohshita, Y., "Vapor Pressure of Hf and Si Precursors for HfxSi1-xO2Deposition Evaluated by a Saturated Gas Technique." *Japanese Journal of Applied Physics* **2004,** *43* (3), 966-967.
26. Forbes, G. S.; Anderson, H. H., "Cyanates of Silicon, Phosphorus and Boron. Instability of Certain Ternary Boron Compounds." *Journal of the American Chemical Society* **1940,** *62* (4), 761-763.
27. Idris, I.; Sugiura, O., "Hydrogen-Free Plasma-Enhanced Chemical Vapor Deposition of Silicon Dioxide Using Tetra-isocyanate-silane (Si(NCO)$_{\bf 4}$)." *Japanese Journal of Applied Physics* **1995,** *34* (Part 2, No. 6B), L772-L774.
28. Teichmann, J.; Bursch, M.; Köstler, B.; Bolte, M.; Lerner, H.-W.; Grimme, S.; Wagner, M., "Trapping Experiments on a Trichlorosilanide Anion: a Key Intermediate of Halogenosilane Chemistry." *Inorganic Chemistry* **2017,** *56* (15), 8683-8688.
29. Tillmann, J.; Meyer, L.; Schweizer, J. I.; Bolte, M.; Lerner, H.-W.; Wagner, M.; Holthausen, M. C., "Chloride-Induced Aufbau of Perchlorinated Cyclohexasilanes from Si2Cl6: A Mechanistic Scenario." *Chemistry – A European Journal* **2014,** *20* (30), 9234-9239.
30. Lipatova, E. E.; Matyushova, V. G.; Narazhaiko, L. F., "Electrochemical polymerization of an unsaturated isocyanate on the surface of carbon fibres." *Polymer Science U.S.S.R.* **1986,** *28* (10), 2267-2275.
31. Korepp, C.; Kern, W.; Lanzer, E. A.; Raimann, P. R.; Besenhard, J. O.; Yang, M. H.; Möller, K. C.; Shieh, D. T.; Winter, M., "Isocyanate compounds as electrolyte additives for lithium-ion batteries." *Journal of Power Sources* **2007,** *174* (2), 387-393.

32. Eaborn, C., "601. Organosilicon compounds. Part II. A “conversion series” for organosilicon halides, pseudohalides, and sulphides." *Journal of the Chemical Society (Resumed)* **1950,** (0), 3077-3089.
33. Gunawardena, G.; Hills, G.; Montenegro, I.; Scharifker, B., "Electrochemical nucleation: part I. general considerations." *Journal of Electroanalytical Chemistry and Interfacial Electrochemistry* **1982,** *138* (2), 225-239.
34. Miller, F. A.; Carlson, G. L., "The vibrational spectra and structure of Si(NCO)4 and Ge(NCO)4." *Spectrochimica Acta* **1961,** *17* (9), 977-989.
35. Bron, M.; Holze, R., "Cyanate and thiocyanate adsorption at copper and gold electrodes as probed by in situ infrared and surface-enhanced Raman spectroscopy." *Journal of Electroanalytical Chemistry* **1995,** *385* (1), 105-113.
36. Colthup, N., *Introduction to infrared and Raman spectroscopy*. Elsevier: 2012.
37. Schmitt, M., "Analysis of silanes and of siloxanes formation by Raman spectroscopy." *RSC Advances* **2014,** *4* (4), 1907-1917.
38. Creighton, J. A.; Withnall, R., "The Raman spectrum of gallium metal." *Chemical Physics Letters* **2000,** *326* (3), 311-313.
39. Koster, D. F., "The vibrational spectra and structure of Cl3SiNCO, Cl3SiNCS, ClSi(NCO)3 and (CH3)3CNCO." *Spectrochimica Acta Part A: Molecular Spectroscopy* **1968,** *24* (4), 395-405.
40. Brown, F. B.; Fletcher, W. H., "The vibrational spectrum of dimethyl cyanamide." *Spectrochimica Acta* **1963,** *19* (6), 915-923.
41. Wilkerson, B. E.; Dillard, J. G., "Resonant electron capture in silicon tetraisocyanate and silicon tetrachloride." *Journal of the Chemical Society D: Chemical Communications* **1969,** (5), 212a-212a.
42. Capezzuto, P.; Bruno, G., "Plasma deposition of amorphous silicon films: an overview on some open questions." *Pure and Applied Chemistry* **1988,** *60* (5), 633-644.
43. Park, Y.-B.; Rhee, S.-W., "Microstructure and interfacial states of silicon dioxide film grown by low temperature remote plasma enhanced chemical vapor deposition." *Journal of Applied Physics* **1999,** *86* (3), 1346-1354.
44. Eaborn, C., "A Conversion Series for Organosilicon Halides, Pseudohalides and Sulphides." *Nature* **1950,** *165* (4200), 685-686.
45. Cheuquepán, W.; Orts, J. M.; Rodes, A.; Feliu, J. M., "DFT and spectroelectrochemical study of cyanate adsorption on gold single crystal electrodes in neutral medium." *Journal of Electroanalytical Chemistry* **2017,** *793*, 147-156.
46. Cheuquepán, W.; Rodes, A.; Orts, J. M., "Cyanate and Cyanurate Adsorption at Silver Electrodes in Neutral Solutions: In Situ ATR-SEIRAS and DFT Studies." *The Journal of Physical Chemistry C* **2020,** *124* (1), 709-721.
47. Corrigan, D. S.; Weaver, M. J., "Adsorption and oxidation of benzoic acid, benzoate, and cyanate at gold and platinum electrodes as probed by potential-difference infrared spectroscopy." *Langmuir* **1988,** *4* (3), 599-606.
48. Corrigan, D. S.; Weaver, M. J., "Coverage-dependent orientation of adsorbates as probed by potential-difference infrared spectroscopy: azide, cyanate, and thiocyanate at silver electrodes." *The Journal of Physical Chemistry* **1986,** *90* (21), 5300-5306.

Chapter 4

Electrodeposition of Epitaxial Si Films at Ambient Pressure and Temperature by Electrochemical Liquid Phase Epitaxy

4.1 Introduction

In 2020, the gap between the global energy consumption and solar energy production was 18 TW.[1-2] Among all candidate materials, Si is ideal material for mass production given its natural abundance, exhaustively understood metallurgy, non-toxicity, long lifecycle, and ubiquity in modern device architecture.[3-4] However, the conversion of Si found in nature (silica/quartz) to pure crystalline Si used in devices is still largely performed using mass scale carbothermic reduction.[5] Ultimately, both the environmental toll and economic instability of markets depending on this method will preclude a rapid expansion of crystalline Si production. To this end, bridging the enormous energy gap in an environmentally benign and fiscally sound manner, in the near-term, would be greatly accelerated by the devise of new methods for making crystalline Si.

Historically, electrodeposition has been identified as a potential alternative route for the preparation of Si, since electrodeposition can be inherently technologically simple, clean, and comparatively non-energy-intensive.[6-8] However, carbothermic reduction is still favored for two reasons. First, while the electrodeposition of Si from molecular solvents can be performed, owing to the insolubility of Si^0 and the strength of the Si-Si bond compared to the available thermal

energy, the resultant deposit is amorphous.[6, 9-18] Second, while significant advances have been made in the direct electroreductive deoxygenation of SiO_2 to form polycrystalline Si, these methods depend on high temperature ($T > 650$ºC) to liquefy the eutectic salt electrolyte in which SiO_2 is soluble .[6-7, 13, 19-23] Recently, a separate tactic has been devised, denoted electrochemical liquid-liquid-solid (ec-LLS), that uses liquid metal electrodes which act as both sources of electrons to reduce dissolved precursors and as a medium for recrystallization of dissolved zero valent metal. This method has been applied for the growth of III-V and group IV bulk crystals, nano- and microwires, and by a unique adaption denoted electrochemical liquid-phase epitaxy (ec-LPE) shown schematically in Figure 4.1, for macroscopically large epitaxial thin films.[24-28]

Herein, we described the effects of applied waveform on the electrodeposition of epitaxial Si thin films by ec-LPE. We present, for the first time, a direct electrochemical method for the growth of thick epitaxial Si thin films at ambient temperatures and pressures. There were three hypothesis explored. First, $SiCl_4$ can be used in ec-LPE to grow epitaxial Si at a *e*-GaIn electrode thin film. Second, that the introduction of a duty cycle into the electrodeposition of $SiCl_4$ enables the growth of thick epitaxial Si thin films. Third, by the application of a duty cycle in ec-LPE, the electrochemical growth of epitaxial Si thin films can be performed at temperatures as low as the ambient. Electrochemical, electron microscopy, Raman spectroscopy, electron and x-ray diffraction data are presented here exploring these hypotheses.

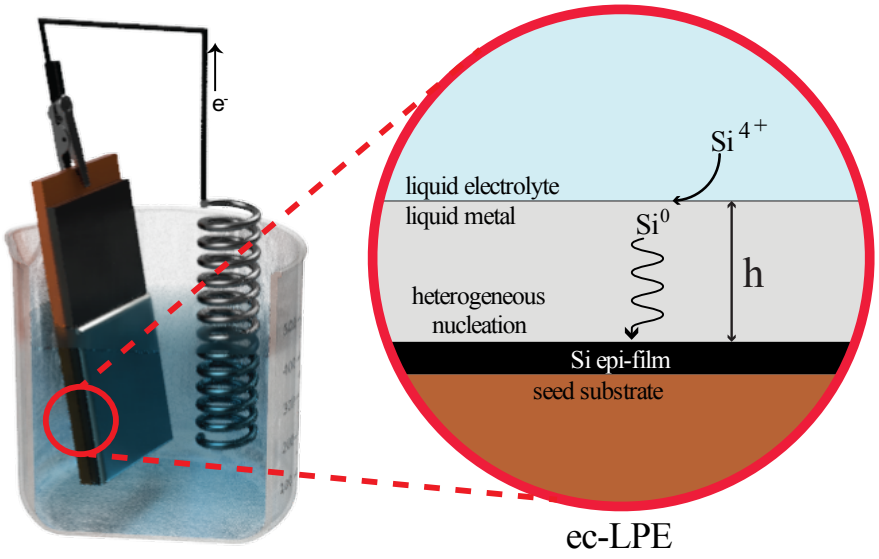


Figure 4.1 Overview of an electrochemical liquid phase epitaxy (ec-LPE) film growth concept with a thin liquid metal electrode with thickness *h*. Schematic depiction of the relevant steps in Si ec-LPE, where an oxidized species Si^{4+} species dissolved in the liquid electrolyte reduces to Si^0 by heterogeneous electron transfer, partitions into the liquid metal film, and then diffuses some distance away from the liquid electrolyte/liquid metal interface before undergoing heterogeneous nucleation at the crystal seed substrate.

4.2 Experimental

$SiCl_4$ (99.99+%, Gelest), HF (49%, Transene Inc.), gallium (99.999%, Alfa Aesar), indium (99.999%, American Elements), SU-8-2007 (MicroChem Corp.), SU-8 developer (MicroChem Corp.), copper pellets (99.999%, R.D. Mathis and Company), hexamethyldisilazane (HMDS, Fischer Scientific), hexanes (ACS Grade, Fischer Scientific), methanol (ACS grade, BDH), acetone (ACS grade, BDH), imidazole (99%, Sigma Aldrich), tertbutyldimethylchlorosilane (99%, Oakwood Chemicals), anhydrous THF (99.5%, Sigma Aldrich, extra dry over molecular sieves) were used as received. Propylene carbonate (99.5%, Acros Organics), tetrabutylammonium chloride (95%, Alfa Aesar) were purified according to our previously reported method. Water with a resistivity >18.2 MΩ cm (Barnsted Nanopure) was used throughout.

Degenerately doped, n-type Si(111) (<0.006 Ω·cm, 0.525 ± 0.015 mm thick, Wafer Works Corp.) and n-type Si(100) wafers (< 0.007 Ω·cm, 0.625 ± 0.020 mm thick, Crysteco) were diced into 4 x 8 cm sections and degreased in water, acetone, hexanes, and methanol under sonication followed by plasma etch (model PE-50, Plasma Etch Inc.) of the substrates in O_2 (20 sccm, 400 W) to clean the unremoved advantageous carbon. The removal of native oxide in 5% HF for 1 min was done to expose a clean Si surface before continuing to the next step. A thin copper film was deposited by thermal evaporation to a thickness of ~ 20 nm of Cu prior to photolithography. Before use in ec-LPE experiments, the wafers were subjected to lithographic patterning as previously described.[25] Directly before use in ec-LPE experiments, exposed copper was immersed in acetic acid to remove residual CuO_x species for 1 min and dried with an N_2 stream prior to being wetted with *e*-GaIn.

Cell Assembly To form a contiguous liquid e-GaIn film with 10 μm thickness, liquid e-

GaIn was pipetted onto a given patterned wafer section which rested on a flat conductive plate set into the solid bottom plate. The liquid metal was spread evenly using a lint-free cloth so that the height in the main cavity was slightly above the photoresist layer. The ports on the membrane were optically aligned with the channels on the substrate and then the membrane was placed on top of the wafer section. The clamping plate was then used to secure this stack with compression under tension by six steel screws. To ensure complete filling of the thin cavity with liquid metal, the exit port was then closed off and the liquid metal was kept under pressure with the syringe at a nominal pressure of 700 psi. The reservoir for the liquid electrolyte was then separately press fit onto the opening in the top clamping plate, with a Kalrez O-ring between the bottom edge of the electrolyte cell and the top-side of the porous membrane. This stack, under compression and fully assembled, was then transferred into an N_2-purged glove box. A schematic description of the cell components and the cell after assembly are shown in Figure 4.2. Electrical contact to the ec-LPE substrate was made through a clip affixed to one of the screws.

Electrochemical measurements.—A Metrohm Autolab PGSTAT302N was employed for all electrochemical measurements and electrodeposition experiments. All electrochemical measurements were performed in a MBraun MB10 drybox. A standard three-electrode configuration with a carbon rod counter electrode with *e*-GaIn as as the working electrode and a reference electrode consisting of a Ag wire coated with AgCl immersed in a fritted compartment containing 0.1 M tetrabutylammonium chloride in propylene carbonate. All reported electrochemical potentials are with respect to this electrode, which was externally referenced to ferrocene/ferrocenium periodically in a separate cell to ensure reference electrode stability. To combat the possibility of hydrolysis of $SiCl_4$ with exposed hydroxyl groups in glass cells, a

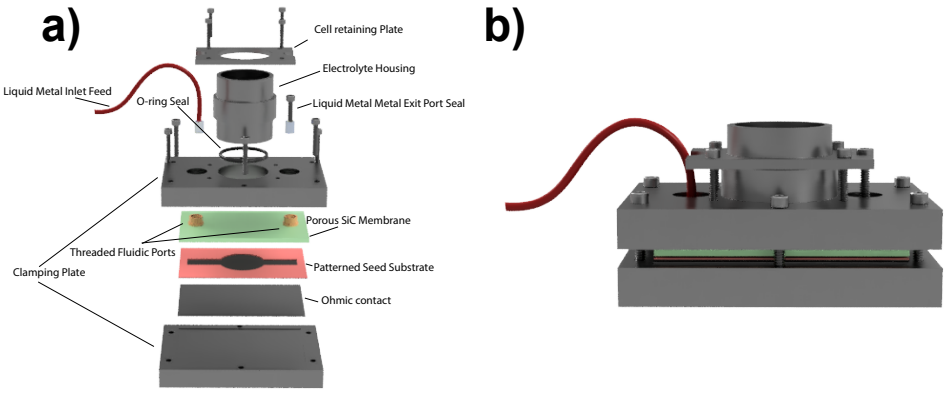


Figure 4.2 (a) Exploded view of the ec-LPE cell used in this work. Using photoresist patterned seed substrates and porous SiC membranes, large two-dimensional liquid metal thin films are formed in this cell using a compression stack. Following assembly, liquid metal is flowed in to a final thickness defined by the photoresist and liquid electrolyte is exposed to the liquid metal surface by a porous membrane that is permeable to electrolyte but resists intrusion by the liquid metal. (b) Representative view of an assembled ec-LPE cell.

silane protection method, which we've previously described, was employed.[29] Here, all experiments use a 10 mL solution of 0.5 M $SiCl_4$ and 0.1 M tetrabutylammonium chloride that were made and added into the cell directly before use. Electrodepositions were performed under potentiostatic control, with E = −1.6 V vs E(Ag/ AgCl) when direct electrodepositions were performed, and [E_1 = -1.6 V for 0.2 ms, E_2 = -0.77 V for 10 ms] when pulsed electrodepositions were performed. Following deposition, the substrate was separated from the assesmbly, immersed in acetone to remove the photoresist and then immersed in conc. HCl at room temperature to remove excess liquid e-GaIn.

Powder X-ray diffractograms and high resolution open detector symmetric coupled scans (ω-2θ) were collected with a Rigaku Smartlab X-ray diffractometer using a Cu Kα X-ray source (λ = 1.5406 Å) and Ge(2x220) incident beam monochromator and a 10 mm slit inserted before the detector. . Raman spectra were obtained using a Renishaw Raman microscope spectrometer equipped with a Nikon LU Plan 20x objective (NA = 0.4) and edge filters to reject the 785 nm excitation line. A 785 nm diode laser was used as the incident excitation at a total radiant power of 1.12 mW over a 20 μm^2 incident spot for an integration time of 60 s.

Scanning electron micrographs (SEM), electron backscatter diffraction patterns (EBSD), and energy dispersive spectra (EDS) were collected using a JEOL-7800FLV scanning electron microscope equipped with an Oxford X-Max^N silicon drift detector (Oxford Instruments) and a (Oxford NordlysMax^2) detector. Collected EDS and EBSD spectra were fitted using Oxford Aztec v3.3 EDS and AztecHKL acquisition and processing software, respectively. Focused ion beam (FIB) milling were conducted in FEI NOVA Nanolab Dualbeam and FEI Helios Nanolab 650 Dualbeam workstations, both equipped with Schottky field emitters and Ga and He focused ion

beams, respectively.

Sample preparation for transmission electron microscopy (TEM) was prepared by FIB milling and liftout using the following procedure. First, a protective Pt layer was deposited using electron beam assisted chemical vapor deposition and followed by deposition of a thicker Pt-layer (1- 2 μm) using an ion beam assisted chemical vapor deposition (IBA-CVD) employing trimethyl(methylcyclopentadienyl)platinum(IV) gas as the Pt source. Trenches were then milled into the film and substrate. An Omniprobe AutoProbe 200 micromanipulator equipped with a standard tungsten probe tip (Ted Pella) was used to Pt-weld to the thin section to the probe tip using IBA-CVD. The specimen was then cut free from the surrounding film through additional FIB milling and affixed onto a Mo- or Cu-TEM grid for analysis. High resolution TEM, scanning transmission electron microscopic (STEM) imaging and annular dark field STEM imaging were collected with a Thermofisher Talos F200x G2 operated at 200 kV.

4.3 Results

Preliminary efforts for the application of ec-LPE to Si epifilm growth are shown in Figure 4.3. Figure 4.3a. shows a representative voltammetric response of a 0.1 M tetrabutylammonium chloride in propylene carbonate solution (black) without and (red) with 0.5 M $SiCl_4$ at a compressed ec-LPE cell with *e*GaIn thin film electrode at 125 ºC. At potentials negative of -0.78 V when $SiCl_4$ is added to the electrolyte the current is prescriptive of the $4e^-$ reduction of $SiCl_4$ to Si^0. The chronoamperometric response of a 500 mM $SiCl_4$ in 0.1 M $N(C_4H_9)_4Cl$ at 125 ºC at E = -2.5 V vs E(Ag/AgCl) for 1200s without and with solution refreshment every 300s are shown in Figure 4.3b) and 3c), respectively. Following the application of a bias, the current reaches a maximum and steadily decrease to zero after ~700s. Given the disparity of the experimental

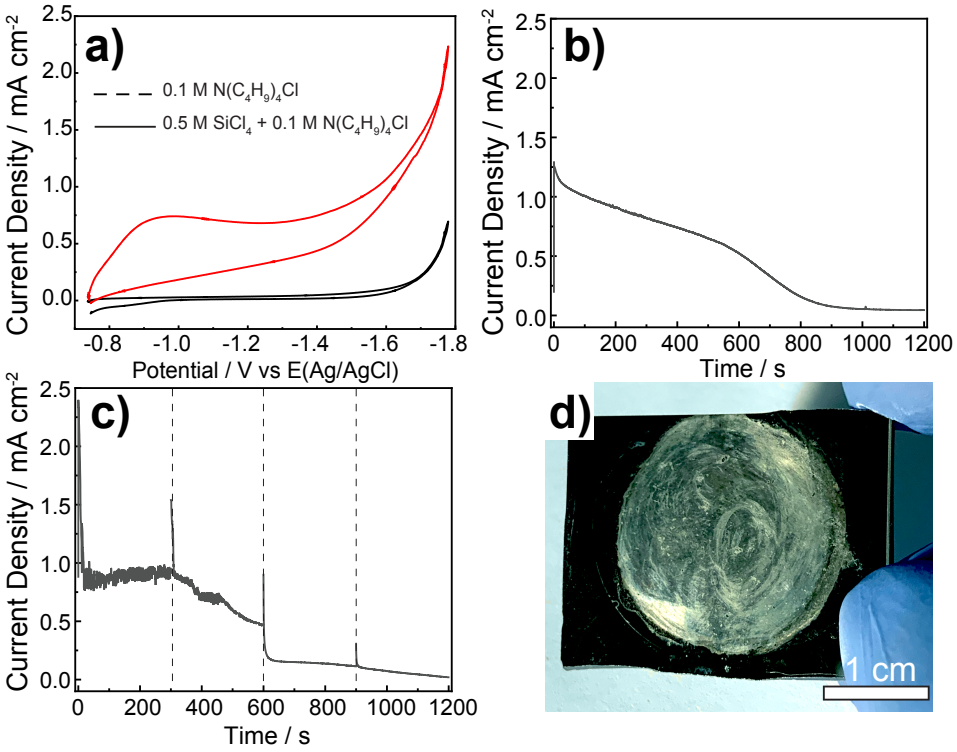


Figure 4.3 Voltammetric response of a *e*GaIn liquid metal thin film with the ec-LPE cell shown in Figure 4.2, with an electrolyte containing 0.1 M $(C_4H_9)_4NCl$ in propylene carbonate without (black) and with (red) 0.5 M $SiCl_4$ at T = 125 °C and scan rate = 0.1 V s^{-1}. b-d) Representative chronoamperometric traces of an ec-LPE deposition of a Si film using the follow conditions: T = 125 °C, and an electrolyte containing 0.5 M $SiCl_4$ and 0.1 M $(C_4H_9)_4NCl$ in propylene carbonate on an n^+-Si(100) seed substrate via b) direct electrodeposition at E = −1.6 V vs E(Ag/AgCl), c) direct electrodeposition at E = −1.6 V vs E(Ag/AgCl) refreshing the electrolyte bath every 300 s. d) Macroscopic image of deposit obtained on the n^+-Si(100) electrode after electrolysis and subsequent liquid metal removal.

temperature of 125 ºC and the boiling point of $SiCl_4$ at 56 ºC under 1 atm pressure, the hypothesis that the current decay resulted from evaporative loss was tested by replacement of the electrolyte solution after 300s. The chronoamperometric response of $SiCl_4$ in showed an identical response in which no current was regained following electrolyte refreshment is shown in Figure 4c). The total charge passed under each curve is roughly 0.55 C. Assuming that the faradaic efficiency of the $SiCl_4$ reduction is 100% and the resultant deposit exclusively results in the formation of c-Si by ec-LLS, the expected film height should be roughly 4 μm. Upon completion of the ec-LPE experiment, the cell was disassembled. The substrate was removed of photoresist by immersion in acetone and the liquid *e*-GaIn electrode was removed via immersion in concentrated HCl. A representative macroscopic photograph of the resultant deposit is shown in Figure 4.3d). A hard, strongly attached film was found beneath the same area which allowed for permeation and exposure of the electrolyte to the underlying *e*-GaIn electrode during the ec-LPE experiment. Though any variation of the area of liquid metal exposed to electrolyte resulted in a corresponding equivalent change in the dimensions of the deposit, all experiments reported here used an exposed area of approximately 4.85 cm^2.

Figure 4.4 cumulatively shows data descriptive of the morphology and material structure of the deposit obtained by Si ec-LPE by single potential step chronoamperometry. Figure 4.4a) and 4b) show scanning electron micrographs of an ec-LPE experiment that was stopped shortly after potential step to E = -1.6 V to prevent contiguous film growth. In both images, the deposit morphology depended on the structure of the underlying substrate, in which Figure 4.4a) corresponds to an n^+-Si(100) electrode and Figure 4.4b) n^+-Si(111) substrates. The square prisms shown in Figure 4.4a) are consistent with the expected [111] plane bounded structure of epitaxial Si nuclei on Si(100) owing to the slow growth rate of along the [100] plane. Similarly, the three-

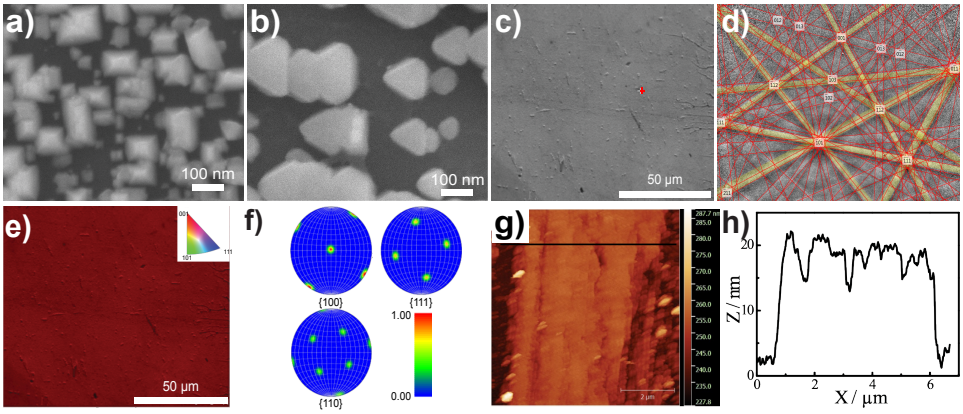


Figure 4.4 a,b) Top-down scanning electron micrographs of initial Si deposits in ec-LPE depositions performed with the same conditions as in Figure 4.1) with n^+-Si(100) and n^+-Si(111) seed substrates, respectively. c) Top-down view scanning electron micrograph of the deposit shown in Figure 4.3d). d) Diamond cubic indexed Kikuchi bands collected from the red cross-hair shown in c). e) Color-coded electron back scatter diffraction (EBSD) map of Si ec-LPE sample grown at T = 125 °C. (f) Contour pole figures from the EBSD mapping shown along the 110 and 111 poles. g) Atomic-force micrograph of Si thin film on Si substrate. (h) Line profile of the height of the Si thin film shown in (g).

fold symmetric trigonal deposits observed in 4b) are consistent with the expected epitaxial nuclei on a Si(111) surface. Figure 4.4c) represents top-down scanning electron micrograph of the deposit shown in Figure 4.3d). After depositions for 1200s a contiguous, coalesced deposit was observed over the whole electrode surface.

To probe the crystalline orientation of the film, electron backscatter diffraction patterns were collected, as shown in Figure 4.4d-f). The Kikuchi bands emerging from the red inset shown in Figure 4.4c) are shown in Figure 4.4d). These Kikuchi bands were overlaid with a simulated diffraction pattern of the diamond cubic silicon structure in the (100) orientation, therein demonstrating both a crystalline and an epitaxial nature to the film. Figure 4.4e) shows a false colored image of 4c) to denote the orientation of the film normal to the film surface by summation of 750 individual EBSD patterns collected over the entire area probed. In this image the only orientation observed corresponded to the (100) orientation of Si, based on the crystallographic data shown in Figure 4.4d). The poles figures shown in Figure 4.4f) represent the summation of the EBSD data collected in Figure 4.4e) and show only sharp poles with no rings or satellite peaks, indicating that the film was in total registry with the underlying substrate over the entire area surveyed. Figure 4.4g and 4h) represent atomic force microscopy maps of a typical deposit obtained from the Si ec-LPE experiment described in Figure 4.3). The roughness of the film, in conjunction with the growth of large 3 dimensional nuclei, supports the notion that the film follows the Volmer-Weber growth mode. Generally, under these conditions the as-grown film was limited in thickness within a maximum of 200 nanometers, far below the 4 μm thickness estimated from the amount of charge passed.

To probe the interfacial order and local microstructure of the deposit, cross-section transmission microscopy data of a Si film grown on an n^+-Si(100) substrate are shown in Figure

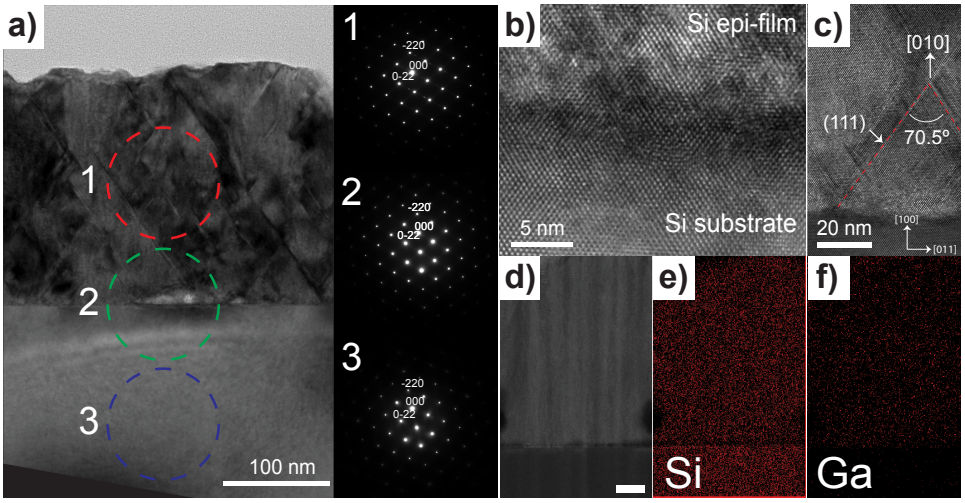


Figure 4.5. a) Bright field transmission electron micrograph of a cross section of an epitaxial Si film prepared by ec-LPE on a n^+-Si(100) at 125ºC. The red, green, and blue dashed circles correspond to the position of the selected area aperture in **1-3.** Shown in **1-3** are partially indexed selected area electron diffraction (SAED) patterns from the epifilm, the epifilm-substrate interface, and the substrate respectively. b) High magnification scanning transmission electron micrograph of a cross section of the Si epifilm shown in a). c) Representative high-resolution transmission electron micrograph of the interface between the Si film and Si substrate shown in a). (d) STEM-EDS mapping of the Si epifilm shown in a) with elemental maps of Si, Ga shown in in e) and f), respectively. Pixel intensities were normalized by the full-area integrated EDS spectra. Scale bar represents 50 nm.

4.5. Figure 4.5a) demonstrates a low magnification bright field transmission electron micrograph of the cross-sectioned film. The film was continuous across the interface and was without voids. Selected area electron diffraction patterns were collected from the (1) the film, (2) the substrate/film interface, and (3) the substrate. In all cases, the resulting observed patterns separately confirmed the crystalline structure of the deposit and that the film was in the same crystallographic structure and orientation as the substrate. Notably, satellite peaks were observed in the diffraction pattern from the epifilm corresponding to twinning planes that emerge during crystal growth. Figure 4.5b) shows a high magnification TEM-HAADF image of the film/substrate interface demonstrating the continuity of the structure across the film/substrate interface. Figure 4.5c) shows a low magnification STEM image of a line defect that emerge at the film/substrate interface and terminate in the body of the film. The angle between the 2D line defect normal to the substrate surface was approximately 70.5º angle demonstrating the defect to be a twinned plane which occured along the (111) planes of the growing nuclei.[30-31] The elemental composition of the film was probed by STEM-EDS, as shown in Figure 4.5d-f). The film was shown to be Si throughout and had a Ga concentration of 11-13 at % which was evenly distributed throughout the film (e.g. not present in precipitates or clusters), with no detectable quantity of In.

To assess the crystalline quality of a Si(100) grown epifilm made by Si ec-LPE, x-ray diffractometry data are presented in Figure 4.6a). The inset demonstrates an X-ray diffractogram which shows only a single peak at the (400) reflection of Si, and not the full set of (111), (220), and (311) peaks expected for a polycrystalline Si thin film.[32] Symmetric double axis coupled scans collected from the epifilm demonstrate the emergence of a peak centered at 34.29 º consistent with previous observations for Ga doped Si.[33] The position of this peak is consistent with the anticipated (400) diffraction peak displacement for a substitutionally hyper-doped Si thin film with gallium.[34]

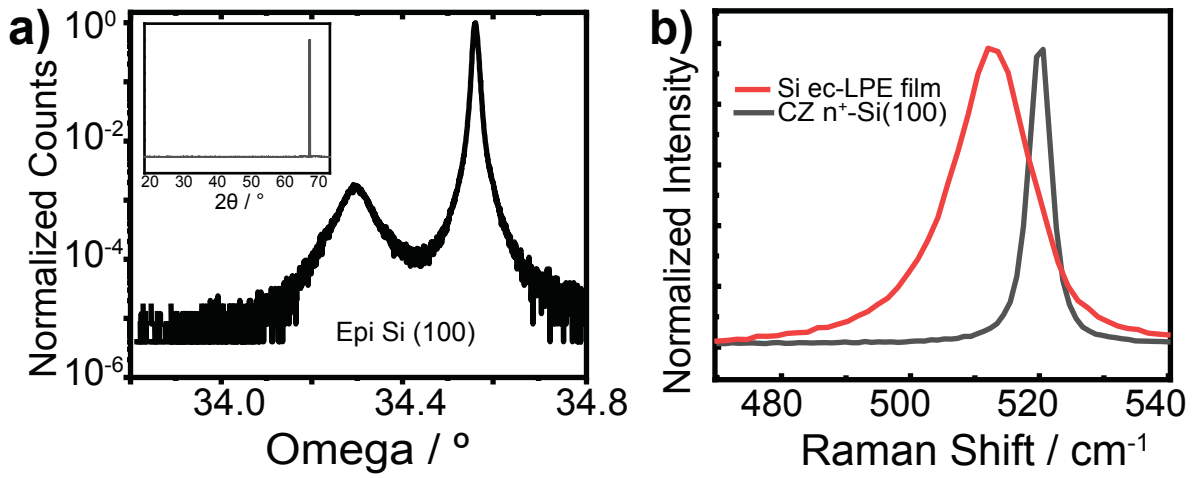


Figure 4.6. a) Representative coupled 2Θ-ω X-ray rocking curves of a Si film prepared by ec-LPE on n^+-Si(100). Inset: X-ray diffractogram of Si films prepared by ec-LPE with n^+-Si(100). b) Normalized Raman spectra of n^+-Si(100) seed substrate (black) and an epitaxial Si thin film (red) prepared by ec-LPE using the conditions shown.

Using the Hirsch model, the threading dislocation density in the film was calculated to be on the order of 9 x 10^7 cm^{-2}. Figure 4.6b) shows a representative Raman spectra of a Si epifilm grown by ec-LPE. The c-Si phonon mode at 520 cm^{-1} was redshifted to 512 cm^{-1} and significantly broadened, consistent with our observation that the Si lattice was heavily substitutionally doped with Ga.[35]

The cessation of the electrodeposition bath was hypothesized to occur as a result of coalesced Si^0 accumulating on the electrode surface, therein blocking any subsequent dissolution of depositing Si^0 into the *e*-GaIn electrode. To test this hypothesis, a pulsed electrodeposition waveform applied to the Si ec-LPE experiment, as shown schematically in Figure 4.7a) in order that following a short period of biasing to generate Si^0 at the liquid metal surface, a long rest period at a potential absenting any redox reaction could enable complete dissolution of Si^0 to regenerate a clean electrode surface for the next electrodeposition pulse. The chronoamperometric trace of a Si ec-LPE experiment from an electrolyte containing 0.5 M $SiCl_4$ and 0.1 M $(C_4H_9)_4NCl$ in propylene carbonate at T = 125 °C, with the electrolyte refreshed after every hour, was performed using pulse steps at E_1 = -1.6 V for 0.2 ms, E_2 = -0.77 V for 10 ms, for a total of 3 hrs. Throughout the course of each hour the current was sustained at nominally the same density, supporting the notion that the electrode surface remained clean following each pulse cycle. To account for any evaporative loss of $SiCl_4$ the solution was changed every hour and afforded the same current response. The macroscopic image of the resultant deposit is shown in Figure 4.7c) demonstrating a contiguous deposit consistent with the observations made used direct chronoamperometric deposition. A cross-section scanning electron micrograph of an approximately 3 μm thick Si film is shown in Figure 4.7d). The crystallinity of the film was probed by electron back scatter diffraction as shown in the map collected from 1040 individual EBSD patterns over the area probed

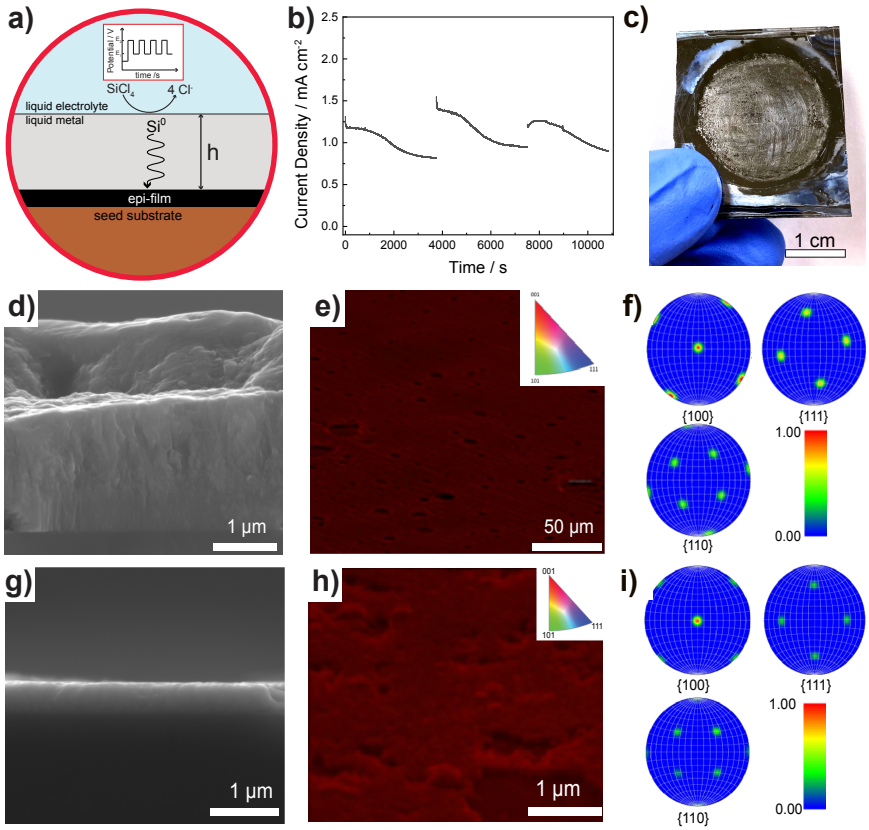


Figure 4.7 a) Schematic depictions of the electrodeposition condition employed in b) Representative chronoamperometric trace of a Si ec-LPE pulsed electrodeposition experiment (E_1 = -1.6 V for 0.2 ms, E_2 = -0.77 V for 10 ms) from electrolyte containing 0.5 M $SiCl_4$ and 0.1 M $(C_4H_9)_4NCl$ in propylene carbonate at T = 125 °C, with the electrolyte refreshed after every hour. c,g) Macroscopic image of deposit obtained on the n^+-Si(100) electrode after electrolysis and subsequent liquid metal removal. d,g) Cross-section scanning electron micrograph of Si ec-LPE sample grown at T = 125 and 23 °C, respectively e,h) Color-coded electron back scatter diffraction (EBSD) map of Si ec-LPE sample grown at T = 125 and 23 °C, respectively. f,i) Contour pole figures from the EBSD mapping shown along the 110 and 111 poles of Si ec-LPE sample grown at T = 125 and 23 °C, respectively.

in Figure 4.7e) with the corresponding pole figures of the sum patterns shown in Figure 4.7f) demonstrating the epitaxial and single crystalline nature of the film. Previously, we reported that the electrosynthesis of c-Si was not observed to occur below 60 ºC.[27] The observation that pulsed electrodeposition enabled the continued growth of thick epitaxial Si thin films motivated exploration of the possibility of Si ec-LPE at room temperature. Data exploring this hypothesis are presented in Figure 4.7g-i) and Figure 8. A cross-sectioned film of a sample obtained by a Si ec-LPE experiment from an electrolyte containing 0.5 M $SiCl_4$ and 0.1 M $(C_4H_9)_4NCl$ in propylene carbonate at T = 23 °C was performed using pulse steps at E_1 = -1.6 V for 0.2 ms, E_2 = -0.77 V for 10 ms for a total of three hours is shown in Figure 4.7g). For the same duration of time as a sample grown at 125 ºC, a film grown at 23 ºC grew to a maximum of 500 nm. The crystalline structure of this film was assessed using a combination of transmission electron microscopy and electron back scatter diffraction. Figure 4.7h) show a top down false colored scanning electron micrograph collected from 8040 individual EBSD patterns collected from the area probed, with the corresponding pole figures shown in Figure 4.7i). The EBSD data confirm that the crystalline structure of the deposit and complete registry with the substrate. A high magnification TEM-HAADF image of the film/substrate interface demonstrating two essential points is shown in Figure 4.8d). First, the atomic continuity across the film/substrate interface again confirmed the epitaxial nature of the growth. Second, there was no amorphous or disordered layer at or near the substrate film/interface showing that even without a significant thermal input, the surface diffusion of Si^0 adatoms within the melt is still sufficient enough to form an ordered structure. Data exploring the variation in material quality at 23 and 125 ºC are shown in Figure 4.8a) and 8b), respectively. Though samples grown at room temperature were demonstrated to be epitaxial across the substrate, compared to samples grown at 125 ºC the atomic clarity in the film was considerably more

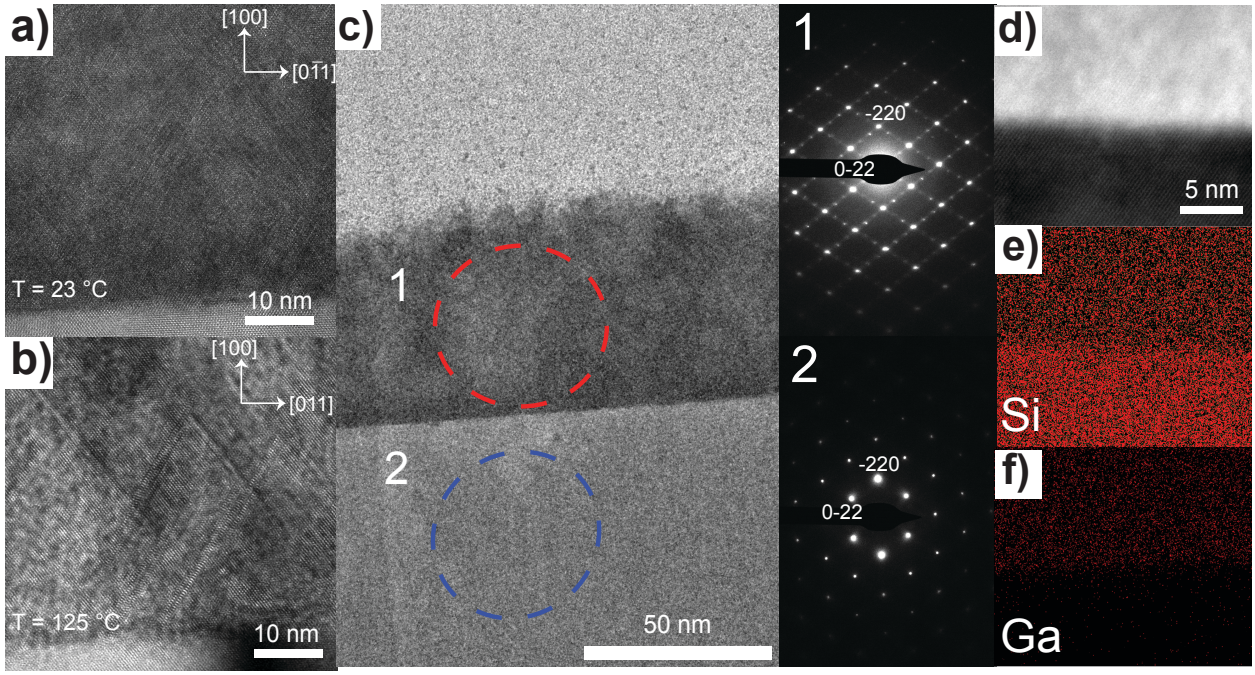


Figure 4.8 a,b) High magnification scanning transmission electron micrograph of a cross section of the Si epifilm grown by pulsed electrodeposition at T = 23 and 125 ºC, respectively. b) Bright field transmission electron micrograph of a cross section of an epitaxial Si film prepared by ec-LPE on a n^+-Si(100) at 125ºC. The red and blue dashed circles correspond to the position of the selected area aperture in 1-2. Shown in 1-2 are partially indexed selected area electron diffraction (SAED) patterns from the epifilm and the substrate respectively. h) STEM-EDS mapping of Si epifilm with elemental maps of Si, Ga shown in i) and j), respectively. Pixel intensities were normalized by the full-area integrated EDS spectra.

obscured, indicating that growth at lower temperature, when all other experimental parameters are held constant, a considerably more defective crystal is produced. To further asses the structure of the epifilm grown at 23 ºC, selected area electron diffraction patterns were collected from (1) the film and (2) the substrate, as shown in Figure 4.8c). Similar to observations made from films grown at 125 ºC, the deposit was shown to be both crystalline and epitaxial with respect to the substrate. However, the electron diffraction pattern shown in Figure 4.8c) has several more diffraction spots. These are known to result from nano- and microtwin stacking faults on the [111] planes, which account for both the satellite peaks but also the double diffraction and Moire fringes observed. Lastly, the elemental composition was probed by STEM-EDS, as shown in Figure 4.8d-f). The film was shown to be Si throughout with a Ga concentration of 19-23 at. %, nearly double the concentration shown at 125 ºC.

4.4 Discussion

The data presented speak cumulatively three points. First, the growth of epitaxial Si thin films by ec-LPE was shown to be possible. Second, the flux of zero valent nuclei in the melt can be controlled by the application of a pulsed waveform to the electrodeposition. Lastly, the materials quality in ec-LPE is directly attributable to the employed growth conditions.

Epitaxial growth of Si by ec-LPE.—The x-ray diffraction, electron microscopy, and electron diffraction data presented here unambiguously demonstrated that the reduction of $SiCl_4$ at a *e*-GaIn thin film electrode led to the formation of Si^0 nuclei that partitioned into the liquid metal, and heterogeneously nucleated as a crystalline epitaxial film on the seed substrate. Critically, the efficacy of this growth process was shown to strongly depend on the applied electrodeposition waveform. This result is neither surprising nor unique to Si ec-LPE. The observation that crystal growth in Si ec-LLS is terminated by the formation of a mixed

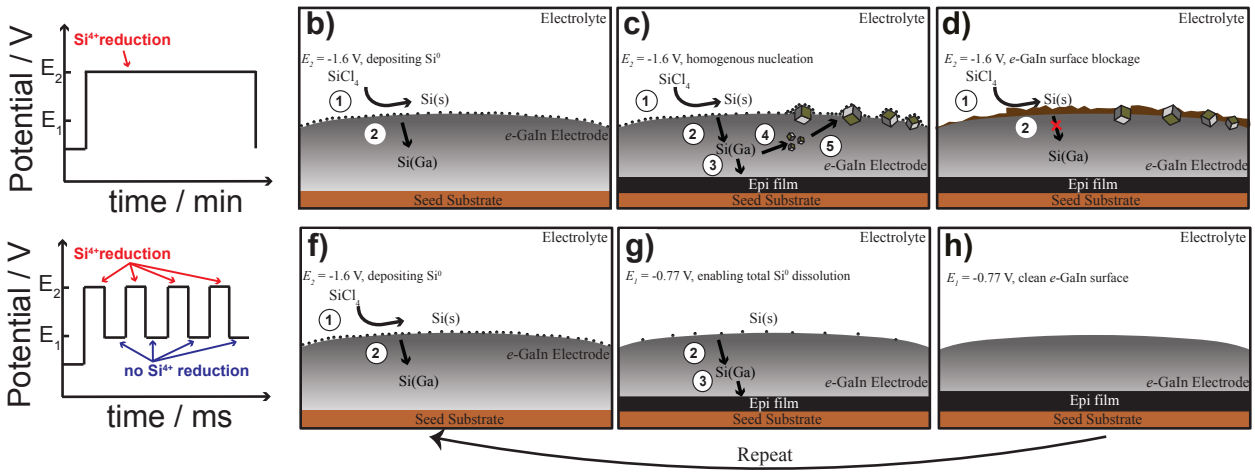


Figure 4.9. Schematic description of the operative pathways in Si ec-LPE during a) direct electrodeposition and e) pulsed electrodeposition, composed of the operative steps shown in b-d) and f-h), respectively.

crystalline and amorphous Si matrix on the melt surface has been previously made using a bulk e-Ga pool working electrode.[12, 36] The observation that an excess flux of Si^0 creates an amorphous layer has also been observed in the vapor-liquid-solid growth of Si wires.[37] Here, similar observations were made following the direct electrodeposition of Si from $SiCl_4$. The presence of crystalline Si both as a film on the substrate but also as crystallites at the liquid metal surfaces demonstrated that the direct electroreduction of $SiCl_4$ simultaneously promoted hetero- and homogenous crystalline Si growth. We hypothesize that the concomitance of these processes is a result of the rates of (1) accommodation of Si^0 across the liquid metal surface, (2) diffusion of dissolved Si^0 into the liquid metal film, and (3) change in the concentration gradient of Si^0 during electrolysis. Owing to the high density of crystalline Si near the liquid metal surface we surmise that even near ambient conditions, the rate of (1) is not a limiting aspect of this system. If (1) were limiting, the timescale of surface diffusion would be long enough that freshly deposited Si^0 nuclei could aggregate to form clusters and eventually coalesce into a purely amorphous film on the liquid metal surface, therein absenting any crystalline Si. This was not observed. Instead, the cessation of crystal growth in Si ec-LPE is understood to be strongly dependent on the rates of (2) and (3). At the temperatures explored here, extrapolation of the liquidus line in the Si-Ga system enables an estimate that the solubility of Si in Ga is 1×10^{-7} at. % at 125 ºC, and 2×10^{-10} at. % at 23 ºC. [26-27] The rate of diffusion of Si in Ga at 23 and 125 ºC are approximately 3×10^{-8} and 3×10^{-8} $cm^2\ s^{-1}$, respectively.[26] The conjunction of the extremely small equilibrium concentration and slow diffusion rate of Si in Ga based melts implies the rapid build-up of large concentration gradients under conditions of continuous Si^0 flux. Shown in Figure 4.9a-d) is a schematic depiction relating these hypotheses to the observed amperometric waveform. At the start of the electrodeposition experiment, $SiCl_4$ is reduced to Si^0 as discrete

nuclei and partition across the liquid metal/liquid electrolyte barrier, as shown in Figure 4.9b). The diffusion of dissolved Si^0 down to the seed crystal interface occurs, and heterogenous nucleation and subsequent crystal growth take place. However, as described schematically in Figure 4.9c), we postulate that constant flux of Si^0 into the melt causes the equilibrium concentration to be rapidly exceeded within the liquid metal, resulting in the birth of nascent critical nuclei and causing diffusing Si^0 atoms in the melt to feed both homo- and heterogenous nucleation and crystal growth processes simultaneously. Ultimately, as shown in Figure 4.9d), the emergence of homogenously nucleated crystals at the liquid electrolyte/liquid metal interface provides a solid surface for seeding the growth of an amorphous Si film, which eventually covers the electrode surface, preventing any further partition of Si^0 nuclei into the melt. Cumulatively, while Si ec-LPE does take place during direct electrodeposition of $SiCl_4$, the continued flux of Si^0 into the melt is understood to accompany immutable parasitic side-process that limit both the obtainable film thickness to <200 nm and the faradaic efficiency of growth to <5%.

Pulsed electrodeposition significantly alters the observed crystal growth dynamics. An annotated example of the recorded electroreduction pulses are shown in Fig 4.9e). Simply, the pulsed electrodeposition method seeks to (1) generate small amounts of Si^0 by electroreduction and (2) enable all reduced Si^0 to dissolve, diffuse, heterogeneously nucleate and allow the liquid metal to return to initial equilibrium conditions. Here, a rest pulse width—the period where no Si^0 is generated—was selected to be 10 ms, in order that more than ample time was allowed for the diffusion of reduced Si^0 in the melt. As shown schematically in Fig 4.9f), the first potential step drives the reduction of $SiCl_4$ to Si^0 at the liquid metal/liquid electrolyte interface. In Fig 4.9g), the applied potential is held where no redox reactions occur, and any residual deposited Si^0 is allowed to dissolve and nucleate heterogeneously. After a sufficiently long period of time, any

excess Si^0 in the liquid metal will have nucleated and the melt will be at equilibrium conditions, enabling the cycle to start again, as shown in Fig 4.9h).

The application of a pulsed electrodeposition waveform to the ec-LPE platform introduces a new paradigm to the growth of covalent and inorganic crystalline solids by electrodeposition at liquid metal electrodes. The cumulative observations here show that pulsed electrodeposition in ec-LPE enables thick epitaxial films of Si and circumvents the previous barriers in low temperature crystalline Si growth. Previous work from our group set the thermal limits of crystalline Si growth from liquid metal electrodes to 65 ºC, though macroscopic thick thin films were obtained temperatures as low as 23 ºC, suggesting that the problems accompanying small equilibrium concentrations and slow diffusion rates are not intrinsically limiting. In the canon of crystal growth, low-temperature crystalline Si growth has been pursued for decades, but with limited success. Using vacuum systems crystalline Si can be grown near ambient conditions, but are intrinsically limited in thickness before epitaxial breakdown occurs. In conventional liquid phase epitaxy, low solubility of solute was an Achilles heel that limited the thermal range over which epitaxial growth could be feasibly grown, given both the rapid depletion of the saturated melt and the slow growth rates.[38-40] The work shown here represents the first practical demonstration of thick, macroscopic epitaxial Si thin films at ambient temperatures. Here, the synergistic combination of the kinetic control afforded by electrochemistry to stop and start the feed of Si^0 into liquid metal, at will, in conjunction with the melt growth dynamics of conventional liquid phase epitaxy to deposit ordered structures, affords a unique mechanism by which the saturation of a liquid metal solution can be controlled. Accordingly, this work sets the stage for more broadly exploring electrodeposition as a disruptive strategy for the growth of crystalline solids using liquid metal electrodes. Principally,

the only limitation to grow a crystalline solid from a liquid metal is that the chosen has solute has some finite miscibility.

Materials Quality in Si ec-LPE.—The epitaxial Si thin films grown here are unique for several reasons. The junction between the Si epifilm and the Si substrate is atomically abrupt, and no inter-diffusion of dopants was observed, which is to be expected given the low temperature growth conditions employed here. Significantly, the establishment of a simplistic low-temperature methodology for heterojunction device architecture has been a longstanding challenge.[41-43] While the material shown here are not applicable for any electronic or photovoltaic purposes directly, the atomic continuity across the interface and hyperdoped p^+ nature of the films open new avenues for the fabrication of epitaxial rear emitters in solar cell technologies.[44-45]

The cumulative x-ray and electron diffraction data suggest that the both the composition and overall defectiveness of the resulting epifilm was a direct consequence of the employed experimental conditions. The observation prior to film coalescence that growth is initiated by the seeding of 3D nuclei is not unique to Si ec-LPE. Numerous reports from the liquid phase epitaxy literature note that the growth, even near equilibrium conditions, is similarly seeded by three dimensional nuclei.[38-40, 46-56] Accordingly, as no evidence of any 2D film preceding island growth was observed, the epitaxial growth mode here is ascribed to the Volmer-Weber growth mode. This would also be anticipated given previous reports from our group in which the analogous Ge in Ga system was shown to have crystal growth initiated at supersaturations in the range of 10^4, considerably far above the predicted boundary for unstable 3D crystal growth.[24] In conjunction with the observed Volmer-Weber growth mode, the variation in both the defects and gallium concentration as a function of the growth condition is unsurprising, but significant for two

reasons. First, the initial nucleation of Si in LPE from Ga-based solutions results from dislocation-controlled facet-growth. That is, for on-axis substrates, the incorporation of Ga solvent into a nascent Si cluster acts as a continued source of growth steps, resulting in a spiral-like growth that forms pyramidal structures on (100) and flat trigonal pyramids on (111) surfaces.[57-58] Since the nucleation seeding mechanism is the same in Si epitaxy from the melt irrespective of temperature, the variation in the defect density between Si films grown at 23 and 125 ºC is a direct measure of the difference in the supersaturation of Si in Ga during the growth. Specifically, with the same flux of Si^0 resulting from each deposition pulse, the variation in the defect density should then be directly related to the heterogenous crystal nucleation density, which increases with supersaturation, as shown schematically in Figure 4.10. The coalescence of discrete 3D crystal islands is often accompanied by line defects that propagate into the film. Thus, with higher supersaturation will be accompanied by a higher nucleation density and therefore a more defected crystal will result. Similarly, the tendency of Ga to incorporate in a growing Si film is purported to also be dependent on the nucleation density. Previous reports from the Si LPE literature assert that the incorporation of Ga impurities in the growing crystalline Si film occurs preferentially on defected (111) planes.[59] Consequently, growths on (100) oriented substrate surfaces under higher supersaturation conditions will have a higher nucleation density and incorporate more Ga into the lattice, as demonstrated here. Cumulatively, these results implicate the notion that supersaturation in ec-LLS based processes is tunable and can allow for crystal growth engineering.

Lastly, it should be noted that the tendency of the epifilms grown here to incorporate Ga above the solid solubility limit in Si, as well as the high density of defects is of potentially significant technological interest. As the dimension of transistors in integrated circuits continues

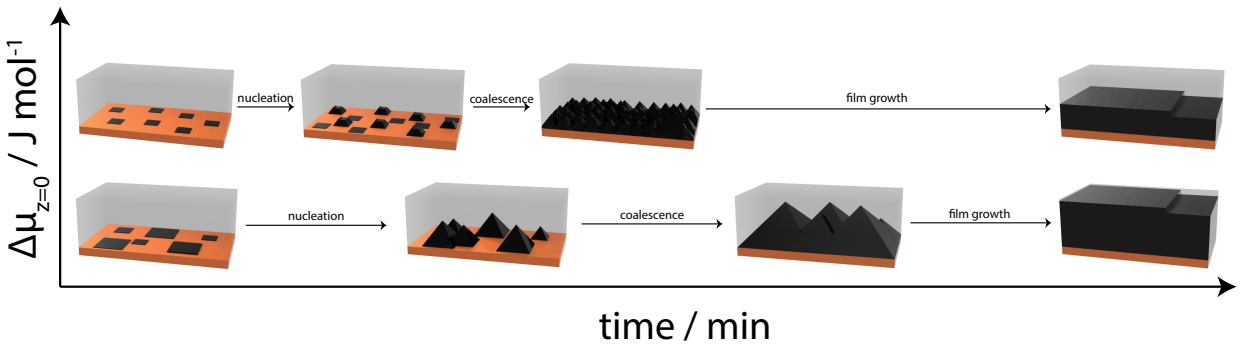


Figure 4.10 Schematic description of the dominant modes of epifilms growth under conditions of low supersaturation (bottom row), where large epitaxial grains predominantly grow, and under conditions of high supersaturation (top row) where the driving force is sufficient for nucleation to predominate over continued nuclei growth. In both cases, following coalescence of neighboring nuclei, a film is formed which continues to grow in a step flow growth-mode.

to near the atomic scale, interest has risen in quantum computing. One significant challenge in the production of quantum computers is the fabrication of quantum circuits using superconductors with high superconductivity that remain stable even down to the milikelvin range.[60] Recent studies have shown that hyperdoped Ga in Si is of particular interest, owing to the superconductivity of the Ga precipitates that can form in the lattice.[60-61] While advances have been made in the fabrication of hyperdoped Ga in Si, these methods rely entirely on ion bombardment that destroys the Si lattice locally and result in a non-uniform distribution of Ga.[60, 62] The method shown here demonstrates the first homogenously hyperdoped Ga in Si thin film, which can be made on the order of microns in thickness with simple laboratory equipment. Similarly, though Si has the highest theoretical Li-ion capacity, it has found no significant employ as an anode material due to its propensity to fracture after just a few cycles.[63] Here, both the presence of a high density of defects and hyperdoped Ga may significantly enhance the cycling lifetime of Si under high load, given previously reports on the stabilizing effects of both defects in crystalline solids and the unit cell expansion induced by Ga substitutional doping.[34, 64]

4.5 Conclusions

This work details the application of ec-LPE to the growth of Si thin films. Though the direct electrodeposition of $SiCl_4$ was shown to produce epitaxial Si thin films, owing to the metallurgical properties of Si with *e*-GaIn at low temperatures, the growth was fundamentally limited by the formation of a blocking layer that inhibited further deposition. Here, for the first time, pulsed electrodeposition was employed to compensate for the slow dissolution of Si, resulting in the growth of thick epifilms. The materials quality of the resultant pulsed electrodeposition grown epifilms was shown to strongly depend on the experimental conditions

employed. Accordingly, this work sets the stage for further investigations to explore the range of crystalline quality obtainable by ec-LPE.

4.6 References

1. Looney, B., BP statistical review of world energy. *BP Report, London, UK* **2020**.
2. Wilson, G. M.; Al-Jassim, M.; Metzger, W. K.; Glunz, S. W.; Verlinden, P.; Xiong, G.; Mansfield, L. M.; Stanbery, B. J.; Zhu, K.; Yan, Y.; Berry, J. J.; Ptak, A. J.; Dimroth, F.; Kayes, B. M.; Tamboli, A. C.; Peibst, R.; Catchpole, K.; Reese, M. O.; Klinga, C. S.; Denholm, P.; Morjaria, M.; Deceglie, M. G.; Freeman, J. M.; Mikofski, M. A.; Jordan, D. C.; TamizhMani, G.; Sulas-Kern, D. B., The 2020 photovoltaic technologies roadmap. *Journal of Physics D: Applied Physics* **2020,** *53* (49), 493001.
3. Anglin, E. J.; Cheng, L.; Freeman, W. R.; Sailor, M. J., Porous silicon in drug delivery devices and materials. *Advanced Drug Delivery Reviews* **2008,** *60* (11), 1266-1277.
4. Maldonado, S., The Importance of New "Sand-to-Silicon" Processes for the Rapid Future Increase of Photovoltaics. *ACS Energy Letters* **2020,** *5* (11), 3628-3632.
5. Lee, J. G.; Miller, P. D.; Cutler, I. B., Carbothermal Reduction of Silica. In *Reactivity of Solids*, Wood, J.; Lindqvist, O.; Helgesson, C.; Vannerberg, N.-G., Eds. Springer US: Boston, MA, 1977; pp 707-711.
6. Elwell, D., Electrocrystallization of semiconducting materials from molten salt and organic solutions. *Journal of Crystal Growth* **1981,** *52*, 741-752.
7. Elwell, D.; Feigelson, R. S., Electrodeposition of solar silicon. *Solar Energy Materials* **1982,** *6* (2), 123-145.
8. Cohen, U., Some prospective applications of silicon electrodeposition from molten fluorides to solar cell fabrication. *Journal of Electronic Materials* **1977,** *6* (6), 607-643.
9. Ouyang, G.; Gu, M. X.; Fu, S. Y.; Sun, C. Q.; Zhu, W. G., Determination of the Si-Si bond energy from the temperature dependence of elastic modulus and surface tension. *EPL (Europhysics Letters)* **2008,** *84* (6), 66005.
10. Lee, C. H.; Kröger, F. A., Cathodic Deposition of Amorphous Alloys of Silicon, Carbon, and Fluorine. *Journal of The Electrochemical Society* **1982,** *129* (5), 936-942.
11. Bechelany, M.; Elias, J.; Brodard, P.; Michler, J.; Philippe, L., Electrodeposition of amorphous silicon in non-oxygenated organic solvent. *Thin Solid Films* **2012,** *520* (6), 1895-1901.
12. Zhang, J.; Chen, S.; Zhang, H.; Zhang, S.; Yao, X.; Shi, Z., Electrodeposition of crystalline silicon directly from silicon tetrachloride in ionic liquid at low temperature. *RSC Advances* **2016,** *6* (15), 12061-12067.
13. Zou, X.; Ji, L.; Ge, J.; Sadoway, D. R.; Yu, E. T.; Bard, A. J., Electrodeposition of crystalline silicon films from silicon dioxide for low-cost photovoltaic applications. *Nature Communications* **2019,** *10* (1), 5772.
14. Zein El Abedin, S.; Borissenko, N.; Endres, F., Electrodeposition of nanoscale silicon in a room temperature ionic liquid. *Electrochemistry Communications* **2004,** *6* (5), 510-514.
15. Munisamy, T.; Bard, A. J., Electrodeposition of Si from organic solvents and studies related to initial stages of Si growth. *Electrochimica Acta* **2010,** *55* (11), 3797-3803.

16. Gobet, J.; Tannenberger, H., Electrodeposition of Silicon from a Nonaqueous Solvent. *Journal of The Electrochemical Society* **1988,** *135* (1), 109-112.
17. Nicholson, J. P., Electrodeposition of Silicon from Nonaqueous Solvents. *Journal of The Electrochemical Society* **2005,** *152* (12), C795-C802.
18. Agrawal, A. K.; Austin, A. E., Electrodeposition of Silicon from Solutions of Silicon Halides in Aprotic Solvents. *Journal of The Electrochemical Society* **1981,** *128* (11), 2292-2296.
19. Boen, R.; Bouteillon, J., The electrodeposition of silicon in fluoride melts. *Journal of Applied Electrochemistry* **1983,** *13* (3), 277-288.
20. Rao, G. M.; Elwell, D.; Feigelson, R. S., Electrowinning of Silicon from K 2SiF6 - Molten Fluoride Systems. *Journal of The Electrochemical Society* **1980,** *127* (9), 1940-1944.
21. Cho, S. K.; Fan, F.-R. F.; Bard, A. J., Electrodeposition of Crystalline and Photoactive Silicon Directly from Silicon Dioxide Nanoparticles in Molten CaCl2. *Angewandte Chemie International Edition* **2012,** *51* (51), 12740-12744.
22. Zou, X.; Ji, L.; Yang, X.; Lim, T.; Yu, E. T.; Bard, A. J., Electrochemical Formation of a p–n Junction on Thin Film Silicon Deposited in Molten Salt. *Journal of the American Chemical Society* **2017,** *139* (45), 16060-16063.
23. Jin, X.; Gao, P.; Wang, D.; Hu, X.; Chen, G. Z., Electrochemical Preparation of Silicon and Its Alloys from Solid Oxides in Molten Calcium Chloride. *Angewandte Chemie International Edition* **2004,** *43* (6), 733-736.
24. Cheek, Q.; Fahrenkrug, E.; Hlynchuk, S.; Alsem, D. H.; Salmon, N. J.; Maldonado, S., In Situ Transmission Electron Microscopy Measurements of Ge Nanowire Synthesis with Liquid Metal Nanodroplets in Water. *ACS Nano* **2020,** *14* (3), 2869-2879.
25. Demuth, J.; Fahrenkrug, E.; Ma, L.; Shodiya, T.; Deitz, J. I.; Grassman, T. J.; Maldonado, S., Electrochemical Liquid Phase Epitaxy (ec-LPE): A New Methodology for the Synthesis of Crystalline Group IV Semiconductor Epifilms. *Journal of the American Chemical Society* **2017,** *139* (20), 6960-6968.
26. Gu, J.; Fahrenkrug, E.; Maldonado, S., Direct Electrodeposition of Crystalline Silicon at Low Temperatures. *Journal of the American Chemical Society* **2013,** *135* (5), 1684-1687.
27. Ma, L.; Lee, S.; DeMuth, J.; Maldonado, S., Direct electrochemical deposition of crystalline silicon nanowires at T ≥ 60 °C. *RSC Advances* **2016,** *6* (82), 78818-78825.
28. Fahrenkrug, E.; Maldonado, S., Electrochemical Liquid–Liquid–Solid (ec-LLS) Crystal Growth: A Low-Temperature Strategy for Covalent Semiconductor Crystal Growth. *Accounts of Chemical Research* **2015,** *48* (7), 1881-1890.
29. Downes, N.; Cheek, Q.; Maldonado, S., Electroreduction of Perchlorinated Silanes for Si Electrodeposition. *Journal of The Electrochemical Society* **2021,** *168* (2), 022503.
30. Jiang, X.; Jia, C. L., The coalescence of [001] diamond grains heteroepitaxially grown on (001) silicon. *Applied Physics Letters* **1996,** *69* (25), 3902-3904.
31. Zhai, S.; Zhang, C.; Zhou, N.; Huang, L.; Lin, M.; Zhou, L., The twin formations on different growth planes of silicon crystal growth from melt by a molecular dynamics study. *Physica B: Condensed Matter* **2019,** *572*, 184-189.
32. Westra, J. M.; Vavruňková, V.; Šutta, P.; van Swaaij, R. A. C. M. M.; Zeman, M., Formation of thin-film crystalline silicon on glass observed by in-situ XRD. *Energy Procedia* **2010,** *2* (1), 235-241.
33. Kavanagh, K. L.; Cargill, G. S., Lattice strain from substitutional Ga and from holes in heavily doped Si:Ga. *Physical Review B* **1992,** *45* (7), 3323-3331.

34. Lee, M.; Lee, K.; Ko, D.-H., Structural, bonding, and elastic properties of Si:X (X = B, Al, and Ga): a theoretical study. *Semiconductor Science and Technology* **2020,** *35* (6), 065004.
35. Ureña-Begara, F.; Vayrette, R.; Bhaskar, U. K.; Raskin, J.-P., Raman analysis of strain in p-type doped silicon nanostructures. *Journal of Applied Physics* **2018,** *124* (9), 095102.
36. Zhao, Z.; Yang, C.; Wu, L.; Zhang, C.; Wang, R.; Ma, E., Preparation and Characterization of Crystalline Silicon by Electrochemical Liquid–Liquid–Solid Crystal Growth in Ionic Liquid. *ACS Omega* **2021,** *6* (18), 11935-11942.
37. Bae, J.; Kulkarni, N. N.; Zhou, J. P.; Ekerdt, J. G.; Shih, C.-K., VLS growth of Si nanocones using Ga and Al catalysts. *Journal of Crystal Growth* **2008,** *310* (20), 4407-4411.
38. Linnebach, R.; Bauser, E., Low temperature liquid phase epitaxy of silicon. *Journal of Crystal Growth* **1982,** *57* (1), 43-47.
39. Ogawa, H.; Guo, Q.; Ohta, K., Low temperature liquid phase epitaxy of silicon from gallium solution. *Journal of Crystal Growth* **1995,** *155* (3), 193-197.
40. Zhengrong, S.; Young, T. L.; Green, M. A., Low-temperature liquid phase epitaxy of silicon. *Materials Letters* **1991,** *12* (5), 339-343.
41. Zheng, Y.; Agrawal, M.; Dharmarasu, N.; Radhakrishnan, K.; Patwal, S., A study on GaSi interdiffusion during (Al)GaN/AlN growth on Si by plasma assisted molecular beam epitaxy. *Applied Surface Science* **2019,** *481*, 319-326.
42. Supplie, O.; Romanyuk, O.; Koppka, C.; Steidl, M.; Nägelein, A.; Paszuk, A.; Winterfeld, L.; Dobrich, A.; Kleinschmidt, P.; Runge, E.; Hannappel, T., Metalorganic vapor phase epitaxy of III–V-on-silicon: Experiment and theory. *Progress in Crystal Growth and Characterization of Materials* **2018,** *64* (4), 103-132.
43. Ohlmann, J.; Feifel, M.; Rachow, T.; Benick, J.; Janz, S.; Dimroth, F.; Lackner, D., Influence of Metal–Organic Vapor Phase Epitaxy Reactor Environment on the Silicon Bulk Lifetime. *IEEE Journal of Photovoltaics* **2016,** *6* (6), 1668-1672.
44. Ingenito, A.; Isabella, O.; Zeman, M., Simplified process for high efficiency, self-aligned IBC c-Si solar cells combining ion implantation and epitaxial growth: Design and fabrication. *Solar Energy Materials and Solar Cells* **2016,** *157*, 354-365.
45. Franklin, E.; Fong, K.; McIntosh, K.; Fell, A.; Blakers, A.; Kho, T.; Walter, D.; Wang, D.; Zin, N.; Stocks, M.; Wang, E.-C.; Grant, N.; Wan, Y.; Yang, Y.; Zhang, X.; Feng, Z.; Verlinden, P. J., Design, fabrication and characterisation of a 24.4% efficient interdigitated back contact solar cell. *Progress in Photovoltaics: Research and Applications* **2016,** *24* (4), 411-427.
46. Soo Hong, L.; Healy, S. A.; Young, T. L.; Green, M. A., Very-low-temperature liquid-phase epitaxial growth of silicon. *Materials Letters* **1990,** *9* (2), 53-56.
47. McNeely, J. B.; Hall, R. B.; Barnett, A. M.; Tiller, W. A., Thin-film silicon crystal growth on low cost substrates. *Journal of Crystal Growth* **1984,** *70* (1), 420-426.
48. Baliga, B. J., Silicon Liquid Phase Epitaxy: A Review. *Journal of The Electrochemical Society* **1986,** *133* (1), 5C-14C.
49. Baliga, B. J., Morphology of silicon epitaxial layers grown by undercooling of a saturated tin melt. *Journal of Crystal Growth* **1977,** *41* (2), 199-204.
50. Bergmann, R., Model for defect-free epitaxial lateral overgrowth of Si over SiO2 by liquid phase epitaxy. *Journal of Crystal Growth* **1991,** *110* (4), 823-834.
51. Mattes, B. L.; Route, R. K., LPE growth of GaAs: Formation of nuclei and surface terraces. *Journal of Crystal Growth* **1974,** *27*, 133-141.

52. Gonzatti, F.; Hartmann, J.-M.; Yckache, K., Low and High Temperature Boron and Phosphorous Doping of Si for Junctions and MEMS Purposes. *ECS Transactions* **2019,** *16* (10), 485-493.
53. Sumner, B. E.; Foley, R. T., Liquid-Phase Epitaxial Growth of Gallium-Doped Silicon. *Journal of The Electrochemical Society* **1978,** *125* (11), 1817-1824.
54. Abdou, F.; Fave, A.; Lemiti, M.; Laugier, A.; Bernard, C.; Pisch, A. In *Liquid phase epitaxy of silicon from tin alloys at low temperature*, Conference Record of the Thirty-first IEEE Photovoltaic Specialists Conference, 2005., 3-7 Jan. 2005; 2005; pp 1066-1069.
55. Girault, B.; Chevrier, F.; Joullie, A.; Bougnot, G., Liquid phase epitaxy of silicon at very low temperatures. *Journal of Crystal Growth* **1977,** *37* (2), 169-177.
56. Baliga, B. J., Isothermal Silicon Liquid Phase Epitaxy from Supersaturated Tin. *Journal of The Electrochemical Society* **1978,** *125* (4), 598-600.
57. Bauser, E.; Strunk, H., Dislocations as growth step sources in solution growth and their influence on interface structures. *Thin Solid Films* **1982,** *93* (1), 185-194.
58. Bauser, E.; Strunk, H. P., Microscopic growth mechanisms of semiconductors: Experiments and models. *Journal of Crystal Growth* **1984,** *69* (2), 561-580.
59. Strunk, H. P.; Kessler, A.; Bauser, E., Identification of Growth Induced Planar Defects in Silicon. *MRS Proceedings* **2011,** *62*, 9.
60. Sardashti, K.; Nguyen, T.; Hatefipour, M.; Sarney, W. L.; Yuan, J.; Mayer, W.; Kisslinger, K.; Shabani, J., Tailoring superconducting phases observed in hyperdoped Si:Ga for cryogenic circuit applications. *Applied Physics Letters* **2021,** *118* (7), 073102.
61. Shim, Y.-P.; Tahan, C., Bottom-up superconducting and Josephson junction devices inside a group-IV semiconductor. *Nature Communications* **2014,** *5* (1), 4225.
62. Skrotzki, R.; Fiedler, J.; Herrmannsdörfer, T.; Heera, V.; Voelskow, M.; Mücklich, A.; Schmidt, B.; Skorupa, W.; Gobsch, G.; Helm, M.; Wosnitza, J., On-chip superconductivity via gallium overdoping of silicon. *Applied Physics Letters* **2010,** *97* (19), 192505.
63. Ren, W.-F.; Zhou, Y.; Li, J.-T.; Huang, L.; Sun, S.-G., Si anode for next-generation lithium-ion battery. *Current Opinion in Electrochemistry* **2019,** *18*, 46-54.
64. Wang, J.; Meng, X.; Fan, X.; Zhang, W.; Zhang, H.; Wang, C., Scalable Synthesis of Defect Abundant Si Nanorods for High-Performance Li-Ion Battery Anodes. *ACS Nano* **2015,** *9* (6), 6576-6586.

Chapter 5

Unfinished Works and Conclusions

5.1 Factors Effecting Crystalline Quality

The observation of starkly different materials quality shown in Chapter 5 by the use of pulsed electrodeposition at different temperatures begs the question of the degree of tunability in supersaturation in the ec-LPE method. As discussed in chapter 1, there is an established relationship between growth mode and supersaturation, and thereby the structural quality of the resulting epitaxial layer. In the ideal growth cases, the supersaturation is near zero so growth occurs near equilibrium, enabling the continued nucleation (or adsorption) and dissolution of dissolved semiconductor solute. Under these conditions, the epitaxial growth occurs as monoatomic steps, which confers the highest degree of structural perfection. Consequently, this is the reason for the excellent materials quality of materials grown in LPE. In contrast to LPE, previous reports from our group demonstrate the ec-LLS based processes have unprecedently high supersaturation. Recently using in-situ TEM Cheek et al. demonstrated that during the direct electrodeposition of GeO_2 at liquid Ga droplets, the supersaturation of Ge in the Ga before nucleation occurred was on the order of 10^4.[1] Thus, to get near equilibrium growth conditions at ambient temperatures by ec-LLS based processes requires tuning the supersaturation several orders of magnitude. Herein, efforts taken to examine factors effecting supersaturation tunability are discussed.

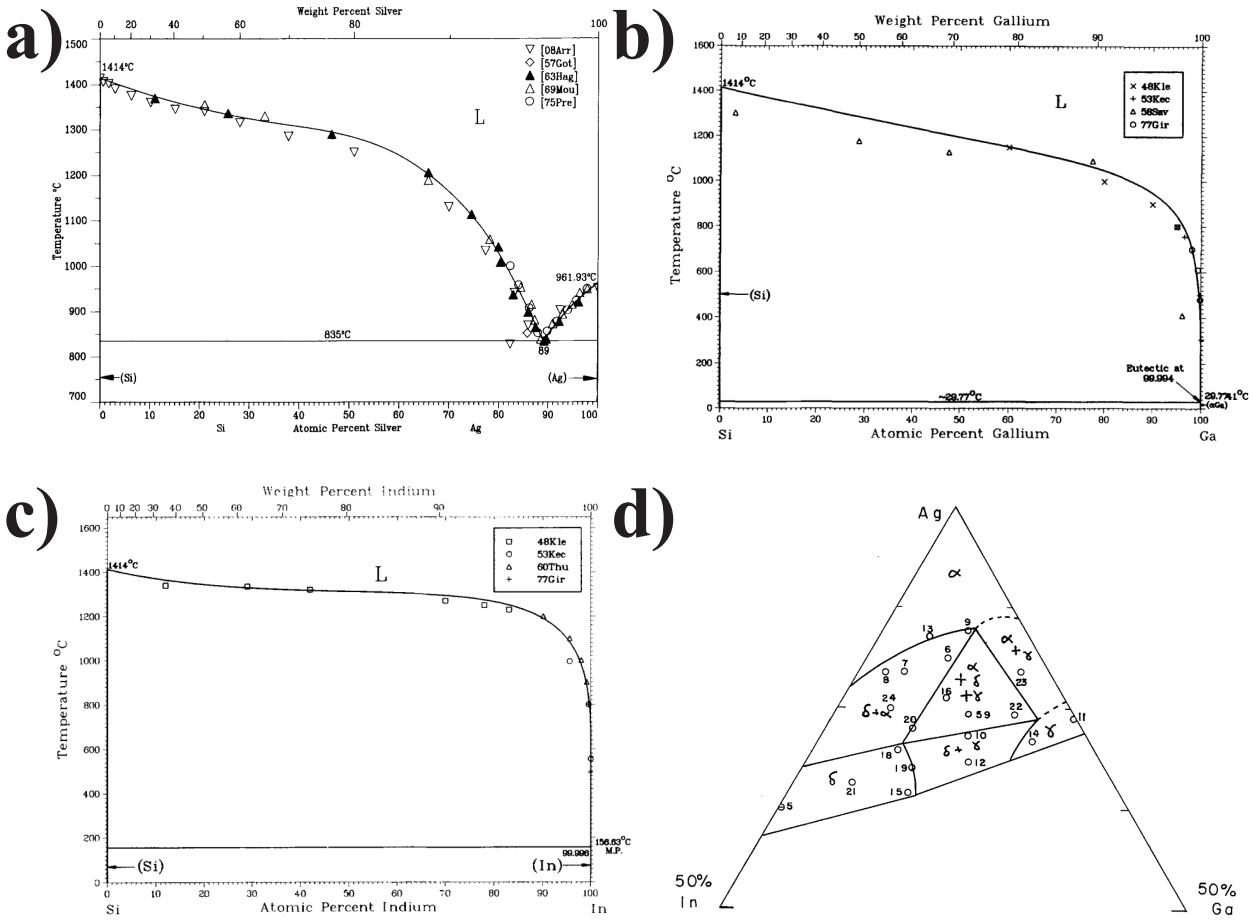


Figure 5.1 Binary phase diagrams of Si in a) Ag, b) Ga, c) In. Reproduced with permissions from Ref. 2, 3, 5. Shown in figure d) ternary equilibrium diagram for the Ga-In-Ag system at room temperature. Reproduced with permission from Ref. 4.

In Si ec-LPE there are several ways to envisage modulating supersaturation. The simplest would be to simply run ec-LPE experiments at much higher temperatures, in order that Si is more soluble in the melt. However, this approach is anathema to the sum objective of devising a low temperature route to crystalline Si thin films. The composition of the liquid metal can also be altered to increase the equilibrium concentration of dissolved Si^0. Previous efforts in our group have examined variation of the In composition in Ga_xIn_{1-x} liquid metal electrodes for Ge microwire growth, though no appreciable difference in microwire purity was observed.[1] Thus, rather than modifying the bulk eutectic composition, which would not appreciably effect the equilibrium of Si as shown in the binary phase diagrams in Figure 5.1b,c), the additions of a dissolved species which forms a deep eutectic with Si is explored instead.[2-5] The list of deep-eutectic forming species with Si includes Al, Ag, Au, Cu, Ni, Pt, and Pd.[6-13] However, in reality, the application of these additives depends on their solubility in *e*-GaIn. Accordingly, Pt, Pd, Ni, Cu, and Au can be immediately ruled out, owing to the formation of solid intermetallic species at ambient temperatures.[14-17] While Al represents an ideal choice for its high solubility in Ga and its deep eutectic with Si, elemental Al is avoided due to its high affinity for oxygen resulting in Al_2O_3 and the irreducibility of the resulting oxide layer.[16, 18] Therefore, Ag represents the best choice for investigation given that it both forms (1) a deep eutectic with Si and (2) a eutectic phase with *e*-GaIn at 2 at.% at room 23 ºC, as shown in Figure 5.1 a,d).[4]

As discussed in Chapter 4, the application of a pulsed electrodeposition waveform to Si ec-LPE enabled the growth of Si epitaxial layers at ambient temperatures. The cumulative materials characterization data showed the resulting epitaxial layer to be of low structural quality. Here, preliminary efforts were taken to be explore the effects of Ag addition on the resulting materials quality in Si ec-LPE. Si ec-LPE pulsed electrodeposition experiments (E_1 = -1.6 V for 0.2 ms, E_2

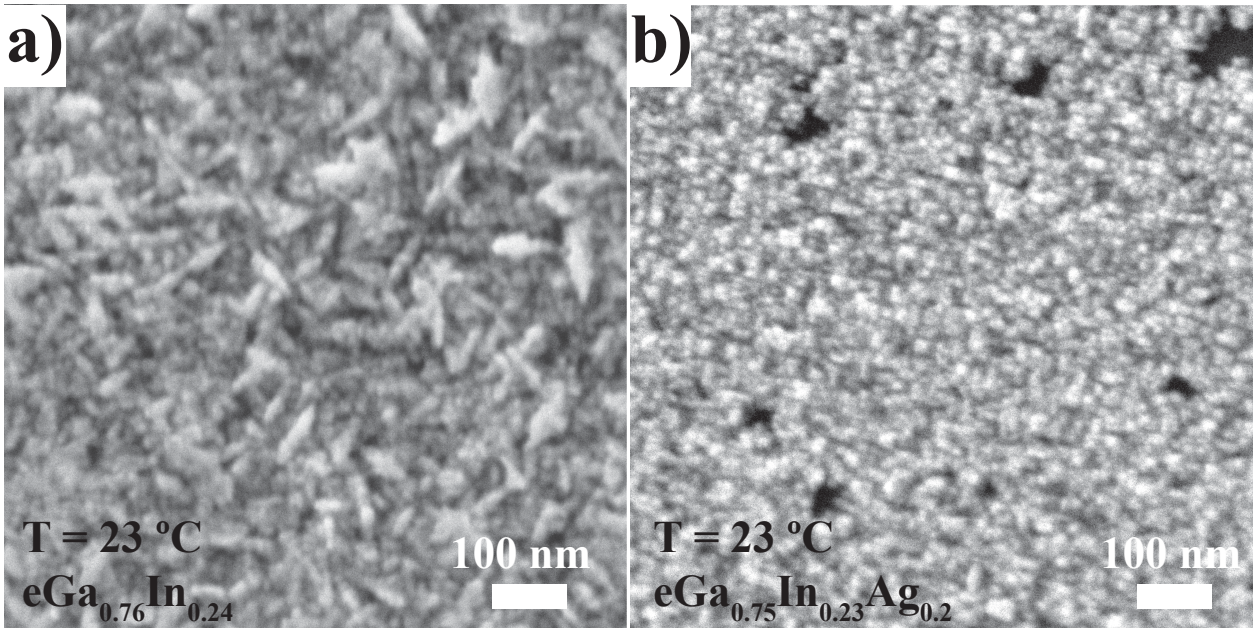


Figure 5.2 Top-down scanning electron micrographs of initial Si deposits in Si ec-LPE pulsed electrodeposition experiment (E_1 = -1.6 V for 0.2 ms, E_2 = -0.77 V for 10 ms) from electrolyte containing 0.5 M $SiCl_4$ and 0.1 M $(C_4H_9)_4NCl$ in propylene carbonate at T = 23 °C with n^+-Si(100) seed substrates using a) *e*-GaIn and b) *e*-GaInAg electrodes.

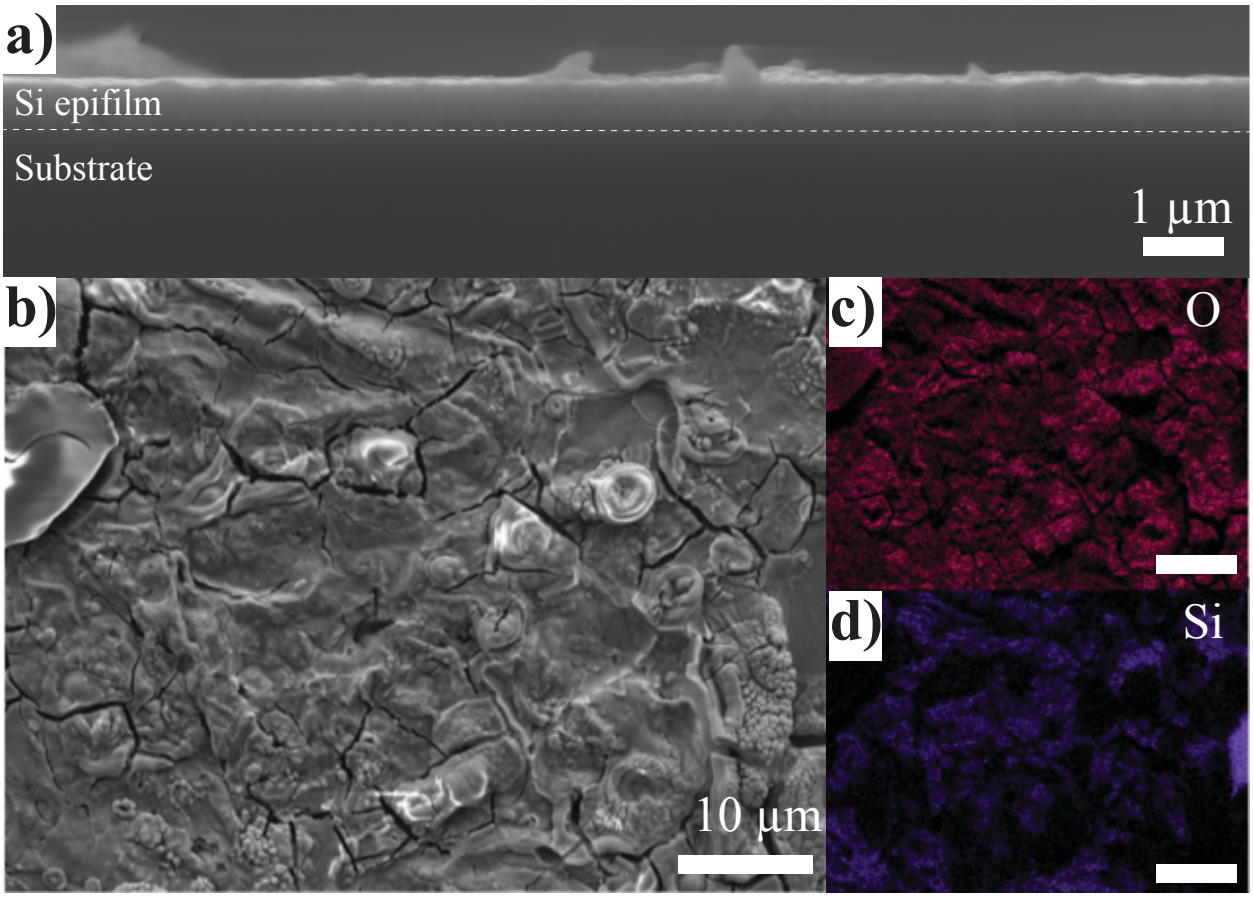


Figure 5.3 a) Cross section scanning electron micrograph of a deposits obtained by Si ec-LPE pulsed electrodeposition experiment (E_1 = -1.6 V for 0.2 ms, E_2 = -0.77 V for 10 ms) performed for 24 hr from electrolyte containing 0.5 M $SiCl_4$ and 0.1 M $(C_4H_9)_4NCl$ in propylene carbonate at T = 23 °C with n^+-Si(100) seed substrates using *e*-GaInAg electrode. b) Top down scanning electron micrograph of the liquid metal surface with corresponding energy dispersive spectroscopy elemental maps of c) O and d) Si.

= -0.77 V for 10 ms) from electrolyte containing 0.5 M $SiCl_4$ and 0.1 M $(C_4H_9)_4NCl$ in propylene carbonate at T = 23 °C were performed for 30 min using *e*-GaIn and *e*-GaInAg electrodes in order to observe a variation in the nucleation of Si. Scanning electron micrographs of the corresponding deposits are shown for *e*-GaIn and *e*-GaInAg electrodes in Figure 5.2 a) and b), respectively. For both liquid metal compositions, the nucleation density is large and the resulting nuclei size on the nanometer scale. However, for the *e*-GaInAg electrode grown deposit, the nuclei are more faceted and with much less three-dimensional coarsening. Experiments were performed in the same manner for 24hr in order to synthesize thick epitaxial films to analyze by X-ray diffraction. However, in both cases, as shown in Figure 5.3b) the long electrodeposition duration resulted in thin epitaxial films (<500 nm) and the liquid metal surface had an appreciable quantity of oxidized silicon material implicating the growth of a blocking layer under these conditions as shown in Figure 5.3b-d). When the same electrodeposition was performed at T = 65 ºC, the obtained material layer was over 1 μm thick for the same period of time as shown in Figure 5.4a). Elemental analysis of the deposited film by energy dispersive x-ray spectroscopy, shown in Figure 5.4b), demonstrates that the film had a significantly smaller proportion of doped metal impurity (~6 at.%) than discussed in Chapter 4 (10-23 at.%). Characterization of the film by coupled scan x-ray diffractometry showed a small epilayer peak shifted 0.21º from the substrate peak, which is consistent with the anticipated shift for a Si thin film doped with 6 at.% of Ga.[19] Cumulatively, the preliminary data shown here suggest that the addition of Ag to the melt can alter the resulting materials quality, though more work will be needed to prove this hypothesis.

Separate attempts to define the consequences of the experimental condition on the supersaturation and thus the resulting Si ec-LPE growth mode at T = 125 ºC were attempted. Specifically, systematic variation to the liquid metal additive (here, provided by dissolution of a

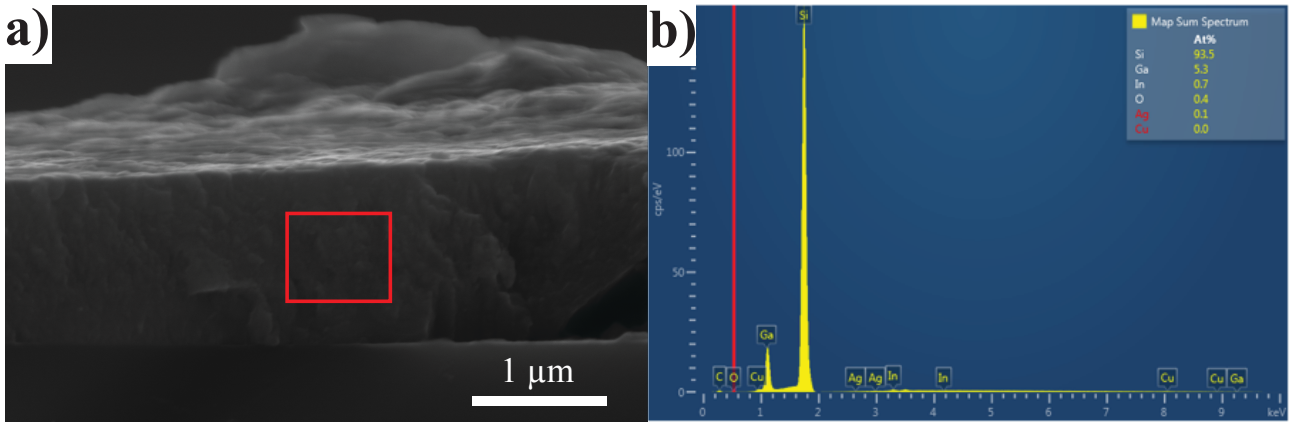


Figure 5.4 Scanning electron micrograph cross section of a Si films prepared from a 4 hour Si ec-LPE pulsed electrodeposition experiment (E_1 = -1.6 V for 0.2 ms, E_2 = -0.77 V for 10 ms) from an electrolyte containing 0.5 M $SiCl_4$ and 0.1 M $(C_4H_9)_4NCl$ in propylene carbonate at T = 65 °C on a n^+-Si(100) seed substrates using *e*-GaInAg electrode. b) EDS mapping of the red box in the Si epifilm shown in a).

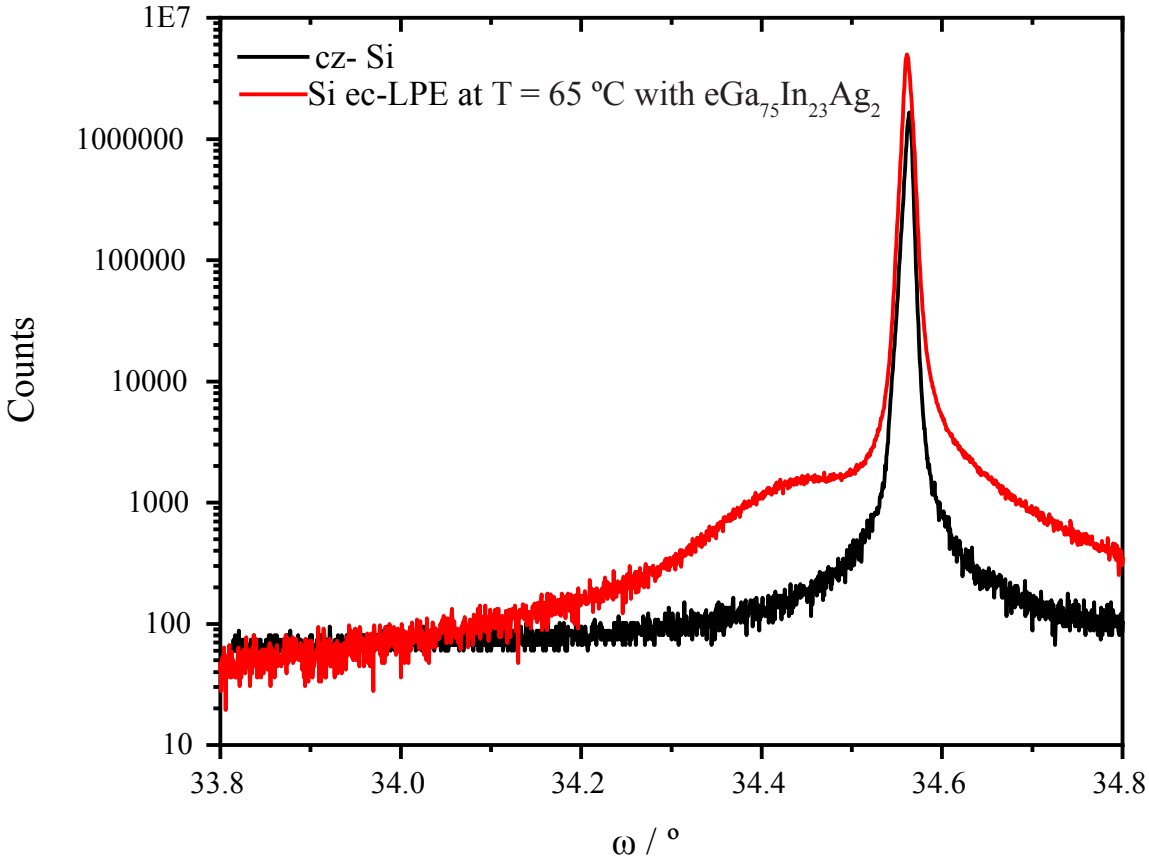


Figure 5.5 Representative coupled 2Θ-ω X-ray rocking curves of the Si ec-LPE film shown in Figure 5.3a).

known thickness of metal wetting layer), the length of the resting pulse duration, and the electrolyte concentration of $SiCl_4$. The result of these experiments is shown in Figure 5.6. As the rest pulse duration was increased, the morphology of the obtained deposit went from large discrete 3D islands to a fully coalesced film. The transition from discrete islands to a coalesced film occurred faster for Ag at shorter rest pulse durations than for Cu or Sn enriched liquid metal electrodes. These results separately implicate the notion that supersaturation is being directly modulated in this system. Here, longer rest pulse durations are understood to enable the Si^0 nuclei deposited in the reduction pulse step to completely dissolve, diffuse, and heterogeneously nucleate, allowing the liquid metal to return to closer to its equilibrium conditions. When shorter pulses are used, residual Si^0, either in the melt or still dissolving from the prior reduction steps, slowly accumulates and causes a large gradient in the melt. This consequence is seen directly in the growth of the heterogeneously nucleated crystals. At large supersaturations, the anisotropic growth of Si crystallites on the [100], [110], and [111] planes should be exacerbated, leading to large discrete nuclei; at lower supersaturations, the growth should be more equivalent on all faces and lead to a smooth film. Both the liquid metal additive and the rest pulse duration follow this trend. Reducing the $SiCl_4$ concentration in the electrolyte from 500 mM to 50 mM demonstrates the same morphological trend with rest potential duration. However, in stark contrast to the expectation that lower supersaturation should reduce the nucleation density when 50 mM $SiCl_4$ was used the nucleation density increased. While these results serve as a useful qualitative description of the effects of experimental condition on the crystal growth in Si ec-LPE, more work is needed to expand on the effect of the $SiCl_4$ electrolyte concentration. Future workers should ensure that when comparing between different ec-LPE runs, data is collected from roughly the same region on the electrode surface (i.e. near the edge, in the center, etc.).

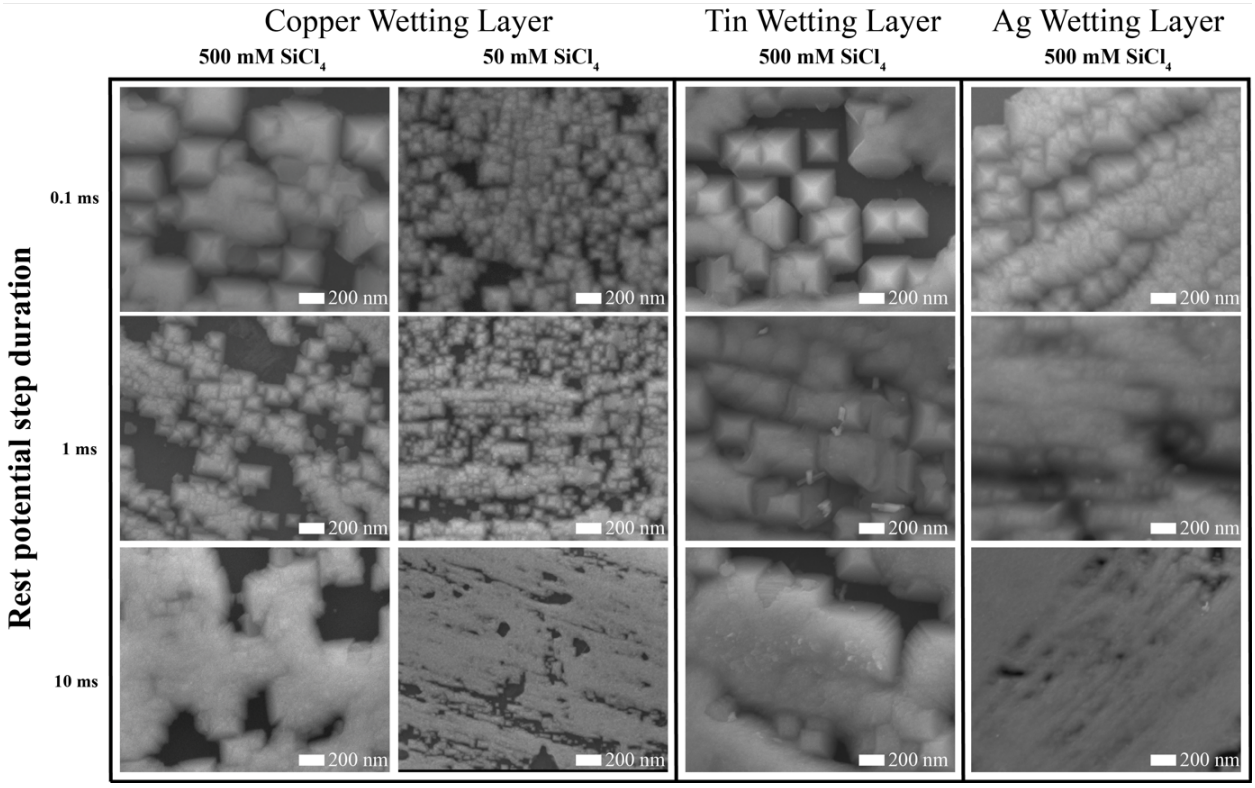


Figure 5.6 Shown is a compilation of top-down scanning electron micrographs organized as a function of the rest potential pulse duration, the liquid metal additive provided by dissolution of the wetting layer, and the concentration. All Si thin films were prepared from a 1 hour Si ec-LPE pulsed electrodeposition experiment (E_1 = -1.6 V for 0.2 ms, E_2 = -0.77 V for 0.1, 1, or 10 ms) from an electrolyte containing 0.05 or 0.5 M $SiCl_4$ and 0.1 M $(C_4H_9)_4NCl$ in propylene carbonate at T = 65 °C on a n^+-Si(100) seed substrates using *e*-GaIn electrodes with 20 nm Cu, Sn, or Ag wetting layers.

5.2 Development of a Method to Produce Liquid Metal Thin Films without Compression

A salient challenge in ec-LPE is the formation of a contiguous liquid metal thin film. While the cell described in Chapter 4 has been used to great success for thin film synthesis, this was accomplished with extensive effort. That is, there is a significant upfront time investment needed to simply assemble the ec-LPE cell since each component has to be handmade every time an experiment is performed. Specifically, the SiC membranes used in ec-LPE are made from a commercially available hierarchically structured flatsheet membrane—intended for water filtration—which necessitate a large sum of steps to create the membranes that constrain the electrolyte area and provide for liquid metal flow through the ports. The crystal seed substrates were similarly processed through a large sum of degreasing, etching, metal coating, and photolithography steps required to both define the liquid metal thin film height and to create intimate contact between the liquid metal and seed substrate. Lastly, and most critically, the force sensor resistor (FSR) used to monitor the internal pressure in the ec-LPE cells is prone to breaking. Since the readout from each FSR varies greatly, each broken FSR stack requires extensive effort to calibrate in order that the user knows the cell is pressurized or filled with liquid metal completely. Accordingly, while the ec-LPE cell described in Chapter 4 has found great utility for demonstrating proof-of-concept epitaxial thin film growth, future experimental efforts would be greatly streamlined with a separate, simpler method for forming contiguous liquid metal thin film electrodes absenting these components. To this end, this section describes the first steps towards liquid metal thin film electrodes, absenting the use of compression. Recently, Hirsch et. al demonstrated the possibility of capitalizing on the lyophobicity of liquid metals when in contact with a compositionally similar solid (e.g. liquid Ga on $AuGa_2$) and the ability of a microstructured

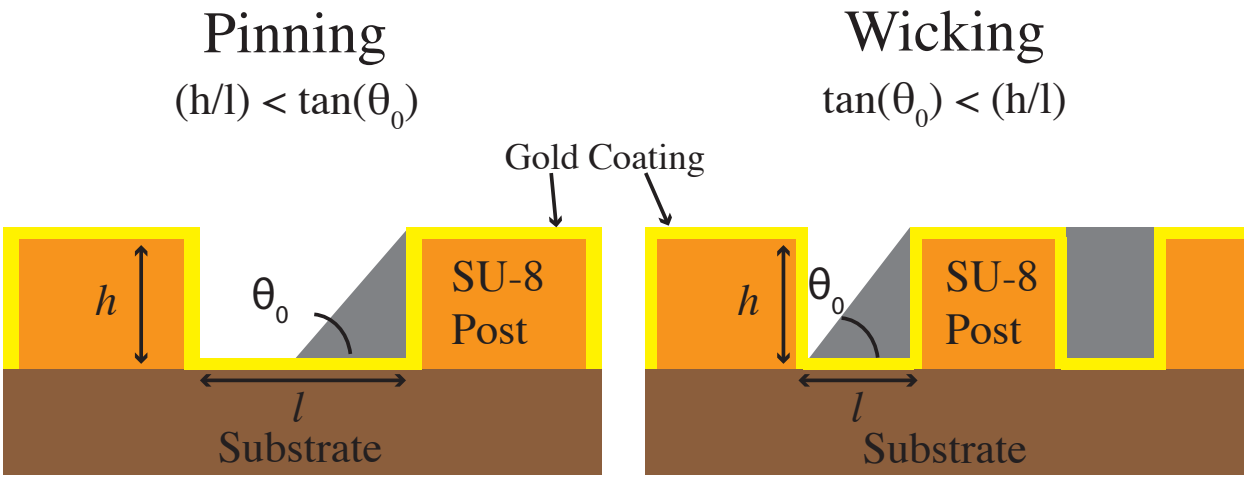


Figure 5.7 Schematic depiction of the geometric requirements to promote imbibition of a liquid metal into a microstructured film.

surface to further stabilize the imbibition of a liquid.[26] In these systems, whether a liquid completely wets into a microstructured surface depends on the wetting behavior of the liquid on the unstructured solid, θ_0, the interpillar distance, *l*, between adjacent microstructured pillars and the height, *h*, of the microstructured pillars. As shown in Figure 5.7, the aspect ratio of the pillars dictates whether the liquid will be completely wetted (wicking) into the film or dewetted (pinned) and eventually forced into large droplets. Here, microstructured SU-8 patterned pillars 13 μm high and with an interpillar distance of 20 μm were microfabricated on a Si substrate surface and coated with approximately 20 nm of Au by thermal evaporation, as shown in Figure 5.8. Shown in Figure 5.8a) is a cross-section scanning electron micrograph of the pillars. An angled top-down micrograph of the pillars is shown in Figure 5.8b) with an inset energy dispersive spectroscopy map demonstrating the coverage of evaporated Au, which was performed following photolithography. In retrospect, one specific improvement to this platform would be finding a method to enable conformal Au coating on the sidewalls in order to further stabilize the liquid metal which will be shown in the subsequent section. A wide view scanning electron micrograph of the pillar array is shown in Figure 5.8c).

Following the microfabrication of the structure electrode, liquid Ga was thermally evaporated and completely imbibed into the surface, as shown in Figure 5.9. Using these conditions, the liquid Ga thin film was completely wetted into the surface and formed a 12 μm thick contiguous film that covered the entirety of the structured surface, as shown in cross section electron micrograph in Figure 5.9a) and the corresponding elemental map shown in Figure 5.9c). The low magnification scanning top-down view shown in Figure 5.9b) demonstrates that the film is smooth and contiguous across the entire surface of the microstructured electrode. To evaluate the stability of the liquid metal thin film under potentiostatic conditions, a cyclic voltammetry was

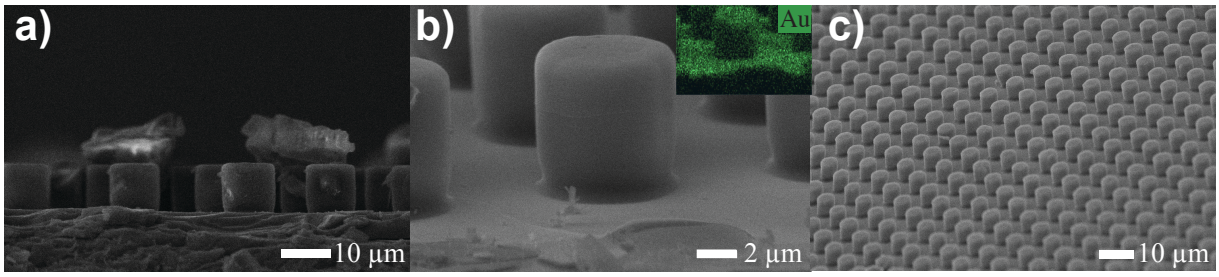


Figure 5.8 a) Cross-section micrograph of a Si substrate patterned with 13 µm an array of pillars. b) High magnification scanning electron micrograph of a pillar after coating with Au by thermal evaporation. Inset: elemental dispersive spectroscopy map of Au in the same region. c) Low magnification scanning electron micrograph of the micropillar array.

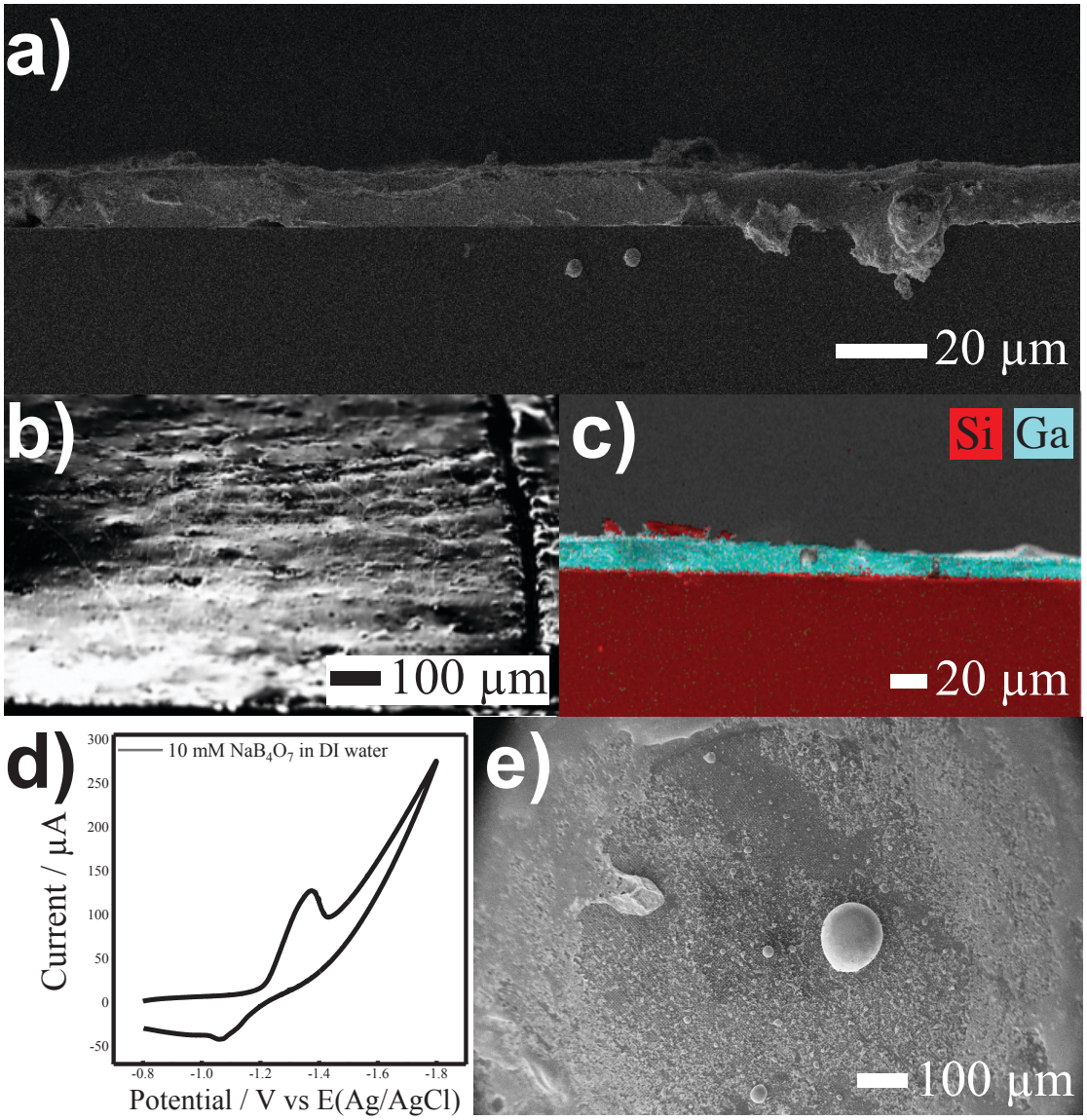


Figure 5.9 a) Cross-section scanning electron micrograph of Au coated pillar array following thermal evaporation of Ga and complete imbibition. b) Top down scanning electron micrograph of the film shown in a). c) Cross section elemental dispersive spectroscopy of the film shown in a) demonstrating the Ga (blue) film and the Si (red) substrate. d) Shown is a cyclic voltammogram of the film in a) immersed in 10 mM NaB_4O_7 in deionized water. Scan rate = 100 mv s^{-1}. e) Top-down low magnification scanning electron micrograph of the microstructured electrode after voltammetric cycling.

collected with the electrode immersed in a 10 mM NaB_4O_7 electrolyte in deionized water, as shown in Figure 5.9d). The cycle shows a clear reduction peak around -1.3 V vs *E*(Ag/AgCl) which corresponds to the reduction of surface oxides on the liquid metal. During cycling, the liquid metal thin film electrode surface actuated and began to de-wet from the microstructured surface at the same time the reduction event occurred. A top-down electron micrograph of the electrode surface following voltammetric cycling is shown in Figure 5.9e). This observation suggests that the gallium surface oxides help to stabilize the liquid metal thin film in the structured post and that the increased surface tension of the pure gallium surface following the removal of these surface oxides overcame the lyophobic forces of the Au coated microstructured surface intended to keep the liquid metal thin film imbibed in the electrode. That is, using the (h/l) aspect ratio of 0.65 did not furnish a stable liquid metal thin film under potentiostatic conditions. Further efforts in this vein should explore microstructured pillar electrodes with (h/l) aspect ratios smaller than 0.42.[26] If fruitful, this method would greatly simplify epitaxial electrodepositions by ec-LPE and potentially open avenues for the exploration of non-planar heterogeneously nucleated crystalline thin films.

5.3 Si ec-LPE for Crystalline Si Anodes in Li-Ion Batteries

Crystalline Silicon is an attractive anode material for Li ion battery anodes since it has the highest known theoretical charge capacity (4,200 mAh g^{-1}) and a low discharge potential.[20] However, the stress induced on the Si lattice during Li^+ intercalation causes a 400% volume expansion, which causes extreme structural damage after just a few cycles. Several strategies have been employed to limit the lattice pulverization during lithiation such as the use of nanostructures, carbon composites, intentional dopants, and intentional defect generation.[20-23] In the case of the

latter two, higher dopant densities and high quantities of 2D defects (twins, stacking faults, dislocations) have been shown to impart significant robustness to Si during lithiation, preventing fracture at highest discharge capacities for many more cycles.[23-24] Accordingly, as discussed in Chapter 4, crystalline Si thin films grown by ec-LPE at room temperature show great promise as anode materials owing to the extremely high doping of Ga (~23 at. %) and the highly defective structure of the films. Here, preliminary efforts exploring the synthesis of crystalline Si by ec-LPE on a Cu current collector are described.

To explore whether crystalline Si could be heterogeneously nucleated on Cu substrates, preliminary experiments were performed with *e*-GaIn coated Cu foil substrates. Si ec-LPE pulsed electrodeposition experiments (E_1 = -1.6 V for 0.2 ms, E_2 = -0.77 V for 10 ms) from electrolyte containing 0.5 M $SiCl_4$ and 0.1 M $(C_4H_9)_4NCl$ in propylene carbonate at T = 23 °C were performed for 2 hr. A macroscopic photograph of the electrode after *e*-GaIn was removed is shown in Figure 5.10a). Here, where *e*-GaIn was exposed to the Cu foil, an intermetallic layer was formed. Shown in Figure 5.10b) a low magnification scanning electron micrograph of the red region shown in Figure 5.10a) show the general coarseness of the electrode surface, as a consequence of the formed intermetallic structure. Previous researchers have observed the same morphology for *e*-GaIn on Cu electrodes owing to the formation of $CuGa_2$ intermetallic layer.[25] A high magnification scanning electron micrograph of the green box shown in Figure 5.10b) demonstrating the presence of Si crystallites is shown in Figure 5.10c), with corresponding energy dispersive spectroscopy elemental map scans of Si and Ga shown in Figure 5.10d,e), respectively. The deposits shown in Figure 5.10c) correspond only to Si and Ga, suggesting the formation crystalline structure, given the propensity of amorphous Si to oxidize upon exposure to ambient lab air. The presented data demonstrate that while Si crystallites can be formed on non-crystalline substrates, the surface

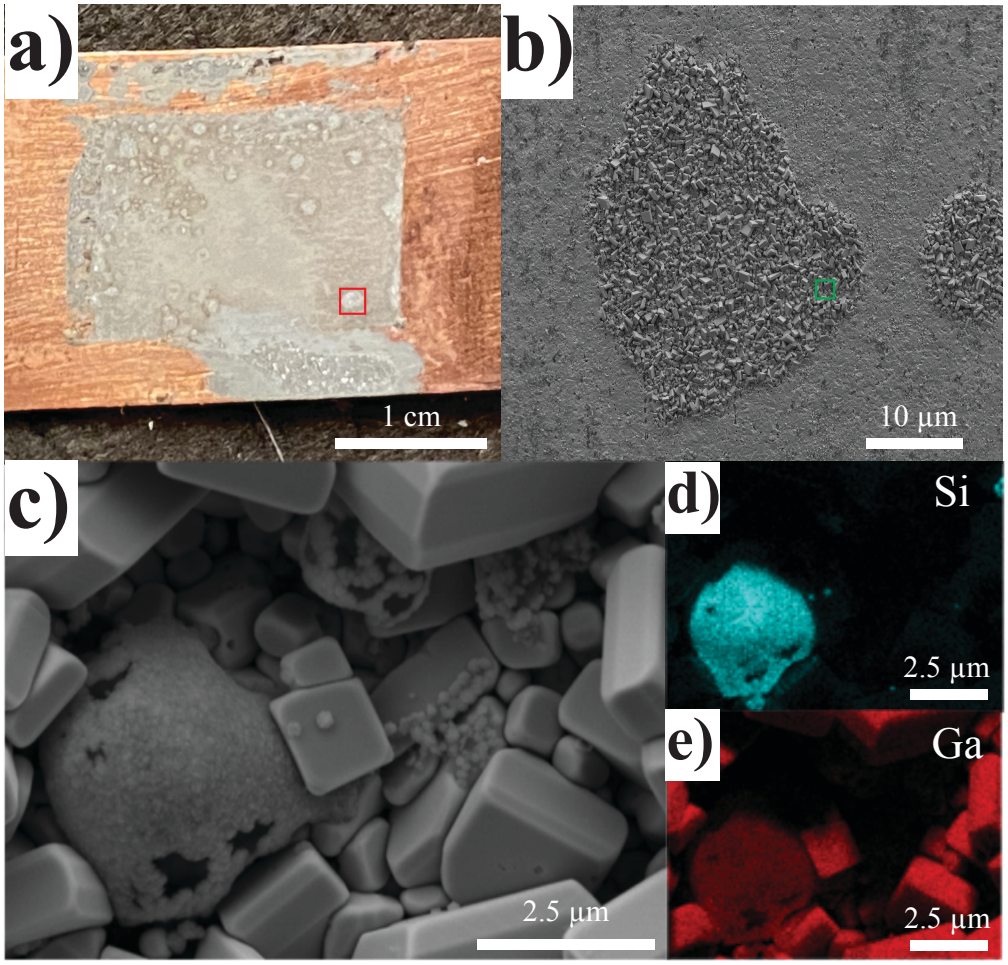


Figure 5.10 a) Macroscopic image of a compressionless Si ec-LPE pulsed electrodeposition experiment (E_1 = -1.6 V for 0.2 ms, E_2 = -0.77 V for 10 ms) from electrolyte containing 0.5 M $SiCl_4$ and 0.1 M $(C_4H_9)_4NCl$ in propylene carbonate at T = 23 °C using a *e*-GaIn thin film on Cu foil support. b) Scanning electron micrograph of the active electrode area after removal of *e*-GaIn, corresponding to the red region highlighted in a). Scanning electron micrograph of the green region in b) with corresponding energy dispersive spectroscopy elemental map scans of d) Si and e) Ga.

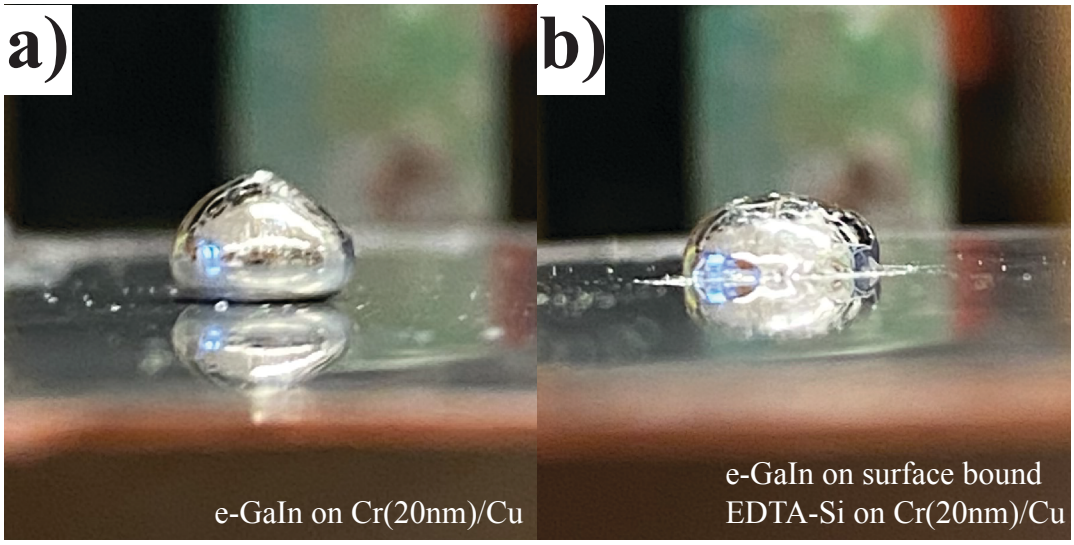


Figure 5.11 Macroscopic photographs showing the wetting behavior of *e*-GaIn on Cr coated (20 nm) Cu foil substrates a) without and b) with surface bound N-(trimethoxysilylpropyl)ethylenediamine, triacetic acid.

coarseness resulting from the intermetallic layer from contact of the *e*-GaIn with Cu directly precludes the formation of a Si thin film.

In order to prepare Cu foil electrodes for application in the ec-LPE a barrier layer between the Cu and *e*-GaIn electrode was hypothesized to be necessary. In the selection of a barrier layer, the material needs to adhere strongly to Cu, while also being insoluble to Cr in order to prevent the same problematic intermetallic layer formation. To this end 20 nm Cr thin films were deposited by thermal evaporation on the Cu foil substrates prior to lithographic patterning. However, the wetting of liquid metals on foreign substrates depends on the interfacial energy between the liquid and the solid. Since no intermetallic layer forms between Cr and Ga, here a surface modification was employed to promote the wetting instead. Specifically, N-(trimethoxysilylpropyl) ethylenediamine, triacetic acid was reacted with the surface oxides of Cr to promote the adhesion of the liquid metal electrode to the surface. The wetting characteristics of *e*-GaIn on the Cr surface with and without this surface modification is shown in Figure 5.11.

Using the modified Cr coated Cu substrate, Si ec-LPE pulsed electrodeposition experiments (E_1 = -1.6 V for 0.2 ms, E_2 = -0.77 V for 10 ms) for 4hr from an electrolyte containing 0.5 M $SiCl_4$ and 0.1 M $(C_4H_9)_4NCl$ in propylene carbonate at T = 23 °C were performed. The results are shown in Figure 5.12). Shown in Figure 5.12a) is a scanning electron micrograph of the resultant deposit on the electrode surface after mechanical removal of the liquid *e*-GaIn electrode. Large mostly contiguous regions of the deposited are observed over the whole of the active electrode area (the white dotted region in the macroscopic photograph inset image). A high magnification scanning electron micrograph of the deposit is shown in Figure 5.12b). The observed deposit was a coalescing film that was faceted. The Raman spectra shown in the inset was taken of the deposit and showed a broad band centered around 480 cm^{-1} and a sharp peak at 520 cm^{-1},

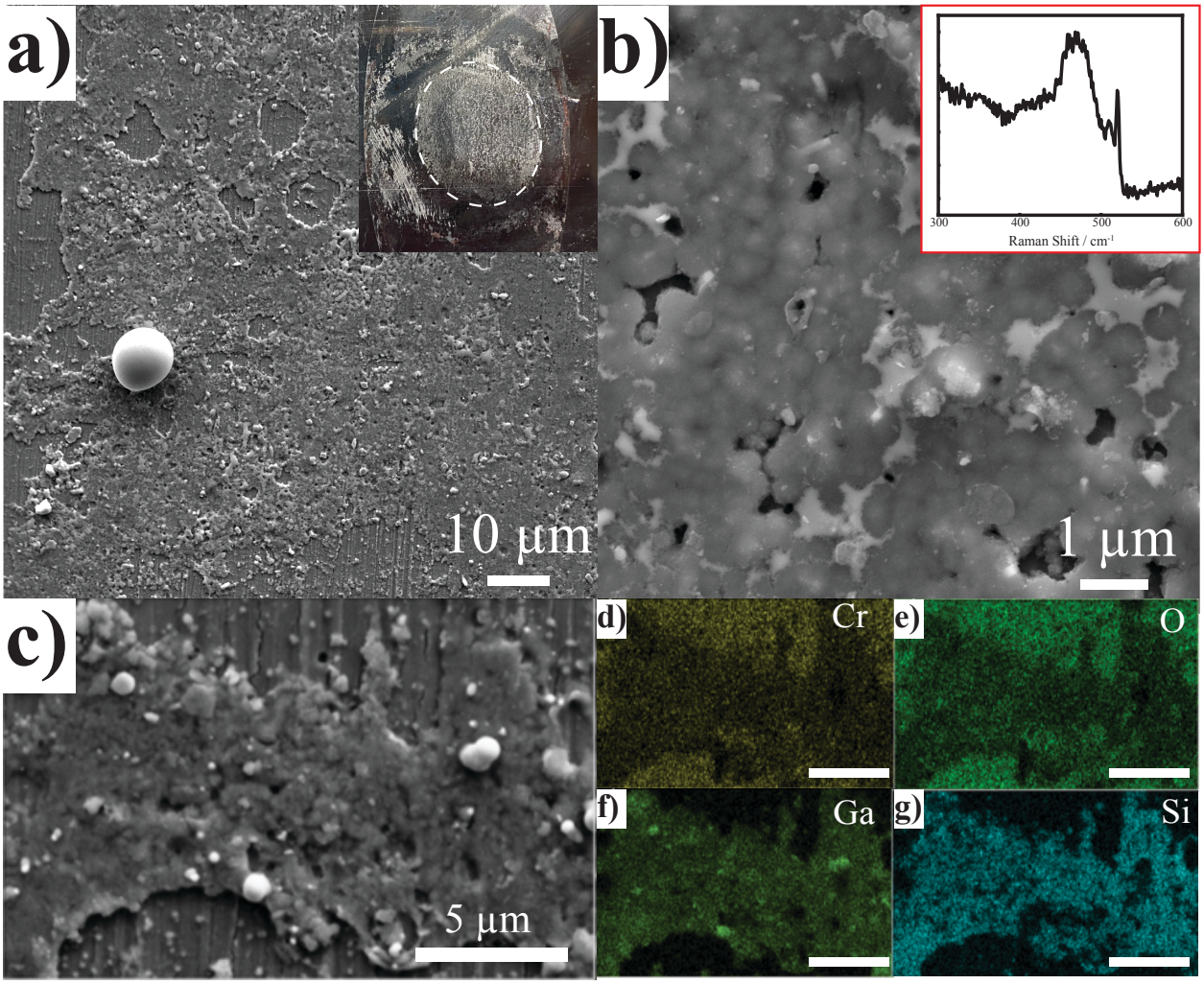


Figure 5.12 a) Low magnification scanning electron micrograph of a Si ec-LPE pulsed electrodeposition experiment (E_1 = -1.6 V for 0.2 ms, E_2 = -0.77 V for 10 ms) from electrolyte containing 0.5 M $SiCl_4$ and 0.1 M $(C_4H_9)_4NCl$ in propylene carbonate at T = 23 °C using a *e*-GaIn thin film on Cr (20 nm) coated Cu foil support showing high degree of deposit coverage. Inset: Macroscopic image of the Cr/Cu electrode surface. b) High magnification scanning electron micrograph of the active electrode area of the film shown in a). Inset: Raman spectra corresponding to the film. c) Scanning electron micrograph of the deposit film with corresponding energy dispersive spectroscopy elemental map scans of d) Cr, e) O, f) Ga, and e) Si.

which is consistent with a heavily metal doped crystalline Si. Elemental maps of the region shown in Fig 5.12c) were recorded demonstrating that the film was exclusively composed of Si and Ga, and that the growth of crystalline Si thin films on a Cu substrate is possible at ambient temperatures. Attempts to further remove residual liquid metal by acid etching in 1M HCl destroyed the chromium layer underneath, which in turn removed the crystalline Si deposit. Future efforts in this work should instead use selective electrochemical etching to remove the liquid metal electrode instead.

5.4 Conclusions

This thesis sought to challenge the paradigm of modern crystalline Si manufacture by re-examining the potential utility of electrodeposition as a synthetic strategy. This thesis has two major accomplishments on this front. First, novel Si electrodeposition precursors containing structural moieties unreported in the literature have been examined. Second, the application of novel pulsed electrodeposition waveform to ec-LPE was demonstrated, enabling the growth of thick epitaxial Si thin films under ambient conditions.

While the oligochlorosilane and tetraisocyanatosilane precursors were demonstrated to be potentially useful for Si electrodeposition, both species were shown to have intrinsic limitations. In the case of the oligochlorosilanes, while the electrochemical and electrodeposition characteristics were similar to the $SiCl_4$ under ambient conditions, the presence of the Si-Si bond moiety at elevated temperature was shown to be sensitive due to its propensity to undergo nucleophilic attack. Thus, in the exploration of future Si electrodeposition precursors, species containing Si-Si bonds in the backbone should be avoided. In the case of tetraisocyanatosilane,

while the voltammetric response and amperometric products were similar to the chlorosilanes under ambient conditions, at elevated temperatures the electrochemical response was significantly attenuated, suggesting the emergence of processes beyond Si^0 formation. This high temperature activity was ascribed to electrochemical activity of the free NCO^- ligand byproducts formed, which are known to electropolymerize. Both the perchlorinated oligochlorosilane and tetraisocyanatosilane precursors did not produce crystalline Si when electrodeposited at a Ga electrode, indicating that there are mechanistic complexities to the ec-LLS process that require further investigation in order to design optimal electrolyte baths.

Previously, the limitation of the applicability of $SiCl_4$ to the ec-LPE method was thought to arise from the inevitable formation of parasitic species that result in the unavoidable cessation of the electrodeposition process. Here, the same observation was made when a direct electrodeposition waveform was applied, resulting in thin epitaxial Si thin films. However, through the application of a pulsed electrodeposition waveform to (1) generate Si^0 by electrodeposition and (2) allow the Si^0 to dissolve into the liquid metal electrode without aggregating on the surface, thick epitaxial films were grown. The novelty of this method was further demonstrated to enable the growth of epitaxial Si thin films at ambient temperatures, therein setting a new thermal benchmark in the growth of group IV epitaxial films.

This thesis demonstrates that ec-LPE is a potentially disruptive method for the growth of crystalline Si thin films. The application of an applied pulsed waveform opens new avenues for more finely tuning the materials quality of as-deposited films. Evidence in this thesis demonstrates that it is possible to tune both the impurity content and defectiveness of as-grown films if deliberate care is taken in the selection of experimental parameters employed. This work motivates further exploration for the limits of ec-LPE as a tactic for crystalline thin film preparation.

Future work should aim to examine both conditions that confer the highest degree of structural perfection to as-grown layers and novel application of the unique Si thin films obtainable by ec-LPE. In the growth of higher quality epitaxial layers by ec-LPE, the flux of zero valent species into the melt should be slowed as much as possible. The best ways to accomplish this include: (1) altering the liquid metal composition to have a larger equilibrium concentration of the zero valent species, (2) identify the necessary pulse widths to ensure the liquid metal electrode is no longer saturated with zero valent precursor, (3) use smaller concentrations of oxidized precursor in the electrolyte bath, (4) explore the use of thicker liquid metal thin films in order that each deposition pulse results in a smaller change in effective concentration of zero valent species. Future researchers looking to further this work should aim to develop strong skillsets in advanced electron microscopy (SEM/FIB, TEM, STEM), electron diffraction (selected area electron diffraction and electron backscatter diffraction), and x-ray diffraction techniques to maintain a high throughput in the characterization of obtained materials.

5.5 References

1. Cheek, Q.; Fahrenkrug, E.; Hlynchuk, S.; Alsem, D. H.; Salmon, N. J.; Maldonado, S., In Situ Transmission Electron Microscopy Measurements of Ge Nanowire Synthesis with Liquid Metal Nanodroplets in Water. *ACS Nano* **2020,** *14* (3), 2869-2879.
2. Olesinski, R. W.; Kanani, N.; Abbaschian, G., The Ga− Si (Gallium-Silicon) system. *Bulletin of alloy phase diagrams* **1985,** *6* (4), 362-364.
3. Olesinski, R. W.; Kanani, N.; Abbaschian, G., The In− Si (Indium-Silicon) system. *Bulletin of alloy phase diagrams* **1985,** *6* (2), 128-130.
4. Reynolds, A. N. C. a. W. F., The System Inidum-Gallium-Silver. *Can. J. Chen.* **1962,** *40*, 37-45.
5. Olesinski, R.; Gokhale, A.; Abbaschian, G., The Ag-Si (silver-silicon) system. *Bulletin of Alloy Phase Diagrams* **1989,** *10* (6), 635-640.
6. Castanet, R.; Chastel, R., Thermodynamic Behaviour of Pd-Si, Pd-Ge and Pt-Ge Molten Alloys. *International Journal of Materials Research* **1987,** *78* (2), 97-102.
7. Du, Z.; Guo, C.; Yang, X.; Liu, T., A thermodynamic description of the Pd–Si–C system. *Intermetallics* **2006,** *14* (5), 560-569.

8. Mostafa, A.; Medraj, M., Binary Phase Diagrams and Thermodynamic Properties of Silicon and Essential Doping Elements (Al, As, B, Bi, Ga, In, N, P, Sb and Tl). *Materials* **2017,** *10* (6).
9. Nash, P.; Nash, A., The Ni− Si (Nickel-Silicon) system. *Bulletin of Alloy Phase Diagrams* **1987,** *8* (1), 6-14.
10. Xu, L. L.; Wang, J.; Liu, H. S.; Jin, Z. P., Thermodynamic assessment of the Pt–Si binary system. *Calphad* **2008,** *32* (1), 101-105.
11. Yan, X.; Chang, Y., A thermodynamic analysis of the Cu–Si system. *Journal of Alloys and Compounds* **2000,** *308* (1-2), 221-229.
12. Chevalier, P.-Y., Thermodynamic evalution of the Ag-Si system. *Thermochimica acta* **1988,** *130*, 33-41.
13. Olesinski, R. W.; Abbaschian, G. J., The Cu−Si (Copper-Silicon) system. *Bulletin of Alloy Phase Diagrams* **1986,** *7* (2), 170-178.
14. Anres, P.; Gaune-Escard, M.; Bros, J., Thermodynamics of the (Pt+ Ga) system. *Journal of alloys and compounds* **1996,** *234* (2), 264-274.
15. Taccardi, N.; Grabau, M.; Debuschewitz, J.; Distaso, M.; Brandl, M.; Hock, R.; Maier, F.; Papp, C.; Erhard, J.; Neiss, C., Gallium-rich Pd–Ga phases as supported liquid metal catalysts. *Nature chemistry* **2017,** *9* (9), 862-867.
16. Liu, J.; Guo, C.; Li, C.; Du, Z., Thermodynamic assessment of the Au–Ga system. *Journal of alloys and compounds* **2010,** *508* (1), 62-70.
17. Yuan, W.; Qiao, Z.; Ipser, H.; Eriksson, G., Thermodynamic assessment of the Ni-Ga system. *Journal of Phase Equilibria and Diffusion* **2004,** *25* (1), 68-74.
18. Nguyen, T.; Foley, R., The chemical nature of aluminum corrosion: III. the dissolution mechanism of aluminum oxide and aluminum powder in various electrolytes. *Journal of the Electrochemical Society* **1980,** *127* (12), 2563.
19. Lee, M.; Lee, K.; Ko, D.-H., Structural, bonding, and elastic properties of Si:X (X = B, Al, and Ga): a theoretical study. *Semiconductor Science and Technology* **2020,** *35* (6), 065004.
20. Chan, C. K.; Peng, H.; Liu, G.; McIlwrath, K.; Zhang, X. F.; Huggins, R. A.; Cui, Y., High-performance lithium battery anodes using silicon nanowires. *Nature nanotechnology* **2008,** *3* (1), 31-35.
21. Graetz, J.; Ahn, C.; Yazami, R.; Fultz, B., Highly reversible lithium storage in nanostructured silicon. *Electrochemical and Solid State Letters* **2003,** *6* (9), A194.
22. Laik, B.; Eude, L.; Pereira-Ramos, J.-P.; Cojocaru, C. S.; Pribat, D.; Rouvière, E., Silicon nanowires as negative electrode for lithium-ion microbatteries. *Electrochimica Acta* **2008,** *53* (17), 5528-5532.
23. Shimizu, M.; Kimoto, K.; Kawai, T.; Taishi, T.; Arai, S., Dopant Effect on Lithiation/Delithiation of Highly Crystalline Silicon Synthesized Using the Czochralski Process. *ACS Applied Energy Materials* **2021,** *4* (8), 7922-7929.
24. Wang, J.; Meng, X.; Fan, X.; Zhang, W.; Zhang, H.; Wang, C., Scalable Synthesis of Defect Abundant Si Nanorods for High-Performance Li-Ion Battery Anodes. *ACS Nano* **2015,** *9* (6), 6576-6586.
25. Cui, Y.; Liang, F.; Yang, Z.; Xu, S.; Zhao, X.; Ding, Y.; Lin, Z.; Liu, J., Metallic bond-enabled wetting behavior at the liquid Ga/CuGa2 interfaces. *ACS applied materials & interfaces* **2018,** *10* (11), 9203-9210.
26. Hirsch, A., Lacour, S. P. A Method to Form Smooth Films of Liquid Metal Supported by Elastomeric Substrate *Adv. Sci.* **2018**, *5*, 1800256